

Département de Physique  
Université de Fribourg (Suisse)



DuMond curved crystal spectrometer  
and  
Photoinduced  $K\alpha$  hypersatellite  
x-ray lines of molybdenum

THÈSE

Présentée à la Faculté des Sciences de l'Université de Fribourg (Suisse)  
pour l'obtention du grade de  
*Doctor rerum naturalium*

Monika Szlachetko  
Pologne

Numéro de la thèse:  
1637

Fribourg 2009

Acceptée par la Faculté des Sciences de l'Université de Fribourg (Suisse)

sur la proposition de:

Prof. Dr. Dionys Baeriswyl, Université de Fribourg, Président de jury

Prof. Dr. Jean-Claude Dousse, Université de Fribourg, Directeur de Thèse

Prof. Dr. Marek Pajek, Jan Kochanowski University, Kielce, Poland, Rapporteur

Dr. Joanna Hoszowska, Université de Fribourg, Rapporteur

Fribourg, 29 mai 2009

Le Directeur de thèse :

Le doyen :

Prof. Dr. Jean-Claude Dousse

Prof. Dr. Titus Jenny

# Contents

Abstract.....3  
Résumé.....7

## Part I: The DuMond curved crystal spectrometer

1. Introduction.....13  
2. Bragg law and structure factor.....18  
3. The DuMond crystal spectrometer of Fribourg.....22  
    3.1 Spectrometer design.....22  
        3.1.1 Overview of the instrument.....22  
        3.1.2 Target chamber.....26  
        3.1.3 Crystal and crystal rotation mechanism.....28  
        3.1.4 Optical laser interferometer.....32  
        3.1.5 Collimator and collimator rotation mechanism.....36  
        3.1.6 Detectors.....39  
        3.1.7 Driving and acquisition electronics.....41  
    3.2 LabVIEW software.....43  
        3.2.1 General description.....43  
        3.2.2 Serial port communication.....45  
        3.2.3 Communication with the DAQ card.....48  
    3.3 Data acquisition.....51  
    3.4 Data analysis.....54  
4. Examples of measurements.....57  
    4.1 Spectrometer resolution.....57  
        4.1.1 Standard method to determine the instrumental broadening  
                of the spectrometer.....57  
        4.1.2 Dependence of the spectrometer resolution on the slit width,

focal distance and diffraction order.....	59
4.1.3 Novel self-consistent method to determine the spectrometer resolution.....	62
4.2 Spectrometer sensitivity.....	69
4.3 Spectrometer precision.....	72
4.4 Additional examples of applications.....	76
4.4.1 Measurements of the Au <i>L</i> x-ray lines series.....	76
4.4.2 Determination of the mass attenuation coefficient of molybdenum around the <i>K</i> -absorption edge.....	85
5. Conclusion.....	91
6. Bibliography.....	93

## Part II Photoinduced $K\alpha$ hypersatellite x-ray lines of molybdenum

1. Introduction.....	101
2. Experimental method and measurements.....	105
3. Data analysis.....	112
4. Results and discussion.....	115
4.1 Energies.....	115
4.2 Natural line widths.....	118
4.3 $K\alpha_1^h$ to $K\alpha_2^h$ intensity ratio.....	120
4.4 Hypersatellite line-to-diagram line intensity ratio $I(K\alpha^h)/I(K\alpha)$ .....	122
5. Conclusion.....	126
6. Bibliography.....	127
Acknowledgments.....	133
Curriculum vitae.....	135
List of publications.....	137

## Abstract

The present Ph.D. thesis includes two research projects in the field of Atomic Physics. The first project concerns the high-resolution transmission curved crystal spectrometer of the DuMond type installed at the University of Fribourg. The construction details and more specifically the developed software for the spectrometer control and data acquisition as well as the operation characteristics and performances of the spectrometer are presented. The second part is devoted to the study of the  $K\alpha$  hypersatellite lines of molybdenum induced by photon impact. From these measurements the energies, linewidths and the intensity ratio of the  $K\alpha_1^h$  to  $K\alpha_2^h$  hypersatellite lines, as well as the  $K$ -shell double photoionization probability were deduced and compared to theoretical and other experimental values.

Curved crystal x-ray spectrometers have proved to be important tools in atomic structure studies and x-ray transition metrology. The high energy resolution and precision of crystal x-ray spectrometers permit to resolve the complex x-ray spectra. The first project of the present thesis concerns the transmission-type bent-crystal spectrometer that was constructed several years ago at the Physics Department of the University of Fribourg. In the present work, to modernize the spectrometer control and acquisition system, the obsolete PEP Modular Computer System was replaced by a PC and a new LabVIEW-based user-friendly software for the control and data acquisition was developed. First, the spectrometer design and construction details including the target chamber, the crystal bending device and rotation mechanism, the optical laser interferometer, collimator, detectors and the driving and acquisition electronics as well as the developed LabVIEW-based software are presented. In order to check the operational characteristics of the spectrometer equipped with the new control software, the energy resolution, sensitivity and precision of the instrument were determined.

The instrumental response of the spectrometer was obtained from the measurements of the gadolinium  $K\alpha_1$  ( $2p_{3/2} \rightarrow 1s_{1/2}$ ) x-ray emission line. For this purpose a metallic Gd sample was irradiated with the bremsstrahlung produced by a Au-anode x-ray tube operated at 80 kV and 30 mA. It was found that the instrumental response of the spectrometer which depends mainly on the slit width, the crystal mosaicity and the precision of the crystal curvature is well reproduced by a Gaussian function with the

standard deviation  $\sigma = 4.75 \pm 0.02$  arcsec of angular resolution. It was demonstrated that the slit-to-crystal distance should be optimized for each measured x-ray line in order to obtain the best resolution. It was also shown that the instrumental energy resolution of the spectrometer can be improved by measuring the x-ray spectra in higher orders of reflection. Moreover, a numerical method to determine the spectrometer resolution and natural linewidth of an x-ray transition was developed. It is based on measurements of an x-ray emission line in five different orders of reflection and solving a set of equations by means of the nonlinear least-squares method. A Gd  $K\alpha_1$  natural linewidth of  $26.18 \pm 0.09$  eV was obtained, the accuracy of which is much better compared to the recommended value of  $26.12 \pm 1.77$  eV. In order to test the sensitivity of the spectrometer (high luminosity with low background conditions) the very weak Gd  $K\alpha_3$  ( $2s_{1/2} \rightarrow 1s_{1/2}$ ) x-ray emission line was observed. The obtained  $K\alpha_3$  energy and the  $I(K\alpha_3)/I(K\alpha_1)$  intensity ratio of  $(1.61 \pm 0.11) \times 10^{-4}$  were found to be in good agreement with experimental results for neighboring elements and theoretical predictions. The K-L<sub>2</sub>, K-M<sub>3</sub> and L<sub>2</sub>-M<sub>3</sub> transitions of Au were then measured to probe the precision of the spectrometer by means of the Ritz combination principle.

Further, the performance of the x-ray spectrometer was probed by measuring the L-series lines of gold. These measurements were carried out in the direct geometry, i.e., the Au anode of the x-ray tube served as the target. The energies and the linewidths of 13 Au L x-ray emission lines were extracted and compared to the other existing theoretical and experimental values. In addition the  $L\beta_2'$  and  $L\beta_2''$  satellites of the  $L\beta_2$  (L<sub>3</sub>-N<sub>5</sub>) x-ray line were observed and the obtained energies were found to be in good agreement with other experimental data. It should be mentioned that in this direct geometry it was possible to observe x-rays with energies down to 9.7 keV corresponding to the Au  $L\alpha_{1,2}$  (L<sub>3</sub>-M<sub>4,5</sub>) x-ray transitions. In fact, the x-ray spectrometer angular range of  $\pm 20$  deg. corresponds theoretically to the minimum photon energy of 7.5 keV for the quartz crystal (110) reflecting planes in the first order of reflection. However, as for photon energies below about 10 keV the absorption of x-ray radiation in the crystal plate increases drastically, the transmission-type spectrometers are usually not employed for these energies, the lowest energy for most of them being even about 20 keV. Finally, the spectrometer was used to determine the absorption mass coefficient around the K-absorption edge for molybdenum

( $Z = 42$ ). The obtained results were compared with existing data measured with monochromatic synchrotron radiation. A very good agreement between both datasets was found. Further, the binding energy of the Mo  $1s$  atomic level was determined. A value of 20.00018(36) keV, in very good agreement with the tabulated ones, was obtained.

The second part of the thesis is devoted to the photoinduced  $K\alpha$  hypersatellite x-ray lines of molybdenum. The  $K\alpha^h$  hypersatellites ( $1s^{-2} \rightarrow 1s^{-1}2p^{-1}$ ) spectra result from the radiative decay of the  $K$ -shell double vacancy states. The experiment was performed by means of high resolution x-ray emission spectroscopy using the Fribourg transmission type DuMond curved crystal x-ray spectrometer and the gold anode x-ray tube operated at 90 kV as the x-ray source. In general, the very low double photoionization cross sections for high- $Z$  elements, as well as the presence of the  $K\alpha$  diagram line tails in the  $K$  x-ray hypersatellite energy region and the x-ray tube bremsstrahlung related background and also the low photon flux, make the measurements of the  $K$  x-ray hypersatellite spectra quite challenging and time consuming. In fact, the hypersatellite high-resolution x-ray emission spectrum of Mo induced by photon impact using a conventional x-ray source was measured for the first time.

Two sets of measurements were performed, namely with and without additional absorbers between the x-ray tube and the Mo sample. The absorbers served to reduce the background level in the region of the hypersatellite lines by cutting down the part of the bremsstrahlung below the  $K$ -shell double ionization threshold ( $\sim 40$  keV). The choice of the proper absorbers and optimal thicknesses of the lattes were based on calculations of the x-ray tube intensity response. From the measured x-ray hypersatellites spectra the energies, linewidths and the intensity ratio of the  $K\alpha_1^h$  to  $K\alpha_2^h$  were obtained. The energies and natural linewidths were found to be consistent, within the experimental uncertainties, with the MCDF (Multi-Configuration Dirac-Fock) calculations and the few existing data from electron and ion-collision studies. The  $K\alpha_1^h$  to  $K\alpha_2^h$  intensity ratio probes the intermediacy of the coupling. The extracted value of  $1.4 \pm 0.5$  was found to be close to theoretical and other available experimental data. Moreover, the ratio of the double to single photoionization cross section was derived from the hypersatellite to diagram line intensity ratio. Since a polychromatic x-ray source was used, the differences

in the average photon energies and the number of photons for the single- and double-ionization cross sections were accounted for. A value of  $1.72 \times 10^{-4}$  was obtained for the ratio which was found to be two times smaller than the single other experimental data existing for Mo.



Ce mémoire de thèse comprend deux projets de recherche dans le domaine de la physique atomique. Le premier projet concerne le spectromètre à cristal courbé DuMond installé dans le bâtiment de physique de l'Université de Fribourg. Les détails de construction de cet instrument et plus spécifiquement le nouveau logiciel développé pour la conduite du spectromètre et l'acquisition des données sont présentés. Les propriétés du spectromètre et ses performances sont également décrites à l'aide de quelques exemples d'application. Le second projet est consacré à l'étude des raies X hypersatellites  $K\alpha_{1,2}^h$  du molybdène induites par photoionisation. A partir des mesures effectuées, les énergies et les largeurs naturelles de ces transitions ont été déterminées et comparées aux données expérimentales et théoriques existantes. Le rapport d'intensité  $I(K\alpha_1^h)/I(K\alpha_2^h)$  ainsi que le rapport des sections efficaces de double et simple photoionisation  $\sigma_{KK}^{photo} / \sigma_K^{photo}$  ont également pu être déduits des mesures.

Les spectromètres à cristal courbé ont prouvé leur importance dans les études de structure atomique et de métrologie de rayons X. Le pouvoir de résolution élevé de ces instruments ainsi que leur précision permettent en effet de résoudre des spectres de rayons X complexes. Le premier volet de cette thèse de doctorat concerne un spectromètre à cristal courbé de type Laue construit au Département de Physique de l'Université de Fribourg il y a quelques années. Dans ce travail, l'ancien système de commande du spectromètre et d'acquisition de données, le PEP Modular Computer System, a été remplacé par un PC et un nouveau logiciel, basé sur le système LabView, a été développé. Cette première partie de la thèse décrit tout d'abord le spectromètre dans son ensemble puis passe en revue les différents composants de l'instrument: la chambre à cible, le système utilisé pour courber le cristal et le mécanisme de rotation de ce dernier, l'interféromètre à laser, le collimateur, le système de détection, l'électronique de commande du spectromètre et celle pour l'acquisition des données ainsi que le nouveau logiciel basé sur LabView. Afin de vérifier les caractéristiques opérationnelles de l'appareil et jauger ses performances avec le nouveau logiciel de commande et d'acquisition, la résolution en énergie du spectromètre, sa sensibilité et sa précision ont été déterminées.

La réponse instrumentale du spectromètre a été déterminée en mesurant la raie  $K\alpha_1$

du gadolinium. Pour cela, une cible métallique de Gd a été irradiée au moyen du Bremsstrahlung d'un tube de rayons X. Il a été montré que la réponse instrumentale qui dépend principalement de la largeur de la fente placée devant la cible, de la mosaïcité du cristal et de la précision de sa courbure, est bien reproduite par une Gaussienne ayant un écart-type angulaire  $\sigma = 4.75 \pm 0.02$  arcsec. Les variations de la résolution instrumentale en fonction de la distance focale du cristal et de l'ordre de diffraction sont également démontrées. De plus, une nouvelle méthode auto-consistante pour déterminer la résolution du spectromètre a été développée. Elle est basée sur la mesure d'une raie X en cinq ordres de diffraction et la résolution du système surdéterminé d'équations résultant de ces mesures par une méthode des moindres carrés non-linéaire. En plus de la réponse instrumentale, cette méthode fournit la largeur naturelle de la raie X mesurée. Une valeur de  $26.18 \pm 0.09$  eV a par exemple été obtenue pour la raie  $K\alpha_1$  du Gd choisie pour tester la méthode, une valeur vingt fois plus précise que la valeur recommandée de  $26.12 \pm 1.77$  eV. Afin de vérifier la sensibilité du spectromètre, la transition interdite  $K\alpha_3$  ( $2s_{1/2} \rightarrow 1s_{1/2}$ ) du Gd dont l'intensité est extrêmement faible a été mesurée. L'énergie de la transition et le rapport d'intensité  $I(K\alpha_3)/I(K\alpha_1) = (1.61 \pm 0.11) \times 10^{-4}$  obtenus sont en bon accord avec les valeurs expérimentales trouvées pour des éléments voisins et les résultats théoriques. Les transitions K-L<sub>2</sub>, K-M<sub>3</sub> et L<sub>2</sub>-M<sub>3</sub> de l'or ont ensuite été mesurées pour vérifier la précision du spectromètre à l'aide du principe de combinaison de Ritz.

Deux autres projets ont encore été réalisés pour contrôler les performances de l'instrument. Le premier a consisté à mesurer la série des rayons X L de l'or. Les énergies et largeurs naturelles de 13 transitions L ont pu être déterminées et comparées à d'autres valeurs existantes. En particulier, les satellites  $L\beta_2'$  et  $L\beta_2''$  de la raie  $L\beta_2$  (L<sub>3</sub>-N<sub>5</sub>) ont pu être résolus. La transition  $L\alpha_{1,2}$  (L<sub>3</sub>-M<sub>4,5</sub>) dont l'énergie n'est que de 9.7 keV a pu être observée. En fait, le domaine angulaire de  $\pm 20$  degrés couvert par le spectromètre et la constante réticulaire des plans de diffraction du cristal de quartz utilisé devraient permettre de mesurer des photons de 7.5 keV en premier ordre. Néanmoins, en raison de la très forte absorption des photons par les cristal en dessous de 10 keV, les spectromètres de type Laue ne sont en général pas employés à ces énergies, la plupart d'entre eux étant limités à la mesure de photons d'énergie supérieure à 20 keV. Dans le second projet, le spectromètre a été utilisé pour mesurer le coefficient d'absorption du molybdène ( $Z = 42$ )

dans la région du bord  $K$ . Les résultats obtenus ont été comparés avec ceux d'une autre expérience réalisée auprès d'une source de rayonnement synchrotron. Un très bon accord a été observé. D'autre part, à partir de ces mesures, l'énergie de liaison de la couche  $K$  du Mo a pu être déterminée. Une valeur de 20.00018(36) a été trouvée, en parfait accord avec les valeurs de référence existantes.

La seconde partie de la thèse est une étude des raies hypersatellites  $K\alpha^h$  ( $1s^{-2} \rightarrow 1s^{-1}2p^{-1}$ ) du Mo induites par photoionisation. Ces rayons X résultent de la désexcitation radiative d'états atomiques comprenant deux lacunes dans la couche  $K$ . L'expérience a été effectuée avec le spectromètre DuMond et un tube de rayons X avec anode d'or travaillant à 90 kV. En général, à cause des très faibles sections efficaces de double photoionisation  $K$  ainsi que de la présence dans la région d'énergie des hypersatellites des queues lorentziennes des raies diagrammes et du bruit de fonds résultant de la diffusion élastique par la cible des photons de bremsstrahlung du tube de rayons X, la mesure d'hypersatellites d'éléments mi-lourds utilisant un tube de rayons X pour la production de la fluorescence représente un défi expérimental particulièrement ardu. En fait, à notre connaissance, les mesures d'hypersatellites présentées dans ce travail sont les premières du genre.

Deux séries de mesures ont été réalisées, l'une sans absorbeur, l'autre avec un absorbeur formé de feuilles de niobium et d'yttrium superposées et placées entre le tube de rayons X et la cible de molybdène. Le rôle de l'absorbeur était d'améliorer le rapport signal-bruit en diminuant fortement le bruit de fonds dans la région d'énergie des hypersatellites. Plus précisément, la feuille de Nb servait à atténuer l'intensité des photons de bremsstrahlung ayant une énergie proche de celle des hypersatellites alors que la feuille d'Y servait à atténuer l'intensité des raies diagrammes et du même coup celle de leurs queues lorentziennes. A partir des spectres mesurés, les énergies et les largeurs naturelles des deux raies hypersatellites ainsi que le rapport d'intensité  $I(K\alpha_1^h)/I(K\alpha_2^h)$  ont pu être déterminés. Un bon accord avec les rares autres données expérimentales existantes et avec les résultats de calculs MCDF a été observé pour les énergies et les largeurs naturelles. Pour le rapport d'intensité, une valeur de  $1.4 \pm 0.5$  a été trouvée, laquelle est également consistante avec les prévisions théoriques et les valeurs expérimentales obtenues par

d'autres auteurs. Enfin, le rapport des sections efficaces  $\sigma_{KK}^{photo} / \sigma_K^{photo}$  a pu être déduit du rapport d'intensité  $I(K\alpha^h)/I(K\alpha)$  corrigé préalablement pour la différence entre les énergies moyennes des photons de bremsstrahlung contribuant à l'ionisation simple, respectivement double, et pour les nombres différents de ces photons. Une valeur de  $1.72 \times 10^{-4}$  a été trouvée pour le rapport des sections efficaces, un résultat deux fois plus petit que la seule autre valeur expérimentale existante dans la littérature pour le Mo.

Part I:

The DuMond curved crystal  
spectrometer

## 1. Introduction

For the detection of x-rays or  $\gamma$ -rays energy dispersive or wavelength dispersive instruments can be used. Gas proportional counters, scintillation detectors or semiconductor diodes belong to the first category while crystal spectrometers belong to the second one. Crystal spectrometers are characterized by a high resolving power of the order of  $10^4$  which is much better than the one of energy-dispersive detectors ( $\sim 10^1$ – $10^2$ ), a high precision and a good sensitivity. In contrast to that the efficiency of the wavelength dispersive detectors is much smaller than the one of energy dispersive detectors, mainly because of the small solid angles characterizing crystal spectrometers.

Many different types of crystal spectrometers have been developed until now. Flat crystal spectrometers provide the highest resolution and precision but their luminosity is extremely weak. To increase the solid angle, the crystal plate can be bent, cylindrically or spherically. Bending the crystal results in luminosity enhancements as big as  $10^2$ – $10^3$  with, however, some losses in the resolution, due to the geometrical aberrations related to imperfections in the curvature of the crystal plate and the quasi-mosaicity induced in the crystal lamina by the bending torque. For both flat and curved crystal spectrometers, Laue type (also named transmission type) and Bragg type (reflection type) instruments do exist. In Bragg type spectrometers the diffraction planes are parallel to the surface of the crystal exposed to the incoming radiation, whereas for Laue type spectrometers the diffraction planes are normal to the exposed surface. In the Laue case the photons have thus to travel through the crystal thickness to reach the detector. As a result, the intensity of the diffracted radiation is attenuated, being partly absorbed by the crystal. This absorption grows drastically when the photon energy decreases. For instance, for a 1 mm thick quartz plate, the absorption amounts to 4.0% at 100 keV, 46.3% at 20 keV and 99.3% at 10 keV! For this reason, transmission type crystal spectrometers cannot be employed for photon energies below about 10 keV. On the other hand, due to geometrical constraints related to the spectrometer design, the minimum Bragg angles sustainable by reflection type crystal spectrometers cannot be below about 20 deg. For standard crystals such as quartz, silicon and germanium with typical spacing lattice constants  $2d \approx 3$ – $5$  Å, Bragg angles  $\theta \geq 20$  deg. correspond to photon energies  $E \leq 7$ – $12$  keV so that Bragg type crystal spectrometers are usually employed for measuring photons below about 10 keV. In that sense Bragg type and Laue type crystal spectrometers can be considered as complementary high-resolution

instruments.

Most reflection type curved crystal spectrometers are operated in the Johann [1], Johansson [2] or von Hamos geometry [3–5], whereas for transmission type curved crystal spectrometers the DuMond [6] and Cauchois [7] geometries are the most commonly employed. For most geometries data collection is performed point by point: the angle between the crystal and the incoming radiation is increased step by step around the Bragg angle, the intensity of the diffracted radiation being measured for each angular step. The total acquisition time needed to measure a whole x-ray or  $\gamma$ -ray spectrum which is then given by the number of points in the spectrum multiplied by the acquisition time per point is rather long as compared to energy dispersive detectors. In the von Hamos geometry, for a fixed position of the crystal and detector, a certain angular range is covered by the crystal so that a whole energy interval can be measured at once. In this geometry, however, a position sensitive detector is needed and the width of the covered energy interval which depends on the Bragg angle is limited by the detector extension in the dispersive direction.

Curved crystal spectrometers of transmission type have proved to be an important tool in x-ray spectroscopy of transitions to the  $K$ -shell and  $L$ -subshells of heavy elements ( $Z > 40$ ). For the metrology of x-ray transitions, in which the natural line widths and the energies of the transitions are of interest, an instrumental broadening comparable to the widths of the atomic levels involved in the transitions and a relative precision of  $\sim 10^{-6}$  are indeed needed. Furthermore, in the  $K$  and  $L$  x-ray spectra of multiply ionized heavy atoms, the radiative decay of the multiple inner-shell vacancy states leads to the occurrence in the spectra of satellite x-ray lines which can be only resolved from their parent diagram lines by means of high-resolution instruments such as Laue type crystal spectrometers. The same holds for  $\gamma$ -ray spectroscopy measurements of odd-odd unstable nuclei. To unravel the spectra of such radioactive isotopes characterized by large densities of close-lying  $\gamma$ -rays, the use of high-resolution instruments is also mandatory.

A major progress in determining the energy and intensity of electromagnetic radiation in complex spectra was made by DuMond in 1947 [6] with his development of the line source curved crystal transmission spectrometer. The DuMond geometry, in which the crystal is bent cylindrically, requires that the radius of curvature of the crystal is equal



to the diameter of the so-called Rowland circle (focal circle) and that the center of the radiation source and the center of the crystal are located on opposite sides of the Rowland circle. If these geometrical conditions are fulfilled, then for a particular photon energy the Bragg law is satisfied over the whole area of the crystal. In the original DuMond spectrometer a quartz crystal plate of dimensions  $80 \times 70 \times 1 \text{ mm}^3$  was bent to a radius of 2 meters with the (310) reflecting planes normal to the surface. During the measurement the source of radiation was moved along the focal circle and the intensity of the diffracted radiation, transmitted through the crystal, was measured for each position of the source by a dedicated multi-cellular Geiger-Müller counting tube of high efficiency. To shield the detector from the directly transmitted and the scattered radiation beams, a multiple-slit collimator was inserted by DuMond between the bent crystal and the detector. This collimator allowed him to extend his measurement to the domain of small Bragg angles, i.e. to the high energy region. The spectrum was constructed by plotting the detector count rate as a function of the Bragg angle, i.e. the angle between the incident x-ray beam and the reflecting planes of the crystal.

Since that pioneering work many spectrometers based on the DuMond geometry have been constructed [8–16]. In most of them the radiation source is no longer a  $\gamma$ -ray radioactive source as in the case of DuMond but a target placed in a beam line of a nuclear reactor (for n- $\gamma$  spectroscopy measurements), a heavy-ion (HI) accelerator (for HI-induced nuclear reactions or HI-induced multiple atomic inner-shell ionization studies) or a synchrotron radiation facility (for photoionization and metrology of x-ray transition measurements and resonant elastic and inelastic scattering experiments). In all these applications, the source can no longer be moved along the Rowland circle to vary the Bragg angle. For in-house experiments employing x-ray tubes or electron guns for the production of the target x-ray fluorescence, the samples have also to be kept fixed to avoid a new adjustment of the x-ray tube or electron gun after each target displacement. The Bragg angle is then varied by rotating the crystal and the detector around the same axis passing through the center of the crystal plate. When the crystal is rotated by an angle  $\theta$ , the detector has to be rotated by  $2\theta$ . Furthermore, as the Rowland circle rotates with the crystal, after a crystal rotation the source of radiation is no longer on the focal circle and the apparent width of the source becomes wider, which leads to a resolution loss of the

instrument. In DuMond spectrometers operated with a fixed source, the focusing distance, i.e. the distance between the crystal and the source, has therefore to be adjusted whenever the defocusing distance resulting from the change in the Bragg angle exceeds a value of the order of  $\sim R/1000$ , where  $R$  is the radius of curvature of the crystal.

Thanks to the considerable developments made during the last decades in electronics and informatics modern DuMond crystal spectrometers are now equipped with sophisticated detector systems and the Bragg angles are determined with high accuracy by means of laser interferometers. Recent spectrometers are operated in a fully automatic way by computers which control also the data acquisition. Regarding the crystals, the know-how acquired at synchrotron radiation facilities in the preparation of ultra pure crystals and development of new bending devices have been also of great benefit. However, despite these improvements the basic mechanical design and the working principles of modern spectrometers have remained essentially the same as those of the DuMond prototype.

In the first part of this thesis the high-resolution DuMond type curved crystal spectrometer installed at the University of Fribourg and more specifically the new software that was developed to operate this instrument are presented. The spectrometer which was constructed several years ago for high-resolution studies of photoinduced x-ray spectra can be used for photon energies above about 10 keV. Thanks to its very good energy resolution (about 3 eV at 15 keV) and high precision (about 0.003 eV at 15 keV), this spectrometer represents an ideal tool for the metrology of  $K$  and  $L$  x-ray transitions of heavy elements. Furthermore, the very low background of the instrument ( $4 \cdot 10^{-3}$  count $\cdot$ s $^{-1} \cdot$ keV $^{-1}$  at 10 keV and  $10^{-3}$  count $\cdot$ s $^{-1} \cdot$ keV $^{-1}$  above 20 keV) makes it particularly adequate for the measurements of x-ray emission lines which are characterized by extremely low transition probabilities. Initially, the spectrometer and the data acquisition were controlled by a PEP Modular Computer System. Because of the high costs related to the maintenance of this old computer and the increasing difficulties to find spare parts for it as well as because the software was not really user friendly, a new LabVIEW-based software was developed to control the spectrometer and acquire data via a standard PC.

A brief reminder of the basic principles of x-ray diffraction by crystals is given in Sect. 2. Construction details and performances of the DuMond curved crystal spectrometer along with the new LabVIEW program are described in Sect. 3, whereas several examples

of applications are presented in Sect. 4.

## 2. Bragg law and structure factor

In a crystal the atoms are uniformly placed in virtual, regularly spaced, parallel planes. Because the wavelength of x-rays (from about 0.1 nm to about 10 nm) or  $\gamma$ -rays (less than about 1 nm) is comparable to the spacing between atoms in the crystal, they are ideally suited for probing the structural arrangement of atoms in materials. With visible light it is not possible to investigate the crystalline structure because visible light has wavelengths much larger than the distance between the atoms in a crystal. For example yellow light has a wavelength of 570–580 nm, whereas the distance between the nearest atoms in a NaCl crystal is only 0.28 nm. Furthermore, energetic x-rays or  $\gamma$ -rays can penetrate into the materials and provide information about their bulk structure.

In x-ray or  $\gamma$ -ray spectrometry it is the energy of the radiation rather than the wavelength which is of interest. The wavelength  $\lambda$  [ $\text{\AA}$ ] of the x-ray or  $\gamma$ -ray as a function of the photon energy  $E$  [keV] is given by the relation:

$$\lambda = \frac{h \cdot c}{E} = \frac{12.398419 [\text{keV} \cdot \text{\AA}]}{E [\text{keV}]}, \quad (1)$$

where  $h$  is the Planck constant and  $c$  the velocity of light in vacuum.

The x-rays or  $\gamma$ -rays are diffracted by the crystal. The condition for a constructive interference after the diffraction by different atomic planes of the crystal is given by the Bragg equation:

$$2d_{hkl} \cdot \sin \theta = n\lambda, \quad (2)$$

where  $n$  is the order of diffraction,  $\lambda$  the wavelength of the incident x-rays or  $\gamma$ -rays and  $d_{hkl}$  is the lattice constant of the crystal for the diffraction planes corresponding to the Miller's indices  $(hkl)$ , i.e. the distance between adjacent  $(hkl)$  planes. For cubic crystals such as silicon and germanium, the spacing lattice constant  $d_{hkl}$  is given by [17]:

$$d_{hkl} = \frac{a}{\sqrt{h^2 + k^2 + l^2}}, \quad (3)$$

where  $a$  is the crystal constant ( $a = 5.43070 \text{ \AA}$  for Si,  $a = 5.65735 \text{ \AA}$  for Ge).

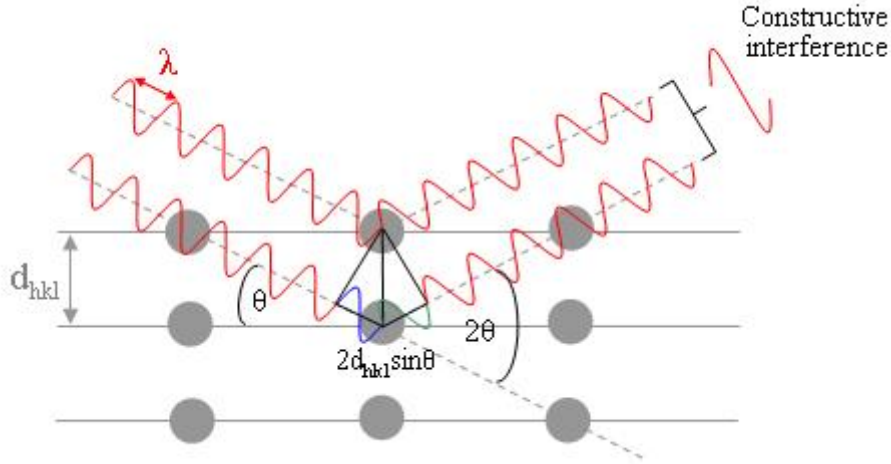


FIGURE 1: Schematic diagram for determining the Bragg law. The beam diffracted from the second plane travels a distance  $2d \cdot \sin\theta$  longer than the beam reflected from the first plane.

For hexagonal crystals like quartz ( $\text{SiO}_2$ ),  $d_{hkl}$  can be obtained from [17]:

$$d_{hkl} = \frac{1}{\sqrt{\frac{4(h^2 + hk + k^2)}{3a^2} + \frac{l^2}{c^2}}}, \quad (4)$$

where  $a$  and  $c$  are the crystal constants (for  $\text{SiO}_2$ ,  $a = 4.91304 \text{ \AA}$  and  $c = 5.40463 \text{ \AA}$ ). The Bragg equation shows that the path difference  $2d \cdot \sin\theta$  for waves diffracted by different atomic planes should be equal to an integer number of the wavelengths  $\lambda$  [see Fig. 1]. When a constructive interference occurs the diffracted beam of x-rays or  $\gamma$ -rays leaves the crystal under an angle equal to the one of the incident beam. For a given wavelength and diffraction order constructive interferences are only possible for a given incident angle. Each angle corresponds thus to a particular wavelength and diffraction order and varies with the lattice spacing constant of the crystal. The two geometries in which the Bragg condition can be realized are shown in Fig. 2. The diffraction geometry shown in Fig. 2a is commonly referred to as the Bragg or reflection case, while the one shown in Fig. 2b is called the Laue or transmission case.

The Bragg law is a necessary but not sufficient condition to observe constructive interferences. Actually, the amplitudes and relative phases of the x-rays scattered by the

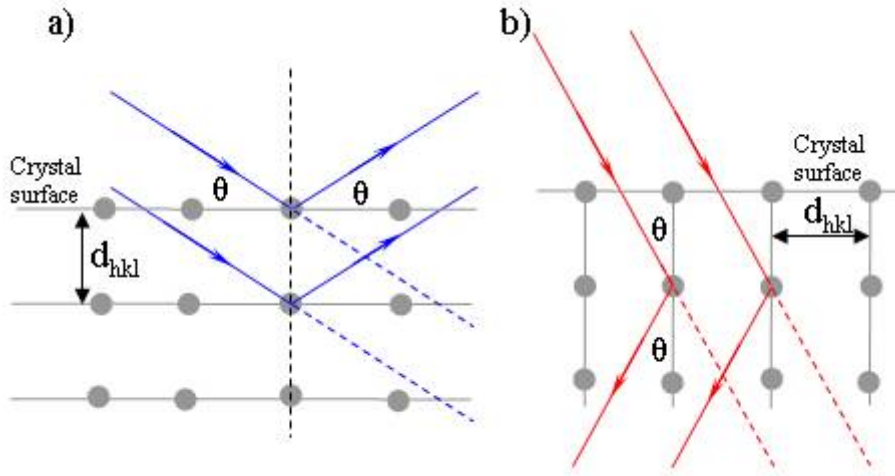


FIGURE 2: Bragg (a) and Laue (b) diffraction cases.

individual atoms in the unit cell are given by the crystal structure factor  $F_{hkl}$  defined by:

$$F_{hkl} = \sum_{j=1}^N f_j \cdot e^{2\pi i(h \cdot x_j + k \cdot y_j + l \cdot z_j)}, \quad (5)$$

where  $f_j$  stands for the atomic scattering factor of the  $j$ -th atom whose position in the unit cell is given by the coordinates  $x_j, y_j, z_j$  and  $N$  is the number of atoms in the unit cell of the crystal. The atomic scattering factor  $f_j$  corresponds to the ratio between the amplitude scattered by the atom  $j$  and the one scattered by an isolated electron, under identical conditions. Clearly the maximum value that  $f_j$  can have is  $Z$  (atomic number of the atom  $j$ ). When  $f_j = Z$  all the electrons scatter in phase with each other. As the intensity of a wave is given by the squared amplitude of the latter, the intensity of the photon beam diffracted by the planes  $(hkl)$  is proportional to the square of the modulus of the structure factor  $F_{hkl}$ :

$$I_{hkl} \propto |F_{hkl}|^2 = F_{hkl}^* \cdot F_{hkl}, \quad (6)$$

where  $F_{hkl}^*$  is the complex conjugate of  $F_{hkl}$ . For face centered cubic crystals like silicon and germanium, the structure factor  $F_{hkl} \neq 0$  only when all Miller indices are odd or all are even. In other words, for face centered cubic crystals there is no diffracted intensity if the Miller indices are mixed. For instance, no reflection is observed for the  $(110)$  planes of Ge

but a strong reflection is observed for Ge(220) which is equivalent to Ge(110) in second order of diffraction ( $n = 2$  in the Bragg law). For hexagonal crystals like quartz ( $\text{SiO}_2$ ), reflection by  $(00\ell)$  planes is only possible when  $\ell$  is a multiple of 3. For most common crystals, the structure factors  $F_{hkl}$  can be calculated with the computer code XOP [18].

## 3. The DuMond crystal spectrometer of Fribourg

### 3.1. Spectrometer design

#### 3.1.1 Overview of the instrument

In the DuMond geometry, the radiation source must be a line-like source. For this reason the radioactive source or the irradiated target should be very thin ( $\sim 0.01$ – $0.10$  mm) and perfectly aligned with the source–crystal direction. In order to achieve an acceptable source strength, the tiny target width is compensated by a large depth ( $\sim 5$  mm). This target geometry which was introduced by DuMond represents still the standard geometry for  $\gamma$ –ray measurements. For x–rays, however, whose energies are in general lower than those of  $\gamma$ –rays, this geometry is less appropriate because the x–rays produced in the depth of the target are almost fully absorbed by the target itself. Therefore, for x–ray spectroscopy measurements the spectrometer is usually operated in the so–called modified DuMond slit geometry. In this geometry represented schematically in Fig. 3, a narrow rectangular slit is placed on the focal circle at a fixed position and serves as the effective source of radiation. The target placed behind the slit can be tilted around a vertical axis to make a certain angle with respect to the target–crystal direction. For a given x–ray line, the angle is chosen so that the highest counting rate is obtained in the spectrometer detector. The variation of the counting rate as a function of the target alignment depends on the self–absorption of the x–rays in the target and the size of the target surface viewed by the crystal through the slit. Both quantities decrease with growing angles but with opposite effects on the counting rate. Two further advantages are provided by this geometry: first the slit width can be adjusted to obtain the desired instrumental resolution and secondly the line shapes of the measured x–rays are no more affected by thermal deformations of the target.

A side view of the spectrometer is shown in Fig. 4. The most important parts of the instrument are the target chamber, crystal, optical laser interferometer, collimator and detector which are described in more details in the next sub–sections. A photograph of the spectrometer is presented in Fig. 5. The x–rays diffracted by the curved crystal are recorded by a Phoswich scintillation detector. In front of the detector a Soller slit collimator permits to shield the detector from the radiation coming directly from the



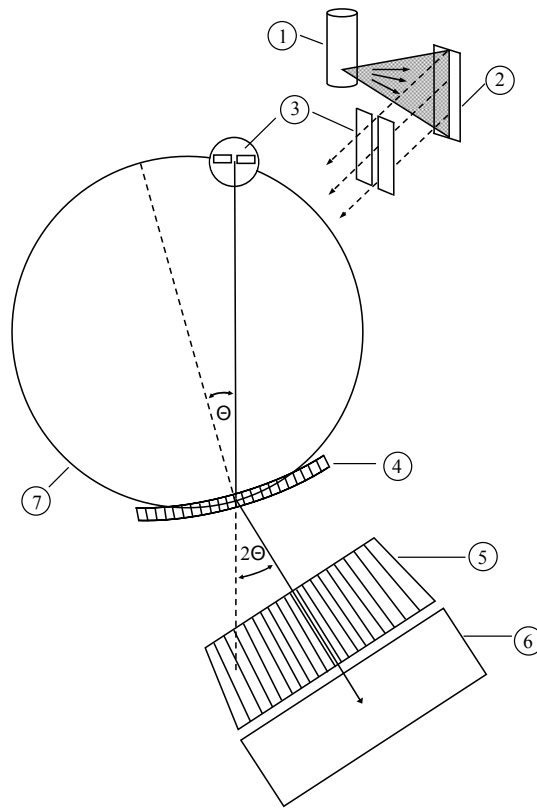


FIGURE 3: Schematic drawing of the modified DuMond slit geometry: (1) x-ray tube, (2) target, (3) slit, (4) cylindrically bent crystal, (5) Soller slit collimator, (6) detector and (7) focal circle.

source. The Bragg angles are measured by means of an optical laser interferometer with a precision of approximately  $5 \cdot 10^{-3}$  arcsec. The most temperature-sensitive elements of the spectrometer, namely the laser interferometer and the bent crystal, are enclosed in a double thermostatic housing which keeps their temperature constant around  $23 \text{ }^{\circ}\text{C}$  with a precision better than  $0.05 \text{ }^{\circ}\text{C}$ . The angular range covered by the spectrometer is  $\pm 20 \text{ deg}$ . For the (110) reflecting planes of a quartz crystal ( $d \approx 2.456 \text{ \AA}$ ) this maximum angle of  $20 \text{ deg}$ . corresponds theoretically to a minimum photon energy of about  $7.5 \text{ keV}$  in first order of reflection. Actually, due to the absorption of the x-rays in the crystal, the true minimum energy lies somewhat higher (at about  $9 \text{ keV}$ , see Sect. 4).

As the diffraction planes are not exactly perpendicular to the front surface of the crystal plate (depending on the crystal, cut errors of several minutes of arc can be observed), two different “zero” positions of the spectrometer are defined. The first one called the “mechanical zero position” corresponds to the position at which the laser

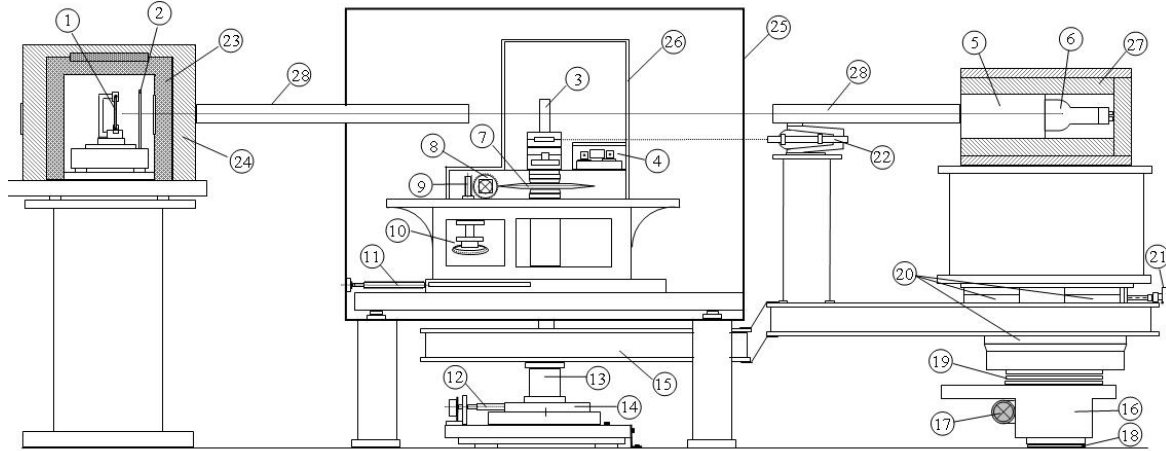


FIGURE 4: Side view of the DuMond crystal spectrometer: (1) target, (2) slit, (3) crystal, (4) optical laser interferometer, (5) Soller slit–collimator, (6) detector, (7) large tooth wheel, (8) small tooth wheel and second worm gear (behind), (9) first worm gear, (10) stepping motor for the crystal rotation, (11) screw rod for the crystal focusing, (12) screw rod for the detector axis focusing, (13) detector rotation spindle, (14) movable table of the detector rotation spindle, (15) detector rotation arm, (16) detector automotive carriage, (17) step motor of the detector carriage, (18) circular rail, (19) large ball bearing, (20) Schneeberger minirails, (21) manual adjustment of the collimator position, (22) laser of the detector position optical tracking system, (23) target chamber, (24) lead shielding, (25) external thermostatic housing, (26) internal thermostatic housing, (27) lead shielding, (28) evacuated pipe.

interferometer has to be reset for a correct determination of the Bragg angles. This “mechanical zero position” which corresponds to the value of 1'000'000 in the electronic register *CRY* where the crystal position is saved (in units of motor steps) is fixed with respect to the mechanical crystal rotation system. If for any reason, the electronic position is lost (for instance after a power supply failure) the correct “mechanical zero position” can be restored thanks to reference marks indicated on the stepping motor and both tooth wheels. The second “zero” position named the “spectroscopic zero position” corresponds to the origin of the Bragg angle scale. As the design of the spectrometer permits to rotate clockwise and anticlockwise the crystal and the detector, the “spectroscopic zero position”  $\theta_0$  can be simply determined by measuring the same line on both sides of reflection and using the following relation:

$$\theta_0 = \frac{\theta_+ + \theta_-}{2}, \quad (7)$$

where  $\theta_+$  and  $\theta_-$  are the Bragg angles corresponding to the line measured on the right (positive angles) and left (negative angles) sides of reflection. The “spectroscopic zero position” is not constant and varies with the employed crystal and position of the slit. It varies also slightly with the focal distance, i.e. the distance between the crystal and the slit, so that a new determination of this “zero” has to be done whenever the focal distance of the spectrometer is changed.

As mentioned before to preserve the angular resolution of the spectrometer, the source of radiation, the slit in our case, should be kept on the focal circle when the crystal is rotated. As shown in Fig. 3 the distance  $f$  between the crystal and the slit is given by:

$$f = R \cdot \cos \theta, \quad (8)$$

where  $R$  stands for the radius of curvature of the crystal. The focal distance  $f$  is changed by moving the whole crystal part, i.e. the crystal itself, the crystal rotation system and the laser interferometer, along the crystal–source direction with a screw rod driven by a step motor.

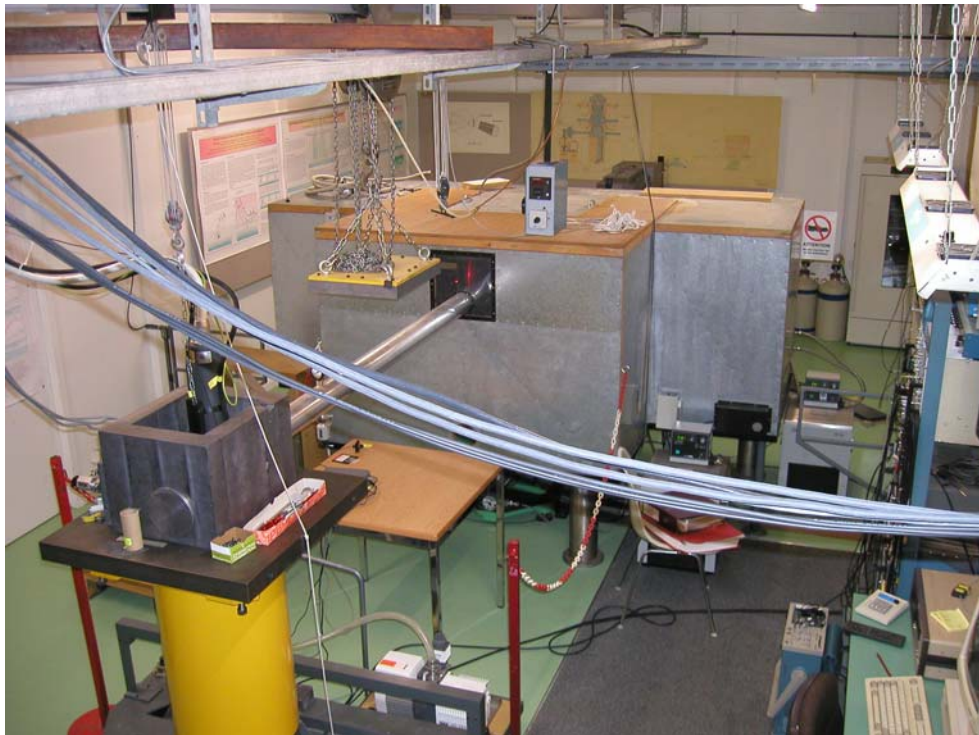


*FIGURE 5: Photograph of the DuMond curved crystal spectrometer.*

The origin of the crystal focusing axis named *FOC* corresponds to a value of 100'000 [motor steps] in the position register of the motor driving the screw rod of the crystal focusing system. The change of the focal distance is 5  $\mu\text{m}$  per motor step. The origin of the axis ( $FOC = 100'000$ ) was defined to correspond to a distance of 315 cm between the crystal and the target. The positive direction of the axis was chosen to point towards the slit so that *FOC* values bigger than 100'000 correspond to focal distances smaller than 315 cm. As the slit is placed in front of the target at a distance  $d$  from it, the *FOC* value corresponding to the Bragg angle  $\theta$  is given by:

$$[FOC(\theta) - 100'000] \cdot 5 \cdot 10^{-4} [\text{cm}] + R[\text{cm}] \cdot \cos \theta + d[\text{cm}] = 315[\text{cm}], \Rightarrow \quad (9a)$$

$$FOC(\theta)[\text{steps}] = 100'000 + \frac{315 - R[\text{cm}] \cdot \cos \theta - d[\text{cm}]}{5 \cdot 10^{-4}}. \quad (9b)$$

As in the DuMond geometry the rotation spindles of the crystal and detector should remain coaxial, the spindle of the detector should be also moved when the *FOC* value is changed. This is realized automatically with a step motor named *FOP* and a second optical tracking system which forces the detector axis *FOP* to remain aligned with the *FOC* axis during a focusing operation.

### 3.1.2 Target chamber

As mentioned before the x-ray source is defined by a rectangular slit located on the focal circle of the spectrometer at a fixed position. The slit is made of two juxtaposed lead plates which are 40 mm high, 6 mm width and 5 mm thick. The distance between the two plates, i.e. the slit width, can be adjusted. If the slit width is increased, a wider part of the target surface is viewed by the crystal and the luminosity of the spectrometer is enhanced but the instrumental resolution becomes worse. In most applications, the slit width is chosen to correspond to the best compromise between a high enough luminosity and an acceptable instrumental resolution. Typical employed slit widths are 0.05 mm, 0.10 mm and 0.15 mm.

Most targets consist of 27 mm high  $\times$  4 mm wide metallic foils. Thicknesses vary from  $\sim 10^{-3}$  mm to  $\sim 10^{-1}$  mm. The foils are kept stretched by a spring in a dedicated holder

as shown in Fig. 6. Powder samples can also be used. They are prepared by dusting the powder onto a thin adhesive backing having similar dimensions as the metallic foils. The alignment and verticality of the targets can be adjusted by means of remote-controlled step motors named *SAL* (Source Alignment) and *SVE* (Source verticality). As mentioned before, for a given x-ray line, the alignment angle of the target is chosen so that the highest count rate is obtained in the spectrometer detector. Similarly, the vertical position of the sample is optimized in order to get the best resolution. The latter is obtained when the vertical axes of the sample and diffraction planes of the crystal are parallel. The smallest angular steps that can be made with the *SAL* and *SVE* systems are 0.225 deg. and 0.00083 deg., respectively. The transverse position of the slit can also be adjusted via a third remote-controlled step motor (*SLT*). One step of the *SLT* motor produces a 1.0  $\mu\text{m}$  displacement of the slit along an axis perpendicular to the target-crystal direction. For optimal operation, the center of the slit should be located on the straight line joining the center of the target and the center of the crystal. For gaseous samples, the target holder is replaced by a 3 cm in diameter and 3 cm high circular cell with an 11  $\text{mg}/\text{cm}^2$  thick kapton wall. Gas pressures up to 3 bars can be used. Other target cells with metallic or polymeric walls were developed for liquid targets such as Hg. The distance  $d$  between the slit center and the vertical axis of the solid target or the gaseous or liquid cell can be varied between 1.75 cm and 4.75 cm.

The target fluorescence is produced by irradiating the samples with the bremsstrahlung of side-window Coolidge-type x-ray tubes. Depending on the projects,

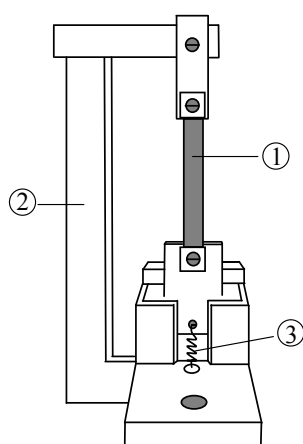


FIGURE 6: Target holder with (1) target, (2) aluminum frame and (3) spring.

x-ray tubes equipped with anodes of Au (1 mm Be window), Cr (0.5 mm Be window) and Sc (0.3 mm and 0.15 mm Be windows) can be used. The bremsstrahlung and the characteristic x-ray radiation of the tube are emitted in a cone having an aperture of about 30 deg. The x-ray tube is mounted vertically on a circular port on the top of the target chamber with the side-window in the direction of the target. The x-ray tube port can be rotated around a vertical axis passing through the center of the sample for performing angular distribution measurements. The angle between the axis of the x-ray tube beam and the target-crystal direction can be varied this way between 30 and 150 deg. with angular steps of 30 deg. The water-cooled x-ray tubes are connected to a 100 kV/3 kW high-voltage generator equipped with an automatic regulation system for the stabilization of the current and voltage.

The slit, the target and the nose of the x-ray tube are all enclosed in a 25 cm long  $\times$  25 cm wide  $\times$  15 cm high vacuum chamber with 2 cm thick iron walls. In the center of the front wall, a circular 0.2 mm thick mylar window permits the exit of the fluorescence x-rays. For safety reasons, the target chamber is enclosed in a 5 cm thick lead shielding and an automatic security system switches off the high-voltage generator if the x-ray tube port on the top of the target chamber or the two fences permitting the access to the rear part of the spectrometer are not closed. When the x-ray tube is on, the target chamber is pumped down to about  $10^{-2}$  mbar with a rotary pump in order to minimize the oxidation of the sample, slit and target chamber walls.

### *3.1.3 Crystal and crystal rotation mechanism*

The spectrometer can be equipped with different high-quality single crystals such as quartz, silicon or germanium. For x-ray measurements, quartz crystal plates are usually employed because, for the same thickness, the absorption is higher in silicon and even more in germanium. Several quartz crystal plates with different orientations and different thicknesses are available. For the present work a 100 mm high  $\times$  100 mm wide  $\times$  0.5 mm thick quartz was employed. The plate was cut so that the (110) diffraction planes were normal to the front surface. In general, the instrumental resolution can be improved by increasing the radius of curvature of the crystal, but because the solid angle is then smaller

the collection efficiency decreases. On the other hand the luminosity loss can be compensated by choosing a larger crystal area, but this may result in geometrical aberrations when the crystal is bent. For these reasons, a radius of curvature of 315 cm was chosen as the best compromise between a high enough resolution and an acceptable luminosity.

The choice of the best crystal thickness depends on the reflectivity of the crystal and the absorption of the x-rays. The reflectivity grows with the crystal thickness as long as the latter is comparable to the extinction length (the length after which the intensity of the incident photons has decreased by a factor  $e \cong 2.718$ ). For x-rays with energies less than about 100 keV, the extinction length of quartz is of the order of several hundreds of  $\mu\text{m}$ . Concerning the absorption, it is well known that the latter increases exponentially with the absorber thickness. Therefore a 0.5 mm thick quartz crystal was chosen as the best compromise.

In the standard bending technique, the crystal is pressed between two clamping blocks, machined out beforehand to have a precise convex cylindrical surface on the crystal side for the front block, respectively a concave cylindrical surface for the rear block. The crystal radius of curvature is determined by the radius of the cylindrical surfaces. Trapezoidal windows in the front and rear clamping blocks permit the transmission of the x-rays. The dimensions of these windows define the effective reflecting area of the crystal. To obtain a precise and constant curvature over the whole surface of the crystal, the latter should be very well polished and its thickness has to be constant at the level of about 0.01  $\mu\text{m}$ . Such conditions are almost impossible to satisfy with crystal laminas thinner than 1 mm so that thin crystal plates are difficult to bend with the standard bending technique. For this reason a novel dedicated bending device was developed. A schematic drawing and a photograph of this device are shown in Fig. 7. In this case the crystal (1) is clamped between two pairs of flat steel blocks (2). The two blocks of each pair are pressed together with two screws passing above, respectively below, the crystal plate. The force which maintains the two blocks together can be adjusted with two springs. The block pairs can rotate around the vertical axes (6). The latter are placed symmetrically with respect to the center of the crystal and the distance between them corresponds to one fourth of the crystal length. The bending torque is

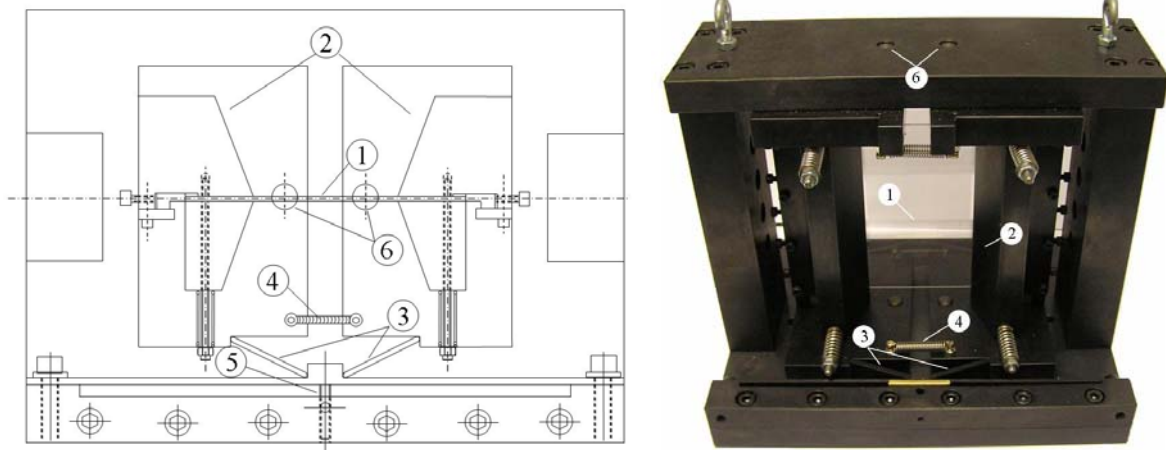


FIGURE 7: Schematic diagram (top view) and photograph (view from the backside) of the bending device: (1) crystal lamina, (2) clamping blocks, (3) lever arms, (4) restoring springs, (5) bending screw and (6) clamping block axes.

applied to the crystal via the pairs of clamping blocks through the lever arms (3) using the screw (5). The torque that should be applied depends on the thickness of the crystal plate and on the restoring force exerted by the two springs (4). The main difficulty here is to apply the torque as symmetrically as possible on both sides of the crystal. Only in this case the crystal will be given the correct cylindrical shape.

In principle, with the novel bending device, the whole height of the crystal can be used. However, as a result of the bending torque a second curvature along the vertical axis is induced in the crystal plate. The magnitude of this so-called saddle effect depends on the values of the elasticity tensor components of the crystal and on the particular orientation of the crystal cut. It leads to geometrical aberrations that increase with the vertical distance between the incidence point of the photon and the crystal center. As a consequence, the top and bottom parts of the crystal cannot be used if the best resolution is needed. For this reason, in most applications described in the present work (see Sect. 4), only the central part of the crystal was employed so that the effective reflecting area was  $4 \times 3 \text{ cm}^2$  and the solid angle of the spectrometer about  $1.2 \times 10^{-4} \text{ sr}$ . The two pairs of blocks are made of hardened stainless steel which is characterized by a long term mechanical stability. In addition the crystal and bending device are enclosed in a thermostatic house where the temperature fluctuations are kept below  $0.05 \text{ }^\circ\text{C}$  throughout the year. This is needed to keep constant the crystal radius of curvature, any change of the latter resulting



in a deterioration of the instrumental response of the spectrometer.

The crystal is rotated by means of a high precision two-stage tooth wheel mechanism (Fig. 8). The 100 mm in diameter rotation axis is mounted in a ball-cage bearing. Thanks to a static compression of the balls of 5  $\mu\text{m}$ , an accuracy of about 0.2  $\mu\text{m}$  is obtained for the crystal axis position. The crystal rotation is driven by a step motor and two worm gears in cascade. The big wheel fitted to the crystal axis has 360 teeth and is 440 mm in diameter. It is driven by the horizontal worm gear. The smaller wheel with 60 teeth is 120 mm in diameter and is driven by the vertical worm gear which is directly connected to the step motor. The total gearing ratio is 1:21'600 so that one motor step of 0.45 deg. corresponds to a crystal rotation of 0.075 arcsec. To minimize friction and thermal dilatations of the moving parts, the choice of the materials is crucial. The big tooth wheel is made of cast iron, the two worm gears of special hardened and polished steel and the small tooth wheel of a bronze alloy. Furthermore, in order to keep the backlash of the system at a small value, a constant restoring torque of about 2.5 Nm provided by a counterweight of lead is applied to the big tooth wheel. The reproducibility of the rotation mechanism was probed and found to be of the order of 0.15 arcsec, whereas the observed maximal nonlinearities amount to about  $\pm 5$  arcsec. Each crystal rotation is carried out via an acceleration – constant speed – deceleration sequence. In other words, the angular velocity of the step motor is first linearly increased up to a preset maximum value, kept then constant at this value as long as the angular difference with respect to the final position is smaller than 60 arcsec and finally decreased linearly from the maximum value down to a speed of a few steps/sec. when the final position is reached. The acceleration and deceleration ranges are 800 steps long and the maximum motor speed is 1400 steps/sec., which corresponds for the crystal rotation axis to an angular velocity of about 1/35 deg./sec. This mode of operation of the step motor permits a smoother and therefore more accurate rotation of the crystal.

As mentioned before the slit-to-crystal distance should be adjusted for each measurement in order to keep the x-ray source on the focal circle. On the other hand the crystal and collimator rotation axes have to be aligned in the vertical direction. For this reason, when the focusing distance is changed the crystal and the collimator axes have to be moved together. The collimator itself, however, must be kept fixed during the

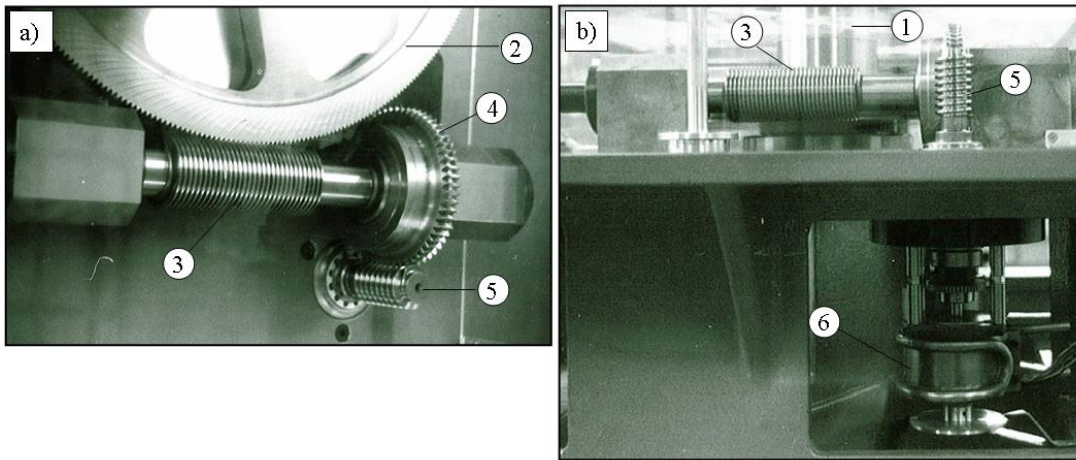


FIGURE 8: Photographs of the crystal tooth wheel mechanism a) top view b) side view: (1) crystal axis, (2) big wheel with 360 teeth, (3) horizontal worm gear, (4) small wheel with 60 teeth, (5) vertical worm gear coupled to the step motor, (6) step motor.

displacement of the axes. This is realized by a dedicated focusing mechanism which consists of two step motors, one for each axis, an optical tracking system and a double jamming device. The optical tracking system keeps the collimator axis vertically aligned to the crystal axis when the latter is moving. During the displacement the pneumatic jamming device, which allows the collimator axis to be fixed to the collimator carrier, is released and the collimator is blocked on the carriage by an electromagnetic jamming device. Note that during the data acquisition the situation is inversed, i.e., the pneumatic jamming system is active and the electromagnetic one is released (see also Sect. 3.1.5).

### 3.1.4 Optical laser interferometer

The Bragg angles are measured by means of an optical laser interferometer with a precision of several milli-arcsec over the  $\pm 20$  deg. angular range of the spectrometer. The schematic layout of the interferometer is represented in Fig. 9. A dedicated He-Ne laser developed by Hewlett-Packard for industrial linear displacement measurements [19] emits two beams of red light with slightly different optical frequencies,  $f_1$  and  $f_2$ . The frequency difference  $f_1 - f_2$  of about 2 MHz which is obtained by using the laser transitions from two adjacent Zeeman sublevels is very stable and represents the reference signal of the

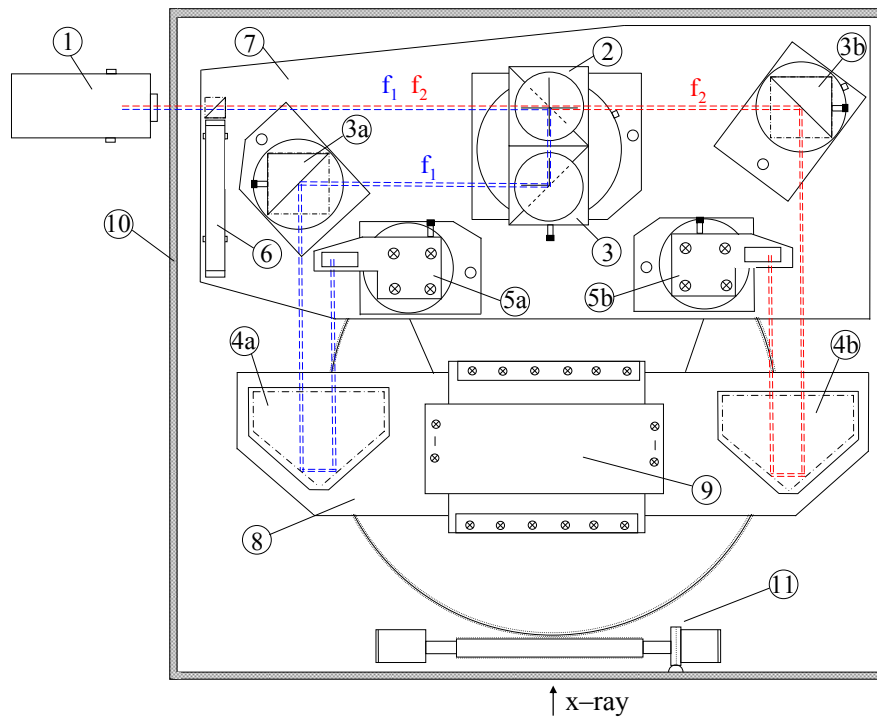


FIGURE 9: Top view of the optical laser interferometer: (1) two-frequency HP laser, (2) beam splitter, (3, 3a, 3b) plane mirrors, (4a, 4b) cube corner reflectors, (5a, 5b) roof prisms (end reflectors), (6) photodetector, (7) fixed table, (8) rotary table, (9) crystal bending device, (10) thermostatic box, (11) driving system of the crystal.

interferometer. Both beams are polarized linearly, the first one in the horizontal plane, the second one in the vertical plane, so that the two signals can be separated by optical elements sensitive to the direction of polarization. The double beam is directed to the beam splitter (2) which separates the two components according to their polarization. The beam  $f_1$ , deflected by the mirrors (3) and (3a) and by the cube corner reflector (4a), reaches the roof prism (end reflector) (5a). The latter reflects the beam which is redirected to the beam splitter by the same optical elements but along a lower lying path. In the beam splitter the beam  $f_1$  is recombined with the beam  $f_2$  which has followed a similar path on the other side of the interferometer. The two beams interfere then in the photodetector (6) which provides an electric signal whose frequency corresponds to the beat frequency of the two beams.

The crystal and all optical elements of the interferometer, the laser excepted, are enclosed in a thermostatic box where the temperature is kept constant within  $\pm 0.05^\circ\text{C}$  by

means of Peltier elements. The box contains two tables. A fixed one, which is used as a support for all optical elements, except the cube corner reflectors, and a rotary one, fixed to the crystal rotation axis, which supports the crystal bending device and the two cube corner prisms. When the rotary table is not moving, the frequency of the beat signal provided by the photodetector is the same as the reference frequency given by the laser so that the angle measured by the system remains unchanged. However, as soon as the table is rotated, due to the displacement of the cube corner reflectors which are moving in opposite directions, the two frequencies  $f_1$  and  $f_2$  are Doppler shifted, one frequency being increased, the other one decreased, and the beat frequency provided by the detector is no longer equal to the reference frequency. The HP controller receives the reference and measured signals, processes them and determines the actual crystal angle in optical units with respect to the mechanical zero position at which the interferometer was set to zero. Actually, as the system was developed by HP for linear displacement measurements, one optical unit corresponds to a difference of  $\lambda/40$  between the optical paths of the two beams. A more detailed description of a similar interferometer and some theoretical calculations are given in Ref. [20].

The method consisting of measuring the optical path difference between the two beams via the Doppler effect instead of counting the interference fringes presents the great advantage to be less sensitive to the frequency instability of the laser because both light beams are affected in the same way. However, as the measured displacements of the cube corners during a rotation are determined through the frequency changes of the two beams but are expressed in units of  $\lambda/40$ , the light velocity inside the thermostatic housing must be known. For this reason, the temperature, pressure and humidity of air inside the thermostatic box are measured by the system. From the obtained values the HP controller computes the so-called compensation factor (ratio between the light velocity in the thermostatic house and in vacuum) and multiplies then the interferometer value by the calculated compensation factor. The corrected interferometer value, compensation factor, air temperature, air pressure and air humidity, as well as the temperature of the rotary table, can be obtained from the controller via the VME crate and a GPIB interface.

As the values provided by the interferometer correspond to optical path differences between the two laser beams and not directly to the angle made by the crystal with respect

to the mechanical zero position, the interferometer was calibrated, using a Moore rotary table [21] and a Hilger–Watts TA53 autocollimator. The combination of these two instruments permitted us to determine 241 crystal angles between  $-20$  deg. and  $+20$  deg. with an angular step of 600 arcsec and a precision of 0.2 arcsec. For each angle the corresponding interferometer value was determined.

The crystal angle with respect to the mechanical zero position where the interferometer register is set to zero can be calculated from the following 7<sup>th</sup> order interpolation polynomial:

$$\theta(x) = a_1x + a_2x^2 + \dots + a_7x^7, \quad (10)$$

where  $\theta$  stands for the crystal angle in [rad] and  $x$  for the interferometer value in [optical units $\cdot 10^{-7}$ ]. The polynomial coefficients  $a_i$  were determined from the above mentioned calibration, using a least–squares fit method. The obtained values are given in Table I.

TABLE I: Coefficients of the interpolation polynomial of the laser interferometer.

$a_1$	$5.45706743 \cdot 10^{-2}$
$a_2$	$6.58150153 \cdot 10^{-7}$
$a_3$	$2.71086763 \cdot 10^{-7}$
$a_4$	$2.36380371 \cdot 10^{-9}$
$a_5$	$3.64198016 \cdot 10^{-8}$
$a_6$	$-8.93969951 \cdot 10^{-12}$
$a_7$	$7.22075351 \cdot 10^{-11}$

The uncertainties on the angles derived from the polynomial interpolation were determined from the error matrix of the least squares fit procedure. They are presented as a function of the crystal angle in Fig. 10 (curve B). However, it has to be mentioned that as a result of vibrations, successive readings of the interferometer for the same angular position of the crystal provide values that are fluctuating up to  $\pm 15$  optical units. To diminish these fluctuations, the interferometer is usually read several times during the data collection at a given crystal angle and the average value is taken. Typical standard deviations for three, five and ten interferometer readings are  $\sim 7$ ,  $\sim 5$  and  $\sim 3$  optical units, respectively. If these

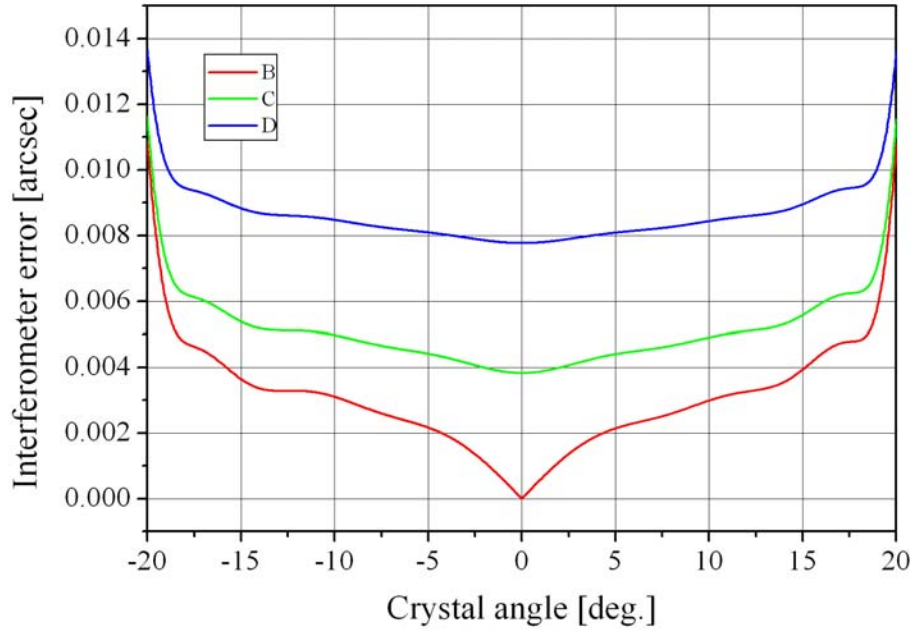


FIGURE 10: Interferometer errors in arcsec as a function of the crystal angle. The red curve B gives the error originating from the sole interferometer calibration, the green curve C and the blue curve D consider in addition the standard deviations for 10 and 3 interferometer readings, respectively.

fluctuations are taken into consideration, the uncertainties on the angles are somewhat larger as shown in Fig. 10 where the total interferometer errors corresponding to ten (curve C) and three readings (curve D) are also given.

### 3.1.5 Collimator and collimator rotation mechanism

As mentioned in Sect. 3.1.1, in the DuMond geometry a Soller slit collimator is installed in front of the spectrometer detector. It serves mainly to suppress the direct photon beam which is spatially overlapping with the diffracted beam at small Bragg angles. For the DuMond spectrometer of Fribourg, the two beams are overlapping for Bragg angles  $\theta_B \leq \sim 1.0$  deg. In addition the collimator diminishes by a factor of about 65 the background originating from the elastic and inelastic scattering by the crystal of the incoming photon beam.

The collimator consists of 24 parallel rectangular slits which are 660 mm long, 110 mm high and 2 mm wide. The horizontal axes of symmetry of the 24 slits converge all to

the same point. The latter which is located on the focal circle represents the virtual source of radiation. If one considers a vertical plane mirror containing the diameter passing through the crystal center and the crystal curvature center, this virtual source corresponds then to the mirror image of the real source. The collimator was constructed by inserting 23 stainless steel plates in a hollow prismatic frame made of cast iron. The vertical side walls of the frame are rectangular (660 mm long  $\times$  105 mm high  $\times$  20 mm thick) whereas the horizontal bottom and top walls are trapezoidal with the same length and thickness as the side walls but a width of 134 mm on the rear side and of 123.95 mm on the front side. The 23 rectangular plates have the same length and height as the vertical walls of the frame but a thickness varying linearly from 2.00 mm on the rear side to 1.56 mm on the front side. The plates are arranged so that the space between two neighboring plates is exactly 2 mm and the longitudinal axes of the plates converge all to the same point, the above defined virtual source of radiation. With this design, the transmission of the collimator amounts to 51%.

The response function of the collimator measured at a Bragg angle equal to zero is shown in Fig. 11 where the intensity of the direct photon beam is plotted as a function of the collimator angular position. The curve has a nearly–trapezoidal shape. The width of the plateau is about 200 arcsec and the one of the two flanks 1100 arcsec, in more or less satisfactory agreement with the calculations which predict widths of 140 and 1040 arcsec, respectively. The difference between the measured and theoretical plateau widths and the small curvature observed on the two flanks (which should correspond to straight lines according to geometrical considerations) result probably from the high count rate characterizing this measurement and the non–considered dead time of the detection system. Similar transmission curves can be obtained by setting the crystal on the Bragg angles corresponding to the centroids of diffracted x–ray lines. In this case, the collimator response function indicates the intensity transmitted by the collimator as a function of its misalignment, i.e., as a function of its angular deviation from  $2\theta_B$ .

The collimator rotation mechanism is depicted in Fig. 4. A self–propelled carriage supports the collimator, the detector and the heavy lead shielding of the latter. The carriage can move independently on a circular rail made of hardened stainless steel. The radius of the circular rail is 2750 mm and its total length 4743 mm. This length is

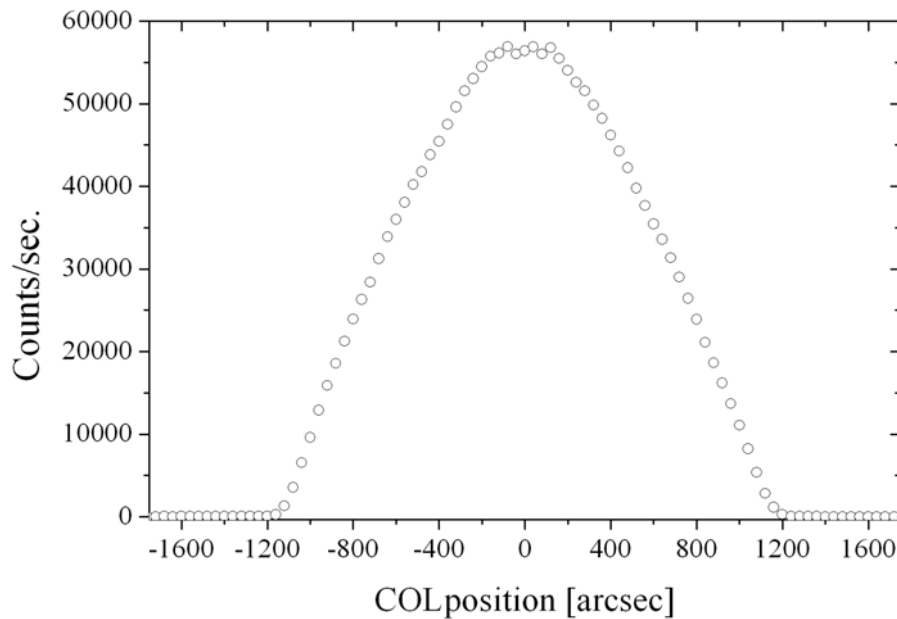


FIGURE 11: Transmission curve of the Soller slit collimator measured at a Bragg angle equal to zero. The photoinduced fluorescence x-ray emission of a gadolinium target was employed as incoming photon beam.

necessary to cover the range of  $\pm 40$  deg. of the collimator–detector system. The carriage is equipped with two conical rollers. One of them is driven by a high–power step motor. One step of this motor corresponds to a rotation of the collimator–detector system by about 1 arcsec. The shape of the conical rollers and the angle between their axes were designed to match perfectly the radius of the circular rail. Furthermore, since the rotation axis of the collimator does not generally coincide with the center of curvature of the circular rail, the mechanical connexion between the table supporting the collimator–detector system and the carriage involves a two–stage bearing which takes care of the appropriate matching between the two different movements.

During the acquisition of an x–ray spectrum the collimator has to be kept aligned on the double Bragg angle  $2\theta_B$  with a precision better than the half of the angular width of the collimator plateau. For the DuMond spectrometer of Fribourg, the condition  $\theta_{col} = 2\theta_B$  is automatically satisfied thanks to an optical tracking device consisting of a laser located on the collimator arm, a mirror placed on the crystal axis and a two–segment photodiode whose position is fix. The error signal provided by the photodiode, which is proportional to the deviation of the laser beam spot from the photodiode center, serves to control the



step motor of the collimator carriage. When the crystal and the mirror placed on the axis of the latter start to rotate, the laser beam spot moves on the photodiode and the resulting error signal which commands the movement of the motor of the collimator carriage forces the latter to follow the rotation of the crystal. As the laser beam reflected by the mirror rotates two times more than the mirror, the detector–collimator system is automatically aligned with the direction corresponding to the double Bragg angle. The accuracy of this optical feedback system was probed over the entire angular range of the detector ( $\pm 40$  deg.) and found to be better than about 25% of the collimator plateau width.

### *3.1.6 Detectors*

For the detection of the diffracted x–rays a Phoswich scintillation counter [22] with a 0.001 inch thick aluminum entrance window is usually employed. This 5 inches in diameter detector consists of a front 0.25 inch thick NaI(Tl) crystal followed by an optically coupled 2 inch thick rear CsI(Tl) crystal. Both scintillation crystals are mounted on the same photomultiplier tube. The first crystal serves to detect the radiation of interest, whereas the second crystal acts as an active shielding permitting to reject events corresponding to background and higher diffraction order photons. Thanks to the different decay times characterizing the two crystals, the fluorescence signals corresponding to the two scintillators can indeed be distinguished and separated by a dedicated hardware using a pulse shape analysis module. Three classes of events are recognized by the electronics: events corresponding to a single signal from the NaI(Tl) crystal, to a single signal from the CsI(Tl) crystal or to simultaneous signals from both scintillators. Events belonging to the second class are mainly due to cosmic rays, those belonging to the third one to high–energy photons that have done a Compton interaction in the first crystal and a Compton or photoeffect in the second one. All such events are rejected by the detection system. Good events are those belonging to the first class since they correspond to lower energy photons entering the detector from the proper side and with the right direction, i.e., the direction defined by the collimator angle  $2\theta_B$ . Note that the thickness of 0.25 inch of the front NaI(Tl) detector is large enough to almost fully absorb the characteristic x–ray emission of any element throughout the Periodic Table. For instance, the absorption of 100 keV

photons amounts to 98%.

The two crystals and the photomultiplier tube, wrapped in  $\mu$ -metal (nickel-iron alloy), are contained in a hermetically sealed 0.25 inch thick stainless steel housing. In addition, in order to reduce the background the detector is placed in a thick Pb-Cu-Al shielding. The relative energy resolution of the Phoswich detector varies as a function of the photon energy between 20% and 30%. During the acquisition, good events are sorted by setting an appropriate energy window in the ADC spectrum of the detector, which permits to further reduce the background of the measured Bragg spectrum. With the x-ray tube switched off, the background level was found to be nearly energy independent, except below 15 keV where some increase is observed. At 17.479 keV (the energy of the  $K\alpha_1$  x-ray line of Mo), a value of 0.033 counts/sec. was for instance observed.

For certain applications for which a better energy resolution is needed for the detection of the diffracted photons, the Phoswich scintillator can be replaced by a semiconductor detector. Two such semiconductor detectors are available. They were specifically designed for an easy installation behind the collimator with, in particular, the detector nose sitting on the top of the LN<sub>2</sub> dewar. The first one is a 20 cm<sup>3</sup> intrinsic germanium LeGe detector having a thickness of 10 mm. The second one is a 0.4 cm<sup>3</sup> lithium-doped silicon Si(Li) detector having a thickness of 5 mm. Thanks to its big surface (20 cm<sup>2</sup>), which permits to cover about 85% of the diffracted photon beam, and its sizeable thickness (1 cm) the 1<sup>st</sup> detector can be used advantageously for measurements that need a good detection efficiency at sizeable photon energies together with a high enough spectrometer luminosity. The second one, which has a surface smaller than 1 cm<sup>2</sup> is mainly employed when the diffracted photon beam is intense and its energy is below about 20 keV. Note that the energy resolution of the Si(Li) detector is about 180 eV (i.e. about 30 times better than the resolution of the Phoswich detector) and its small area leads also to an increased resolution of the crystal spectrometer since only a small part of about 0.5 cm<sup>2</sup> of the crystal reflecting area is employed in this case for the diffraction of the photons. The combination of these two advantages makes this small detector also very useful for dedicated x-ray metrology applications.

### *3.1.7 Driving and acquisition electronics*

The schematic block diagram of the electronics for driving the spectrometer and acquiring data is shown in Fig. 12. The steering of the motors of the spectrometer and the target chamber is controlled by a Z80 microprocessor (MPMZ80) via VME micro-step generators and linear amplifiers. Each motor has its own micro-step generator and linear amplifier. This driving electronics was developed and constructed by the electronics pool of the Physics Department. The communication between the PC and the VME modules is performed through a RS-232 connection at a baud rate of 9600 bytes per second. The controller of the HP interferometer is also connected to the Z80 microprocessor through a GPIB interface.

The main function of the acquisition electronics is to amplify, shape and sort the signals provided by the Phoswich detector. The Phoswich photomultiplier yields two output signals: the first one is used to determine the total energy deposited in the detector (energy signal) and the second one, which is faster, is used for timing purposes (timing signal). The energy signal is sent to the input of a spectroscopy amplifier (SA) whose gain can be chosen and the shaping time is kept fixed at 1  $\mu$ s. The timing signal is sent through a timing filter amplifier (TFA) to the pulse shape discriminator (PSD). The latter permits to separate the x-ray photons that loose their energy entirely in the main crystal from those that loose their energy, partly or totally, in the second crystal. The separation of the two signals is possible because of their different rise time. The PSD module provides a gate signal if the timing signal corresponds to a good event and an anti-gate signal in the opposite case. The gate or anti-gate signal and the signal from the spectroscopy amplifier are both sent to a linear gate. If the gate signal is present, the linear gate forwards the energy signal to a multifunction data acquisition card (DAQ) which is mounted in the computer itself. If it is an anti-gate signal, the energy signal is ignored by the linear gate. The DAQ card converts the analog energy signal into a digital one, which can be then handled with the appropriate software.

The computer is equipped with a PCI-6040 E series Multifunctional I/O card made by National Instruments [23]. This card consists of an analog to digital converter (ADC) with 8 input channels for voltage measurements, a digital to analog converter (DAC) with 2

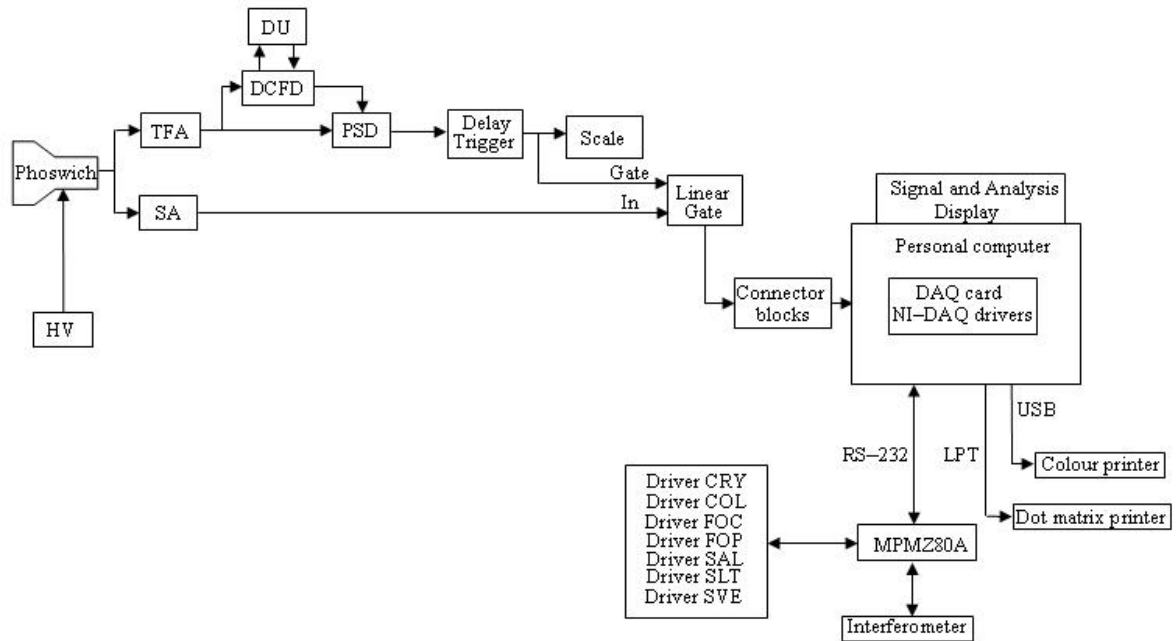


FIGURE 12: Block diagram of the driving and acquisition electronics of the spectrometer. HV stands for the high-voltage power supply of the Phoswich detector (1280 V), SA for the Spectroscopy Amplifier (Canberra, model 2021), TFA for the Timing Filter Amplifier (Ortec, model 454), DCFD for the Differential Constant Fraction Discriminator (Canberra, model 2129), DU for Delay Unit (home made module) and PSD for the Pulse Shape Discriminator (Canberra, model 2160A).

output channels for generating voltages, several counters and digital input/output (I/O) ports. The precision of the conversion of the analog input signal into a digital signal depends on the number of bits used by the ADC. The DAQ card which is installed in our computer has a resolution of 12 bits (4096 channels), a 250 kB/s multichannel sampling rate and a dynamical range of 0 to 10 V.

## 3.2 LabVIEW software

### 3.2.1 General description

The data acquisition and the spectrometer operation are controlled by a self-written program using the LabVIEW 8.0 software (shortcut from Laboratory Virtual Instrumentation Engineering Workbench) developed by National Instruments. LabVIEW is one of the most popular and powerful available tools for the acquisition, analysis and data display as well as for external instrument operation [24]. An important advantage of the LabVIEW software is the availability of many libraries with a large number of functions for data acquisition, data analysis, mathematics, statistics and data presentation as well as an extended database of drivers for DAQ cards and instrument communication. The new program for the data acquisition and driving of the spectrometer makes a large use of these libraries. LabVIEW is a graphical programming language  $G$  that uses icons instead of command lines for the creation of applications. LabVIEW programs are called virtual instruments, or VI's, because their appearance and way of operation imitate physical instruments, such as oscilloscopes and multimeters.

Each LabVIEW program consists of two windows: the Front Panel which serves as user interface and the Block Diagram where the real programming flow takes place (Fig. 13). The Front Panel consists of Controls and Indicators, which correspond to the interactive input and output terminals of the VI's, respectively. Controls are knobs, push buttons, dials, and other input devices. Indicators are graphs, LED's, and other displays. Controls simulate instrumental input devices and supply data to the Block Diagram of the VI's. Indicators simulate instrument output devices and displays, acquire or generate data of the Block Diagram. Objects for the Front Panel are taken from the Controls Palette. The user can enter data by using the mouse or keyboard and then view the results produced by the program on the screen.

The Block Diagram consists of Terminals, Functions and Wires. The objects for the Block Diagram are taken from the Functions Palette. When Controls or Indicators are set on the Front Panel, the objects corresponding to them automatically appear as Terminals in the Block Diagram. Terminals are entry and exit ports that exchange information between the Front Panel and the Block Diagram. The Terminals represent the

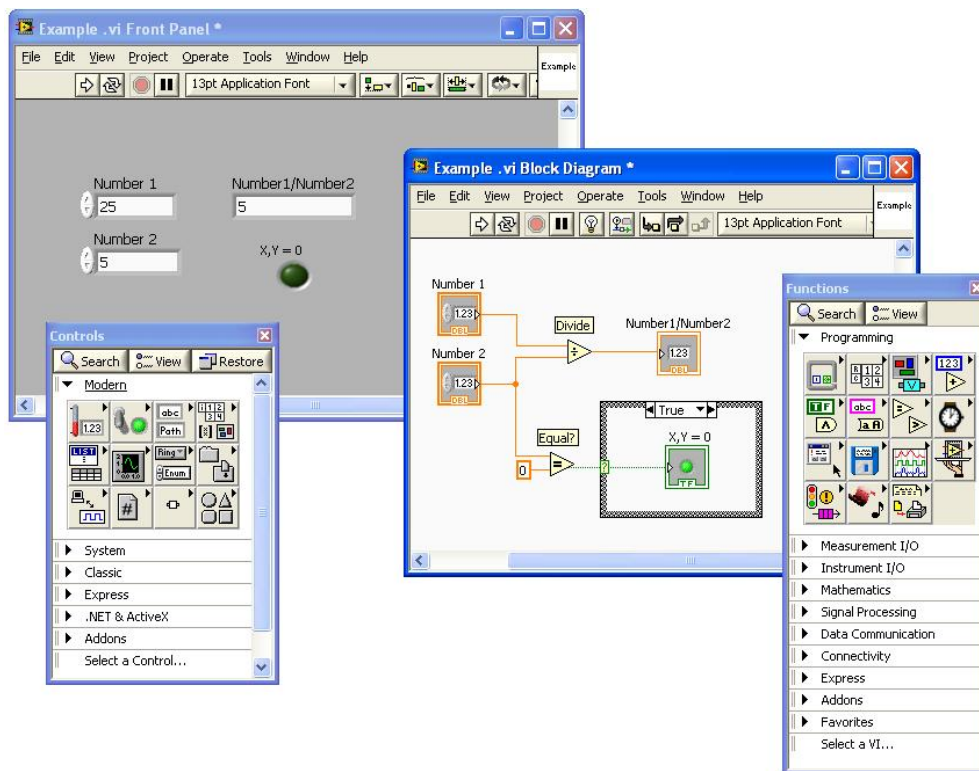


FIGURE 13: Example of a simple program written in the LabVIEW language.

data type of the Controls or Indicators. The data are transferred between the Block Diagram objects through the Wires. Each Wire has a single data source, but the latter can be wired to many VI's and Functions that read the data. Wires have different colors, styles, and thicknesses depending on the type of data they transfer.

The Structures are graphical representations of the Loops. They are used in the Block Diagram to repeat blocks of code. The Structures have Terminals that connect them to the other Block Diagrams. The section of the Block Diagram inside the Structure Border is called a Subdiagram. The Terminals that feed data into Structures and out from them are called Tunnels. To Structures belong the:

- *FOR loop* – executes a Subdiagram for a preset number of times.
- *WHILE loop* – executes a Subdiagram until a particular condition occurs.
- *CASE Structure* – contains multiple Subdiagrams, but executes only one of them depending on the value transferred to the Structure.

- *SEQUENCE Structure* – contains one or more Subdiagrams that are executed in a sequential order.
- *TIMED Structure* – executes one or more Subdiagrams with time boundary conditions or delays.
- *EVENT Structure* – contains one or more Subdiagrams that are executed depending on the way the user interacts with the VI's.

In LabVIEW the Functions are the basic operating elements for the creation of a program. They do not have Front Panels or Block Diagrams but Connector Panels. They cannot be opened or edited. In order to use in a LabVIEW program a particular Function, the latter should be taken from the Functions Palette and then inserted into the diagram. Different kinds of Functions exist. In general, they can be divided into two categories: the Functions which are used to manipulate data and those which are used to dialog with the instrument, collect data or send the latter from the computer to external devices.

### 3.2.2 Serial Port Communication

As mentioned before the steering of the spectrometer is controlled by a MPMZ80 processor. The communication with this microprocessor is performed through a RS-232 serial port. The serial communication is popular because most computers have one or more serial ports. Therefore no additional hardware is needed, except a cable, to connect the instrument to the computer. Another advantage of serial communication is the ability of the latter to control an instrument at large distances. In the serial communication the serial port sends and receives the information bytes sequentially. Several parameters must be specified for the serial port configuration (Fig. 14): the *baud rate* which indicates how fast the data are transmitted through the port, *data bits* which specifies the number of bits of the exchanged data, *parity* which specifies the parity used for every byte frame to be sent or received, stop bits which gives the number of stop bits used to indicate the end of a frame and flow control which sets the type of control used in the transfer mechanism.

In order to communicate via serial ports, the VI's and Functions located in the Function-Instrument I/O-Serial Palette (Fig. 15) are employed. This Subpalette consists

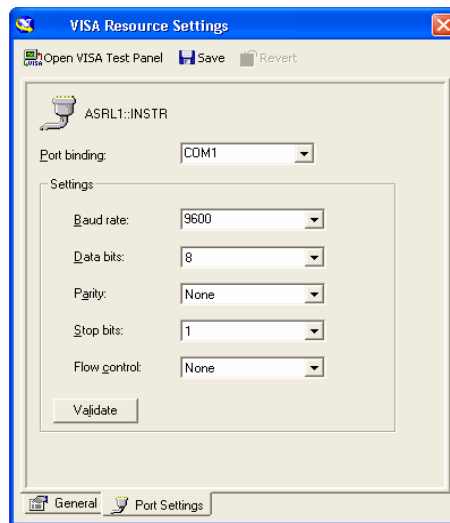


FIGURE 14: Serial port parameters.

of VI's needed to initialize the serial port, send data to it, read data from it, return the number of bytes, set a serial port break, set the I/O buffer size and flush the I/O buffer. The most important functions needed for serial port communication and used in our program are presented below.

- *VISA Configure Serial port* (Fig. 16a) – initializes the port identified by the VISA resource name to the specified settings.
- *VISA Write* (Fig. 16b) – writes the data from the Write Buffer into the device specified by the VISA resource name.
- *VISA Read* (Fig. 16c) – reads the specified number of bytes from the device specified by the VISA resource name and returns the data in the Read Buffer.
- *VISA Close* (Fig. 16d) – closes a device session.

The VISA–Virtual Instrument Software Architecture is the standard Application Programming interface for instrument I/O communication. VISA is not LabVIEW specific, but is a standard available in many programming languages [25]. The same VI's and Functions which are used for communication with serial port are also used for parallel port communication. In this case the VISA resource name must be specified as being one of the LPT ports. In our case the communication with the dot matrix printer is performed through a LPT port.



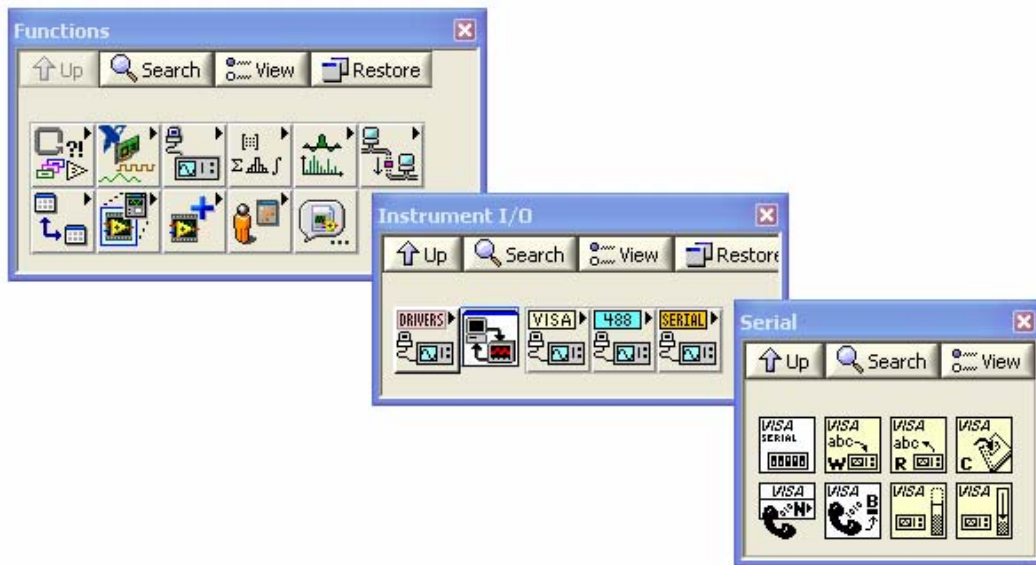


FIGURE 15: Serial Functions Palette

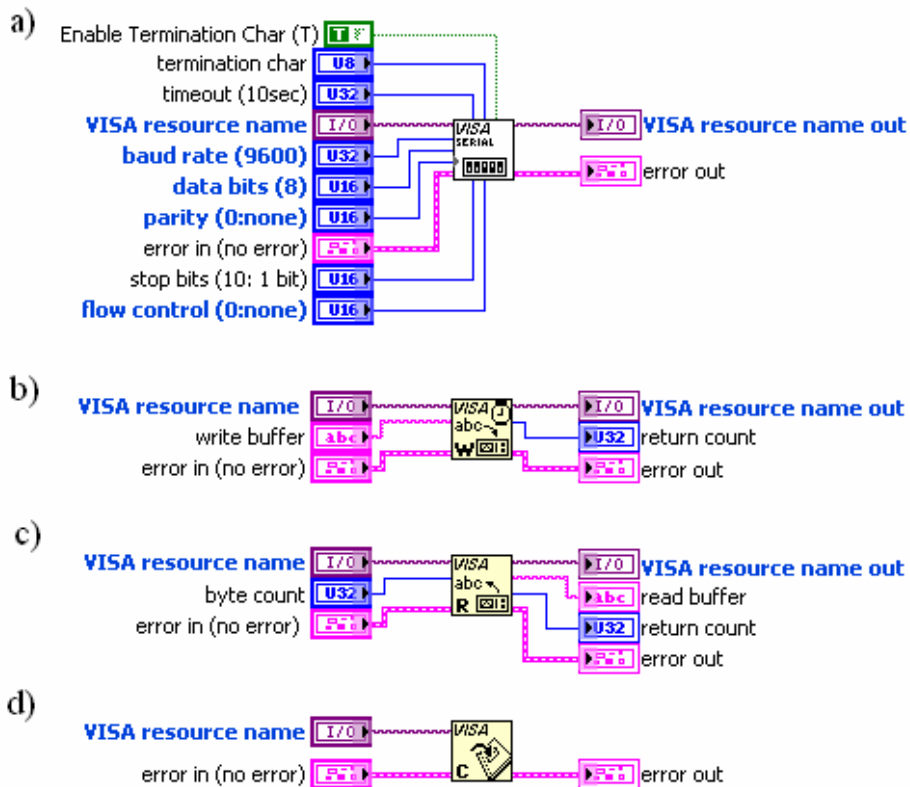


FIGURE 16: The VISA functions occurring in the program used to communicate with the spectrometer.

### 3.2.3 Communication with the DAQ card

As mentioned before the signal from the detector is sent to the data acquisition card which is installed directly inside the computer. The LabVIEW includes a set of ready-made VI's and Functions which are used to configure this DAQ card, acquire data from it and send data to it. These VI's and Functions are located in the Function-Measurement I/O-DAQmx Data Acquisition palette (Fig. 17).

Getting data from a data acquisition device is very simple. But, before acquiring data, one must configure the DAQ card using a second software package from National Instruments called *Measurement & Automation Explorer* (or MAX). Measurement & Automation Explorer is a software interface that gives access to all National Instruments devices connected to the system. The shortcut to MAX is placed on the desktop during the installation of the NI-DAQ. When the application using the NI-DAQmx is run the software reads the MAX configuration to determine which device was configured. To acquire data, the following pieces of information are needed by the software: *device number*, *task/channel* that is being used, *acquisition mode* which specifies if the task should acquire or generate data continuously, i.e., as long as the DAQmx Stop Task VI

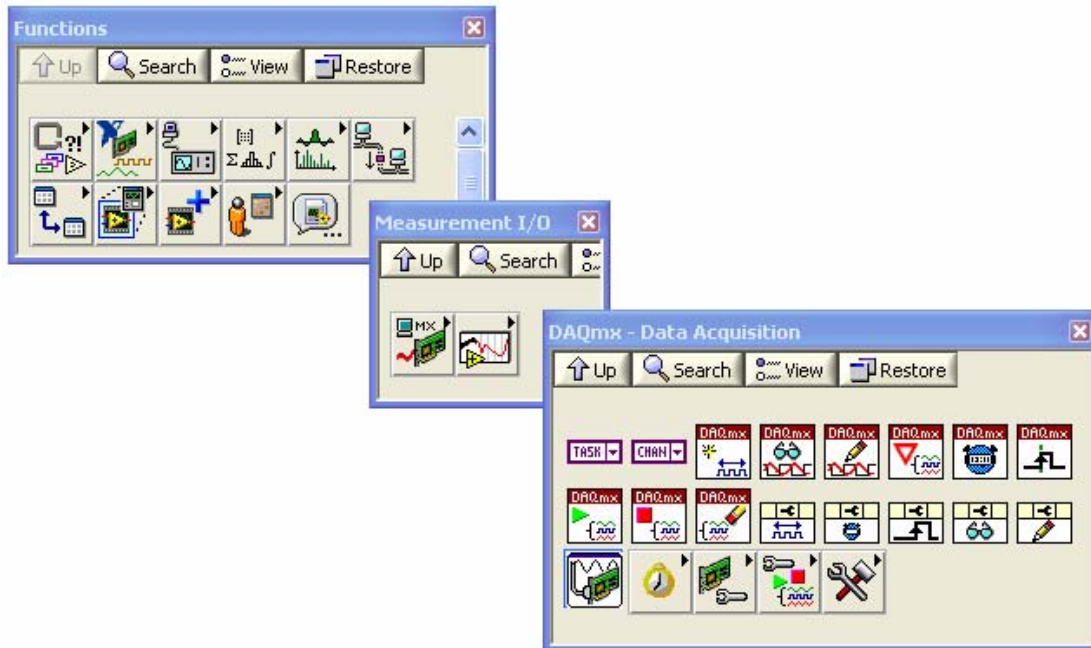


FIGURE 17: NI-DAQmx – Data acquisition palette.

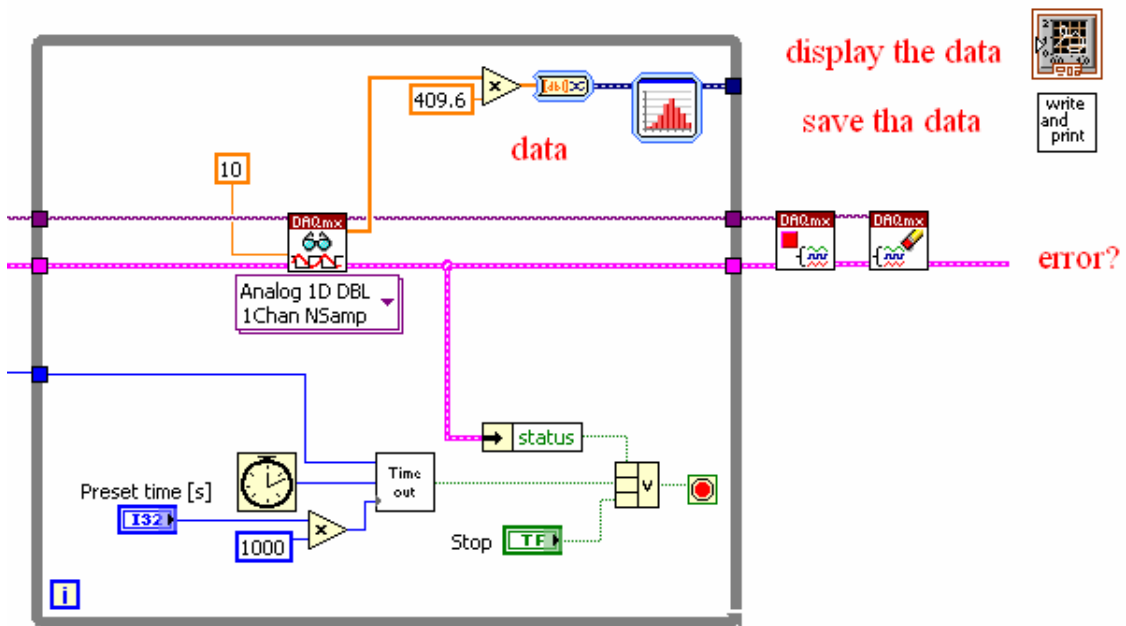
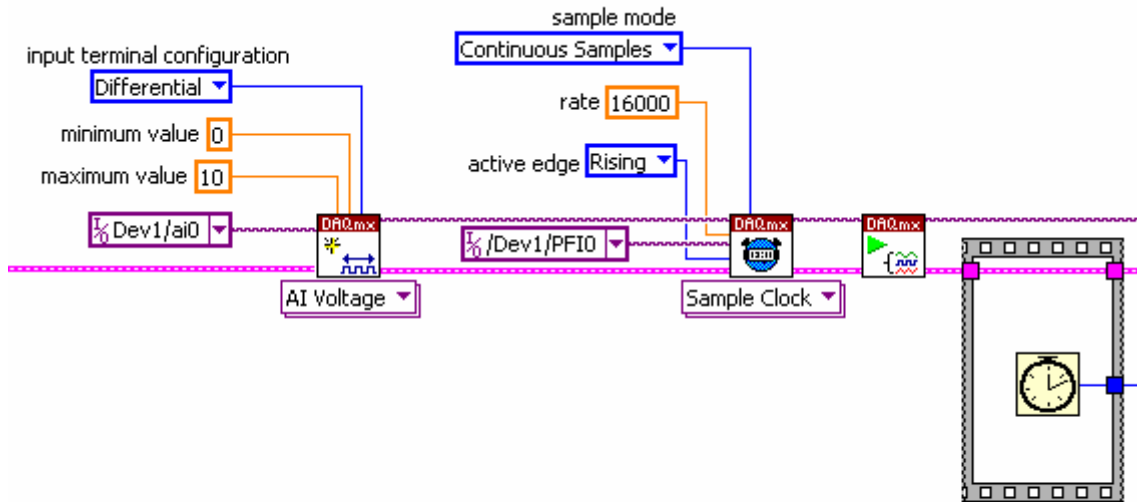


FIGURE 18: Block Diagram showing the program for data acquisition.

runs or if the task should acquire or generate a preset number of data and *sampling rate* which determines at which speed the device should acquire or generate data in each channel. A faster sampling rate results in acquiring more data in a given time.

For illustration, the block diagram corresponding to the part of the program which is used for data acquisition is presented in Fig. 18. At first, the task corresponding to the measurement of the detector signal voltage is created. For that, the input channel of the DAQ card and the minimum and maximum voltages have to be selected. In our case, the signal is read from the analog input channel, ai0, and the voltage ranges between 0 and 10 volt. The DAQ card uses a sample clock to control the rate at which samples are acquired. This sample clock sets the time interval between samples. Each tick of this clock initiates the acquisition of one sample per channel. Here the rate of the clock was chosen to be 16'000. *Continuous samples* was chosen for the sample mode and *rising* for the active edge. The active edge specifies on which edge of the sample clock pulses controls the acquisition. After that the acquisition is started. The single floating-point sample is read from the selected channel of the DAQ card. The *timeout* was set to 10 seconds, so that an error is returned if the samples are not returned after this time. The data are read until the preset collecting time is finished or the stop button selected or an error occurs. In each case, the acquisition is stopped and the specified task is cleared.

### 3.3 Data acquisition

The front panel and the simplified flow chart of the acquisition program for measuring an angular spectrum are shown in Fig. 19 and Fig. 20, respectively.

Before starting the measurement of the given x-ray line or x-ray spectrum, all motors of the spectrometer and target chamber must have been initialized and the interferometer reset. To start the acquisition the user has to define first the different parameters of the measurement. The main input parameters are the crystal start position and the focal distance of the crystal which is calculated from Eq. (9b). In the measurement performed with the DuMond spectrometer the x-ray spectra are measured point-by-point. Therefore, the step length and the number of steps needed to cover the whole angular range corresponding to the given x-ray line or x-ray spectrum are also needed. The acquisition time per point which is chosen depending on the count rate, the energy window which allows to reject higher reflection orders and background events and the number of interferometer readings per point must also be entered. Finally the file name and the directory where the data will be stored in the computer have to be chosen.

If the energy  $E$  of the line to be measured in the  $n^{\text{th}}$  reflection order is known, the Bragg angle  $\theta$  can be determined from Eqs. (1) and (2):

$$\theta = A \sin \left( \frac{12.398419 [\text{keV} \cdot \text{\AA}]}{2d_{hkl} [\text{\AA}]} \cdot \frac{n}{E [\text{keV}]} \right). \quad (11)$$

The mechanical crystal position of the x-ray line measured on the right side ( $n > 0$ ) or the negative side ( $n < 0$ ) of reflection and corresponding to the Bragg angle  $\theta$  can then be determined by using the following formulas:

$$CRY_{(n>0)}[\text{step}] = ZMPC[\text{step}] + \theta[\text{step}], \quad (12a)$$

$$CRY_{(n<0)}[\text{step}] = ZMPC[\text{step}] - \theta[\text{step}], \quad (12b)$$

where  $ZMPC$  is the “mechanical zero position” of the crystal given in motor steps and one motor step corresponds to 1 deg./48'000.

When all parameters have been entered and the tracking mode has been switched on for the collimator motor, the program can be started. First, the step motor sets the crystal

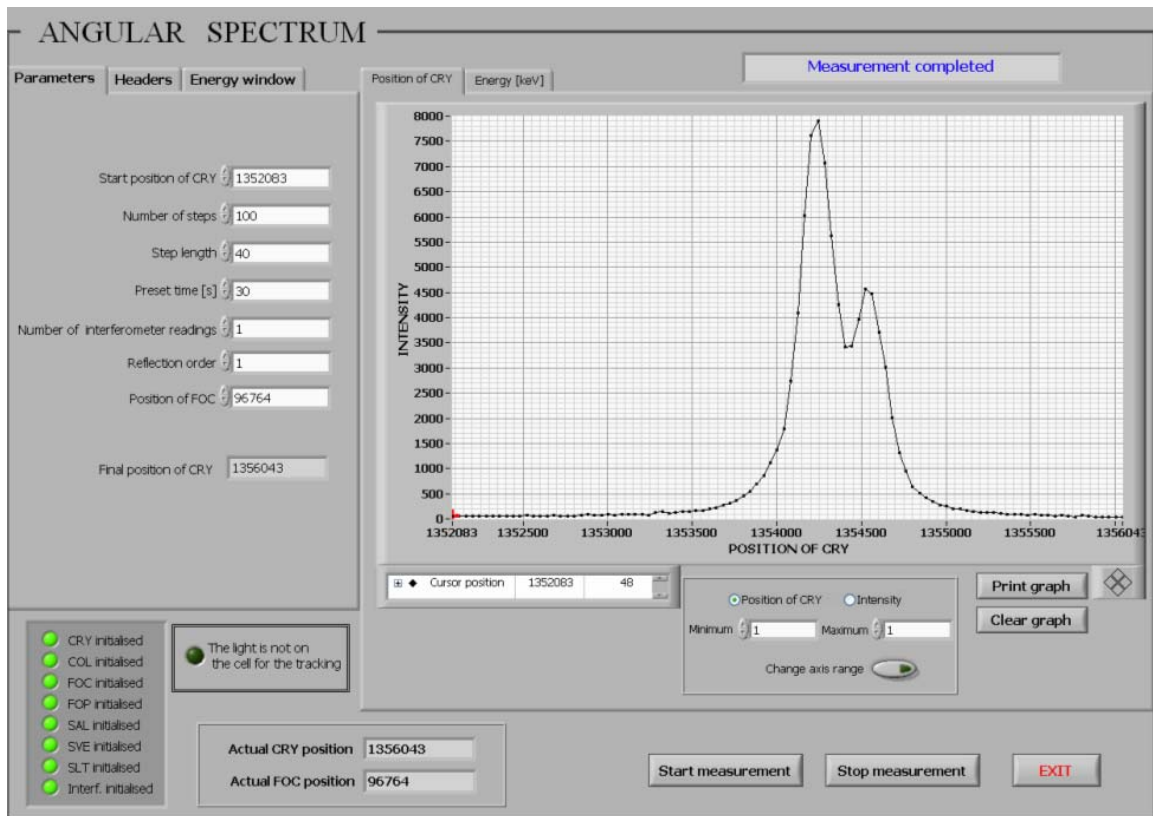


FIGURE 19: Front Panel of the acquisition program for measuring an angular spectrum. Here, the indicated parameters correspond to the measurement of the Mo  $K\beta$  x-ray spectrum in 1<sup>st</sup> order of reflection (right side).

at the angle corresponding to the given crystal start position. Depending on the side of reflection at which the measurement is performed, this start position corresponds to the minimum (left side) or maximum (right side) x-ray energy of the spectrum. When the crystal motor indicates that it has reached the start position, data are collected during the chosen acquisition time. Then, the crystal is moved to the next position, rotating the crystal by the number of steps corresponding to the selected step length. When this second angular position is reached, the data acquisition starts again. This process is repeated until the crystal reaches its final position. At each point, the computer reads several times the laser interferometer and the mean value is determined. The mean value of the interferometer corresponding to each measured point will be used later on for the energy calibration of the spectrum. For each measured point the most important parameters like the mechanical crystal position, mean value of the interferometer, effective acquisition

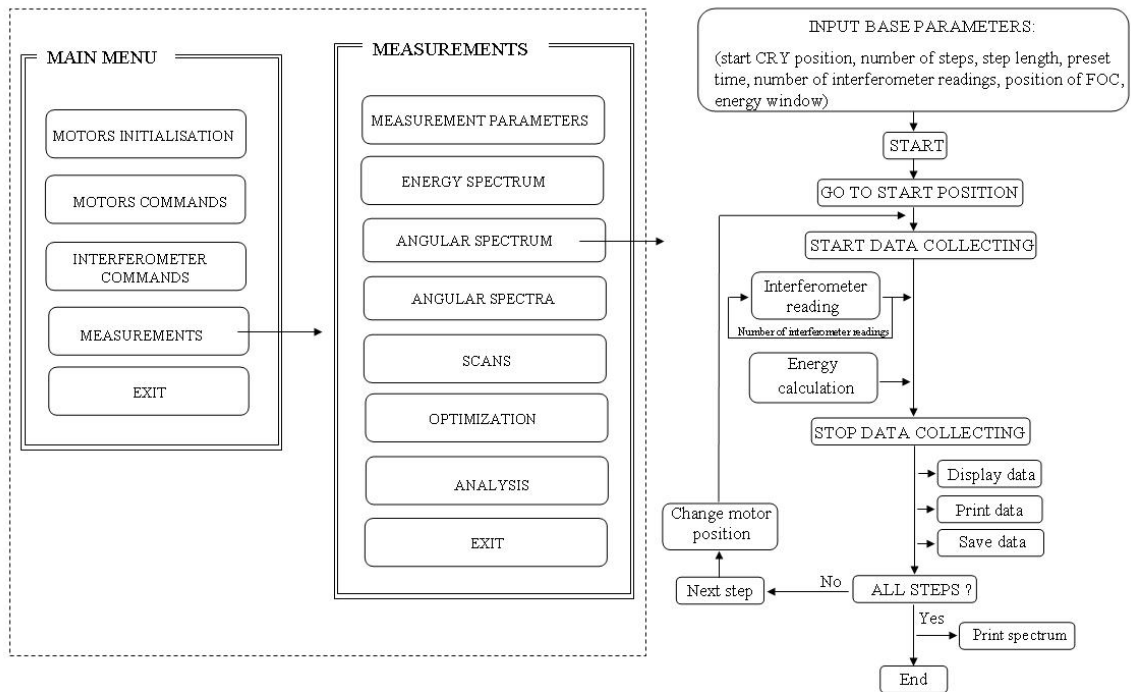


FIGURE 20: Flow chart of the acquisition program for measuring an angular spectrum.

time, count number and energy are saved by the computer in the appropriate file and simultaneously printed by the LTP printer for the on-line survey of the measurement. The angular Bragg spectrum is built point by point and displayed graphically on the screen. The data can be presented as a function of the energy [keV] or as a function of the crystal position [motor steps].

### 3.5 Data analysis

For a precise determination of energies with a crystal spectrometer an accurate energy calibration of the instrument is required. For the energy calibration of the angular spectra observed with the DuMond spectrometer the “spectroscopic zero position”, i.e., the origin of the Bragg angles scale, and the crystal spacing constant of the reflecting planes are needed.

In order to determine the zero Bragg angle an x-ray line must be measured on both sides of reflection. The centroids positions of the two lines are obtained from the fits of the two angular spectra and are therefore given in optical units [OU]. The two centroids positions are then converted in radians using the interpolation polynomial of the interferometer given by the relations (10). Using the calculated values and Eq. (7), the “spectroscopic zero position”  $\theta_0$  is obtained. As mentioned in Sect. 3.1.1, the “spectroscopic zero position” is not constant and varies with the employed crystal and position of the slit. It varies also slightly with the focal distance so that a new determination of  $\theta_0$  has to be done whenever the focal distance of the spectrometer is changed.

The lattice spacing constant  $d_{hkl}$  of the crystal can be determined similarly by measuring an x-ray line taken as reference on both sides of reflection, provided the energy of this reference line is known with a good enough accuracy. The difference of the two fitted centroids positions give indeed an angle equal to  $2\theta_B$ . Using the Bragg law, one can then write:

$$d_{hkl} [\text{\AA}] = \frac{12.398419 [\text{keV} \cdot \text{\AA}]}{2 \sin\left(\frac{\theta_+ - \theta_-}{2}\right)} \cdot \frac{n}{E [\text{keV}]}, \quad (13)$$

where  $n$  is the diffraction order and  $\theta_+$  and  $\theta_-$  the centroid positions of the reference line measured on the right and left sides of reflection, respectively. From the Bragg law the following expression is easily obtained for the error  $\Delta d_{hkl}$ :

$$\Delta d_{hkl} = \sqrt{(\text{ctg} \theta)^2 \Delta \theta^2 + \left(\frac{\Delta E}{E}\right)^2} d_{hkl}, \quad (14)$$



where  $\Delta E$  stands for the uncertainty on the energy of the x-ray transition taken as reference. Furthermore,  $\Delta\theta$  is given by:

$$\theta = \frac{\theta_+ - \theta_-}{2}, \quad \Rightarrow \quad \Delta\theta = \frac{1}{2} \sqrt{(\Delta\theta_+^{fit})^2 + (\Delta\theta_+^{int})^2 + (\Delta\theta_-^{fit})^2 + (\Delta\theta_-^{int})^2}, \quad (15)$$

where  $\Delta\theta^{fit}$  and  $\Delta\theta^{int}$  represent the errors originating from the fit and the angular interferometer, respectively.

In all measurements presented in this work, the (110) diffraction planes of a quartz crystal were employed. The spacing constant  $d_{110}$  was determined by means of the above method, using the  $K\alpha_1$  x-ray line of Gadolinium as reference. A 36 mg/cm<sup>2</sup> thick metallic Gd foil was employed. The latter was tilted to make an angle of 6.75 deg. with respect to the target-crystal direction because at this angle the maximum count rate was observed. For the photoionization a gold anode x-ray tube operated at 80 kV and 30 mA was used. The tube was oriented so that the axis of the conical beam emitted by the tube was perpendicular to the target-crystal direction. The distance between the x-ray tube anode and the target was 45 mm. In order to increase the precision on the  $d_{110}$  constant, the Gd  $K\alpha_1$  x-ray line was measured on both sides of reflection in first, second, third, fourth and fifth diffraction orders. For each diffraction order, the  $d_{110}$  constant and its uncertainty were determined from the relations (13) and (14), using for the energy of the Gd  $K\alpha_1$  transition the value of 42996.72(44) eV quoted in [26]. From the five series of measurements the following average value was found:

$$d_{110} = 2.456549 \pm 0.000011 \text{ \AA} \quad (16)$$

Note that the relative uncertainty of about 4.5 ppm originates mainly from the uncertainty on the energy of the reference line.

When the spacing constant of the diffraction planes  $d_{hkl}$  and the zero Bragg angle  $\theta_0$  have been determined, any point  $i$  of a Bragg spectrum measured with the same focal distance as the reference line can be calibrated in energy, using the following relation:

$$E_i[\text{keV}] = \frac{12.398419[\text{keV} \cdot \text{\AA}]}{d_{110}[\text{\AA}]} \cdot \frac{n}{2 \sin(\theta_i - \theta_0)} = 5.047088[\text{keV}] \cdot \frac{n}{2 \sin(\theta_i - \theta_0)}. \quad (17)$$

Finally, the x-ray spectrum, calibrated in energy, can be analyzed by means of a least-

squares–fitting method which is employed by different analysis programs. In our case, the PeakFit software package [27] was used. Voigt functions were chosen to fit the measured x–ray lines. This choice was dictated by the fact that the Voigt function corresponds to the convolution of the Lorentzian natural line shape of an x–ray transition with the Gaussian instrumental response of the spectrometer. The Voigt function can be defined as follows:

$$V(x) = \frac{A_0 \cdot A_3}{2\pi\sqrt{\pi} \cdot A_2^2} \int_{-\infty}^{+\infty} \frac{\exp(-t^2)}{\frac{A_3^2}{2 \cdot A_2^2} + \left(\frac{x - A_1}{\sqrt{2} \cdot A_2} - t\right)^2} dt, \quad (18)$$

where  $A_2$  and  $A_3$  represent the Gaussian and Lorentzian widths, respectively,  $A_0$  the area under the curve and  $A_1$  the peak centroid.

## 4. Examples of measurements

In order to check the performances of the spectrometer with the new acquisition and steering program, a series of test measurements concerning the resolution, precision and sensitivity of the DuMond crystal spectrometer have been performed. Additional measurements illustrating the usefulness of the instrument in different areas of x-ray research are also presented.

### 4.1 Spectrometer resolution

#### 4.1.1 Standard method to determine the instrumental broadening of the spectrometer

The instrumental response of the spectrometer which depends mainly on the slit width, crystal mosaicity and precision of the crystal curvature was found to be well reproduced by a Gaussian function. The angular instrumental broadening was determined using the  $K\alpha_1$  x-ray emission line of a 36 mg/cm<sup>2</sup> thick metallic foil of gadolinium measured in first order of diffraction. The sample was irradiated with the bremsstrahlung produced by a Au anode x-ray tube which was operated at 80 kV and 30 mA. A slit width of 0.10 mm was used. The angular spectrum depicted in Fig. 21 was analyzed with the PeakFit program, using a Voigt function to fit the  $K\alpha_1$  x-ray line. In the fitting procedure the intensity, peak position and Gaussian standard deviation as well as a linear background were let free. The value of the Lorentzian width was taken from the tables of Campbell and Papp [28] and kept fixed in the fitting procedure. As the widths reported in [28] are expressed in eV, the Gd natural width was transformed beforehand in arcsec, using the following expression:

$$\Gamma_{nat,g}[\text{arc sec}] = 2.063 \cdot 10^5 \cdot \text{tg}(\theta_B) \cdot \frac{\Gamma_{nat,E}}{E}, \quad (19)$$

where  $\theta_B$  is the Bragg angle,  $E$  and  $\Gamma_{nat,E}$  the energy and natural width of the transition, respectively. From the analysis of the  $K\alpha_1$  x-ray line, a value of  $\sigma_{instr,g} = 4.82 \pm 0.04$  arcsec was obtained for the standard deviation of the Gaussian function representing the angular instrumental response of the spectrometer. The corresponding full width at half

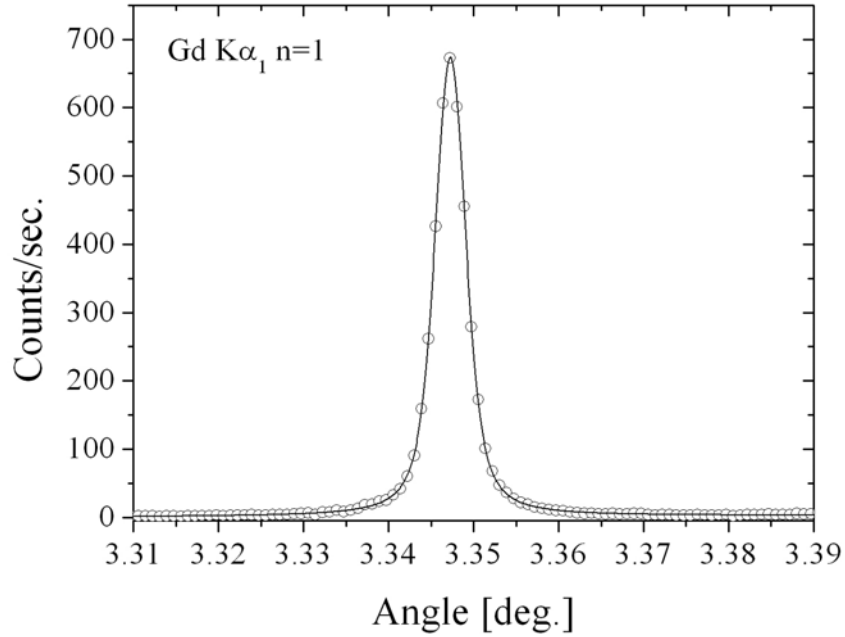


FIGURE 21: The Gd  $K\alpha_1$  x-ray emission line measured in first order of reflection. The solid line corresponds to the total fit of the spectrum.

maximum (FWHM) of the instrumental response is thus  $\Gamma_{instr,g} = 2\sqrt{2\ln 2} \cdot \sigma_{instr,g} = 11.35 \pm 0.09$  arcsec. The energy resolution  $\sigma_{instr,E}$  of the spectrometer can be deduced from the angular resolution  $\sigma_{instr,g}$  via the Bragg law:

$$\Delta E = ctg(\theta_B) \cdot E \cdot \Delta\theta, \quad (20a)$$

$$\Rightarrow \sigma_{instr,E} = ctg(\theta_B) \cdot E \cdot \sigma_{instr,g}, \quad (20b)$$

where  $E$  is the energy and  $\theta_B$  the Bragg angle of the observed x-ray line. Using Eq. (20b) and the above mentioned value of  $4.82 \text{ arcsec} = 2.34 \cdot 10^{-5} \text{ rad}$  for  $\sigma_{instr,g}$ , an energy resolution  $\sigma_E = 17.1 \text{ eV}$  is found for the Gd  $K\alpha_1$  x-ray line whose energy is  $42.996 \text{ keV}$ , whereas for the Mo  $K\alpha_1$  x-ray line which has an energy of  $17.479 \text{ keV}$  an energy resolution of  $2.80 \text{ eV}$  is obtained. This illustrates the fact that for crystal spectrometers the energy resolution becomes poorer with increasing photon energy. Actually, from Eq. (20a), one can show that the energy resolution deteriorates approximately with the squared energy of the measured photons:

$$\Delta E = E \cdot \frac{\cos(\theta_B)}{\sin(\theta_B)} \cdot \Delta\theta = E \cdot \cos(\theta_B) \cdot \frac{2d_{hkl}}{hc} \frac{E}{n} \Delta\theta \approx \frac{2d_{hkl}}{nhc} \Delta\theta \cdot E^2, \Rightarrow$$

$$\Delta E \propto E^2 \text{ for a given } n \text{ and } \Delta\theta. \quad (21)$$

#### 4.1.2 Dependence of the spectrometer resolution on the slit width, focal distance and diffraction order

In the DuMond slit–geometry the effective size of the x–ray source is defined by the slit width. The latter influences the instrumental resolution as well as the measured intensity since the solid angle of the spectrometer is directly proportional to the employed width of the slit. In order to demonstrate the effect of the source size on the instrumental resolution, the Mo  $K\alpha_1$  x–ray emission line was measured with three different slit widths. The measurements were performed with a metallic 54 mg/cm<sup>2</sup> thick foil of Mo irradiated with the bremsstrahlung of a Au x–ray tube operated at 80 kV and 30 mA. The x–ray spectra were acquired in first order of reflection only but on both sides of reflection in order to determine the spectroscopic zero position needed for the energy calibration. Each

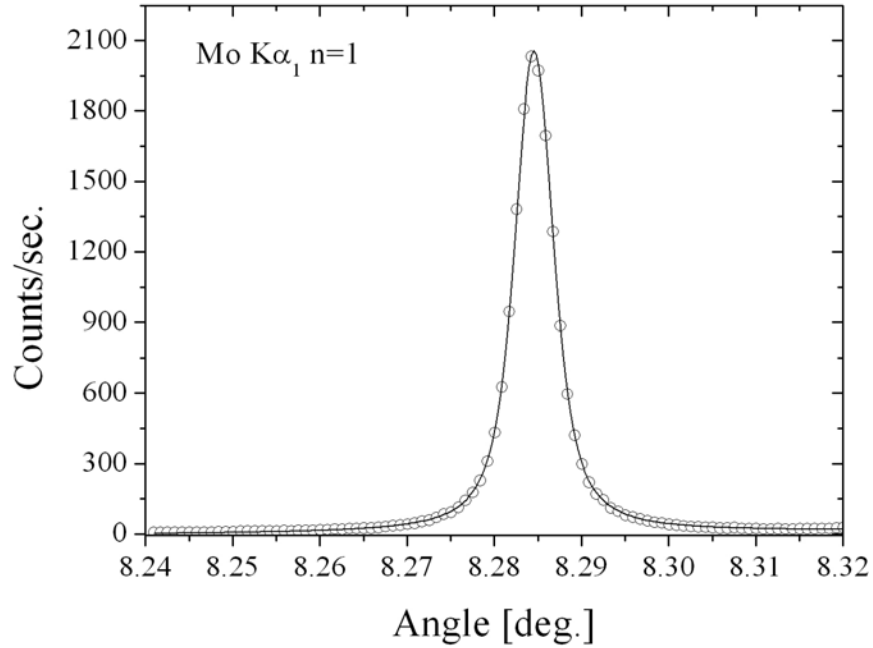


FIGURE 22: The Mo  $K\alpha_1$  x–ray emission line measured in first order of reflection with a slit width of 0.10 mm. The solid line corresponds to the total fit of the spectrum.

TABLE II: Variation of the FWHM instrumental resolution [eV] of the spectrometer as a function of the slit width. The measurements were performed using the  $K\alpha_1$  x-ray line of Mo in 1<sup>st</sup> order of diffraction. The uncertainty on the natural line width is not taken into account in the quoted errors.

Slit width [mm]	0.05	0.10	0.15
FWHM [eV]	$5.64 \pm 0.07$	$6.60 \pm 0.06$	$7.32 \pm 0.04$

spectrum consisted of 100 equidistant points. The data collecting time per point was 30 sec. The energy spectra were fitted using Voigt functions with the intensity, peak position and Gaussian width of the Mo  $K\alpha_1$  x-ray line and the two constants of the linear background as free fitting parameters. The Lorentzian width of the transition was deduced from the tables of Campbell and Papp [28] and kept fixed. The angular spectrum corresponding to the 0.10 mm slit width is shown in Fig. 22. The results provided by the fitting procedure for the energy resolution are presented in Table II. As expected a well-defined linear dependence on the instrumental resolution as a function of the slit width is observed.

Furthermore, in order to probe the effect of the crystal focusing distance on the instrumental resolution, the Gd  $K\alpha_1$  x-ray emission line was also measured at different slit-to-crystal distances. The results of these measurements are presented in Fig. 23. As shown the best energy resolution was found for a focal distance of 315.2 cm. However, for this measurement a small asymmetry is observed on the low energy side of the x-ray line (Fig. 24a). The asymmetry disappears when the optimum focal distance is detuned by about 1 cm but then the resolution becomes somewhat worse (Fig. 24b).

The instrumental energy resolution of the spectrometer can also be improved by measuring the x-ray spectra at higher diffraction orders. To demonstrate this effect, the Gd  $K\alpha_1$  x-ray line was observed at five different orders of diffraction. The obtained FWHM energy resolutions are shown in Fig. 25 as a function of the diffraction order. From the figure one can see that the instrumental response between the first and the fifth order is improved by a factor of about 5. Actually, according to formula (20) the improvement factor of the resolution is simply given by the ratio  $\text{ctg}(\theta_{n=1})/\text{ctg}(\theta_{n=5}) = 5.22$ . However, as shown in Fig. 25, the spectrometer efficiency, unfortunately, decreases also with the diffraction order. For instance, the intensity drops by a factor of about 25 between the 1<sup>st</sup>

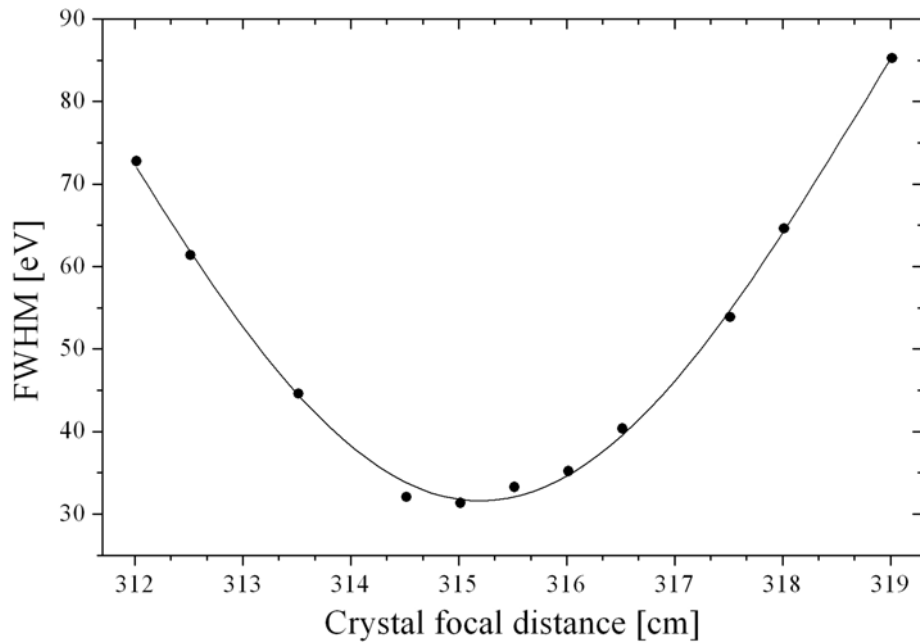


FIGURE 23: Variation of the energy resolution of the spectrometer as a function of the focal distance of the crystal. The measurements were performed using the Gd  $K\alpha_1$  x-ray transition. The dots represent the Gaussian widths obtained from the fits of the  $K\alpha_1$  x-ray line and the solid line the 2<sup>nd</sup> degree polynomial interpolation of the experimental points.

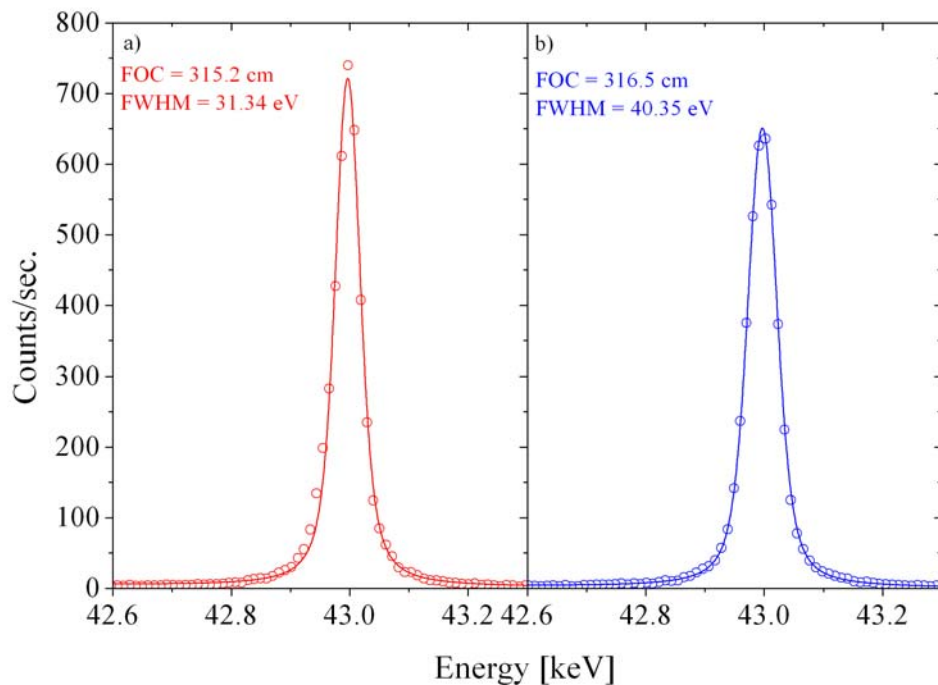


FIGURE 24: Gd  $K\alpha_1$  x-ray line measured at two different focal distances: 315.2 cm (a) and 316.5 cm (b). The dots represent the experimental data and the solid lines the total fits.

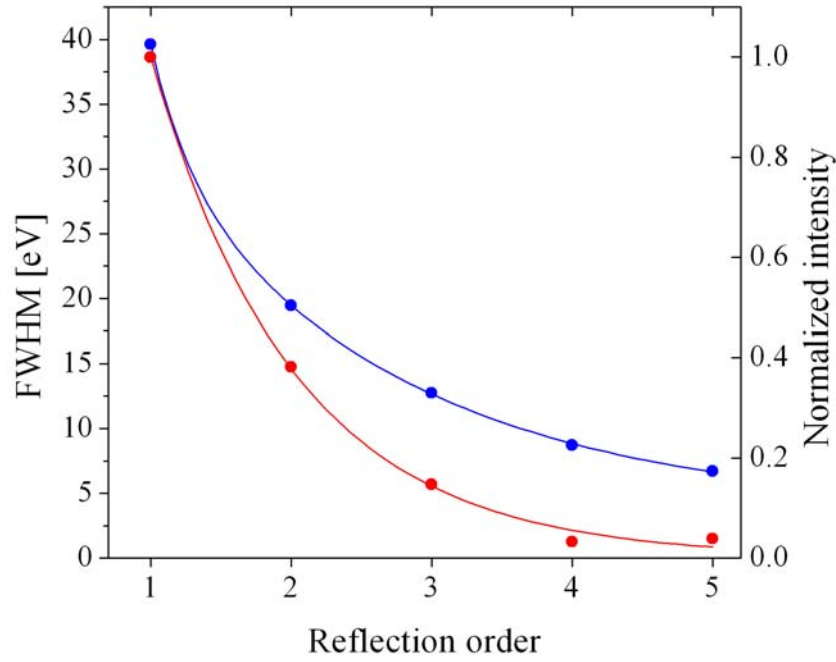


FIGURE 25: Variation of the energy resolution (blue dots) and relative intensity (red dots) of the Gd  $K\alpha_1$  x-ray line as a function of the diffraction order. The solid lines serve only to guide the eye.

and 5<sup>th</sup> order of diffraction. This diminution in intensity which is the price to pay for the resolution improvement is partly due to the diminution of the structure factor  $F_{hkl}$  of the crystal for increasing diffraction orders.

#### 4.1.3 Novel self-consistent method to determine the spectrometer resolution

The above mentioned error on the angular resolution ( $\Delta\sigma_{instr,g} = \pm 0.04$  arcsec) obtained with the standard method using the known natural width of the  $K\alpha_1$  transition of Gd corresponds to the error given by the fitting procedure for the free parameter  $\sigma_{instr,g}$ . The uncertainty on the natural width of the transition is not included. If the latter is considered ( $\Delta\Gamma_{nat,E} = \pm 2.11$  eV for the Gd  $K\alpha_1$  transition [28]), the error  $\Delta\sigma_{instr,g}$  becomes significantly bigger (0.18 arcsec in 1<sup>st</sup> diffraction order). The precision of the method is thus limited by the uncertainties of the natural widths of the transitions used as references. In addition the natural widths expressed in arcsec should have the same order of magnitude as the FWHM angular resolution to get reliable results. To circumvent these



difficulties,  $\gamma$ -rays can be used instead of x-rays because the natural line widths of  $\gamma$ -rays are nearly-zero due to the much longer lifetime of the excited nuclear states as compared to the atomic ones. However, due to the low efficiency of the crystal spectrometer, very intense radioactive  $\gamma$ -sources with activities of  $\sim 10^{10}$  Bq are needed. Such sources can be produced by irradiating enriched isotopes with thermal neutrons provided that the chosen isotopes have large neutron-capture cross sections and the formed unstable isotopes long enough half-lives (several days). In addition, the transportation of such strong radioactive sources is complicated and onerous, especially when the source is irradiated at foreign nuclear reactor facilities. Finally, it should be noted that enriched isotopes are in most cases rather expensive. For all these reasons, the  $\gamma$ -ray solution is neither the ideal one.

We have thus developed a novel method in which the natural width of the measured transition has not to be known. In this method, fluorescence x-ray lines are observed at different orders of diffraction and on both sides of reflection so that the measured angular spectra can be calibrated in energy. The basic idea of the method resides in the fact that, in first approximation, the angular instrumental broadening of the DuMond spectrometer does not depend on the Bragg angle, i.e., the angular resolution of the spectrometer can be considered as nearly constant for different diffraction orders. In other words, according to Eq. (20b), the instrumental energy resolution can be parameterized using a single unknown,  $\Gamma_{nat,g}$  for all diffraction orders. For the Lorentzian width of the transition, no difficulty is encountered since the method applies to energy spectra for which the natural line width (in eV) remains the same for any diffraction order. Now, since for each diffraction order the FWHM width of the Voigtian used to fit the x-ray transition is equal to the width resulting from the convolution of the Gaussian instrumental response with the Lorentzian shape of the transition, a system of equations with two unknowns, the instrumental resolution  $\sigma$  and the natural width of the transition  $\Gamma_{nat}$ , can be obtained from the set of measurements. To solve the system of equations, the transition has to be measured at least at two different diffraction orders. However, the method is more accurate if the measurements are carried out at more than two orders of diffraction and the system of equations is solved by means of a non-linear least-squares fitting method. For this reason, the  $K\alpha_I$  x-ray transition of Gd was measured at five diffraction

orders, namely at  $n = 1, 2, 3, 4$  and  $5$  and for each order on both sides of reflection.

Mathematically, the novel method consists in minimizing the function  $S(\sigma_{instr,g}, \Gamma_{nat,E})$  given by:

$$S(\sigma_{instr,g}, \Gamma_{nat,E}) = \sum_{i=1}^5 \left[ \frac{\Gamma_{obs,i} - V_i(\sigma_{instr,g}, \Gamma_{nat,E})}{\Delta\Gamma_{obs,i}} \right]^2, \quad (22)$$

where  $i$  stands for the diffraction order,  $\Gamma_{obs,i}$  and  $\Delta\Gamma_{obs,i}$  for the total width and corresponding error obtained from the fit for the x-ray line measured at the  $i$ -th diffraction order [55.48(18) eV for  $n = 1$ , 36.95(11) eV for  $n = 2$ , 31.61(6) eV for  $n = 3$ , 28.94(10) eV for  $n = 4$  and 27.86(8) eV for  $n = 5$ , respectively] and  $V_i(\sigma_{instr,g}, \Gamma_{nat,E})$  represents the width of the Voigtian function used to reproduce the profile of the line. To find the values of the unknowns  $\sigma_{instr,g}$  and  $\Gamma_{nat,E}$ , one must solve the system of equations:

$$\frac{\partial S}{\partial \sigma_{instr,g}} = 0, \quad (23a)$$

$$\frac{\partial S}{\partial \Gamma_{nat,E}} = 0. \quad (23b)$$

Unfortunately, due to the integral form of the Voigtian function, the system of equations (23) does not yield on analytic solutions. We have therefore approximated the Voigtian widths by the following expression:

$$V_i(\sigma_{instr,g}, \Gamma_{nat,E}) = \left[ \left( \frac{2\sqrt{2} \cdot \ln 2 \cdot E}{\text{tg}(\theta_i)} \cdot \sigma_{instr,g} \right)^{\alpha_i} + \Gamma_{nat,E}^{\alpha_i} \right]^{\frac{1}{\alpha_i}}. \quad (24)$$

The parameters  $\alpha_i$  were determined by using for the widths  $V_i(\sigma_{instr,g}, \Gamma_{nat,E})$  the fitted values  $\Gamma_{obs,i}$ , for  $\sigma_{instr,g}$  the value of 4.82 arcsec =  $2.34 \cdot 10^{-5}$  rad obtained with the standard method and for  $\Gamma_{nat,E}$  the value reported in [28]. The following results were found:  $\alpha_1 = 1.35$ ,  $\alpha_2 = 1.44$ ,  $\alpha_3 = 1.51$ ,  $\alpha_4 = 1.56$  and  $\alpha_5 = 1.60$ . One sees that the parameters  $\alpha_i$  vary only smoothly with the diffraction order. In addition, there were found to be not very sensitive on the values chosen for  $\sigma_{instr,g}$  and  $\Gamma_{nat,E}$  so that the approximation (24) is justified. Using the approximation (24) in (22), the system of equations (23) can be solved

analytically. To estimate the errors on the solutions  $\sigma_{instr,g}$  and  $\Gamma_{nat,E}$  the error matrix  $E_{ij}$  is formed. The inverse of this error matrix is defined by:

$$(E^{-1})_{ij} = \frac{1}{2} \frac{\partial^2 S}{\partial a_i \partial a_j}, \quad (25)$$

where  $a_1$  and  $a_2$  are equal to  $\sigma_{instr,g}$  and  $\Gamma_{nat,E}$ , respectively. The variance and covariance of the solutions are then given by:

$$var(\sigma_{instr,g}) = (\Delta\sigma_{instr,g})^2 = E_{11}, \quad (26a)$$

$$var(\Gamma_{nat,E}) = (\Delta\Gamma_{nat,E})^2 = E_{22}, \quad (26b)$$

$$covar(\sigma_{instr,g}, \Gamma_{nat,E}) = E_{12} = E_{21}. \quad (26c)$$

With the above described novel method, values of  $\sigma_{instr,g} = 2.332(19) \cdot 10^{-5}$  rad = 4.81(4) arcsec and  $\Gamma_{nat,E} = 25.61(36)$  eV were found. It can be noted that the result provided by the self-consistent method for  $\sigma_{instr,g}$  is fully consistent with the value of 4.82(18) arcsec obtained with the standard method but about 5 times more accurate. The same holds for the natural line width  $\Gamma_{nat,E}$  which fairly agrees with the value of  $(26.1 \pm 2.2)$  eV reported in [28] but is also more precise.

As in the above method some approximations were employed, another approach was probed in which the five angular spectra were fitted simultaneously by means of the PeakFit program. For each diffraction order, the natural line width  $\Gamma_{nat,g}(n)$  was represented as a function of  $\Gamma_{nat,g}(n=1)$  using the following expression derived from Eq. (19):

$$\Gamma_{nat,g}(n) = \frac{tg[\theta_B(n)]}{tg[\theta_B(n=1)]} \Gamma_{nat,g}(n=1). \quad (27)$$

Using the simplified notations  $\Gamma_{nat} := \Gamma_{nat,g}(n=1)$ ,  $\sigma := \sigma_{instr,g}$  and  $f_i := tg[\theta_B(i)]/tg[\theta_B(1)]$ , the following function was employed in the Peakfit program to fit the angular spectrum resulting from the sum of the five x-ray lines:

$$F(\theta) = \sum_{i=1}^5 \frac{a_{0,i}}{\sqrt{2} \cdot \pi \cdot \sigma \cdot (\Gamma_{nat} \cdot f_i)} \int_0^{+\infty} e^{-\frac{1}{2} \left( \frac{\theta - \theta_i}{\sigma} \right)^2} \frac{1}{1 + \left( \frac{\theta - \theta_i - t}{(\Gamma_{nat} \cdot f_i)} \right)^2} dt. \quad (28)$$

In the fit, the parameters  $a_{0,i}$  which correspond to the areas under the peaks, the line centroids  $\theta_i$ , as well as the two parameters of interest  $\sigma$  and  $\Gamma_{nat}$  were let free. The angular spectra corresponding to the five orders of diffraction and fitted with the function  $F(\theta)$  are depicted in Fig. 26. From the fitting procedure the following values were obtained:  $\sigma = 0.001318(4)$  deg. and  $\Gamma_{nat} = 0.002051(7)$  deg. Rewriting these values in the proper units and using Eq. (20a) to transform  $\Gamma_{nat}$  in eV, one finds:  $\sigma_{instr,9} = 4.75(2)$  arcsec and  $\Gamma_{nat,E} = 26.18(9)$  eV.

The results obtained for  $\sigma_{instr,9}$  and  $\Gamma_{nat,E}$  are summarized in Table III. As shown, the three values of  $\sigma_{instr,9}$  are consistent within the combined uncertainties and the errors are much smaller for the two self-consistent methods. The same holds for  $\Gamma_{nat,E}$ , except that the two values corresponding to the two self-consistent methods are in slight disagreement, their difference being 0.57 eV and the combined error 0.45 eV. It is also somewhat surprising that the second self-consistent method based on the simultaneous fit of the five x-ray lines is significantly more accurate than the first one. A possible explanation might be that in the second method the degree of freedom, i.e., the number of data diminished by the number of free fitting parameters is  $5 \times 100$  points – 12 free fitting parameters = 488, whereas the one of the first method is only 5 equations – 2 unknowns = 3. In addition, in the second method all points of the spectra are used in the least-squares fit procedure and not only the widths of the lines. This is important since the information

TABLE III: Comparison between the results obtained for  $\sigma_{instr,9}$  and  $\Gamma_{nat,E}$  with the three methods. With the first method,  $\Gamma_{nat,E}$  cannot be determined. The value of  $(26.1 \pm 2.1)$  eV reported in [28] was used.

Method	$\sigma_{instr,9}$ [arcsec]	$\Gamma_{nat,E}$ [eV]
Standard	4.82(18)	–
Self-consistent (widths)	4.81(4)	25.61(36)
Self-consistent (simultaneous fit)	4.75(2)	26.18(9)

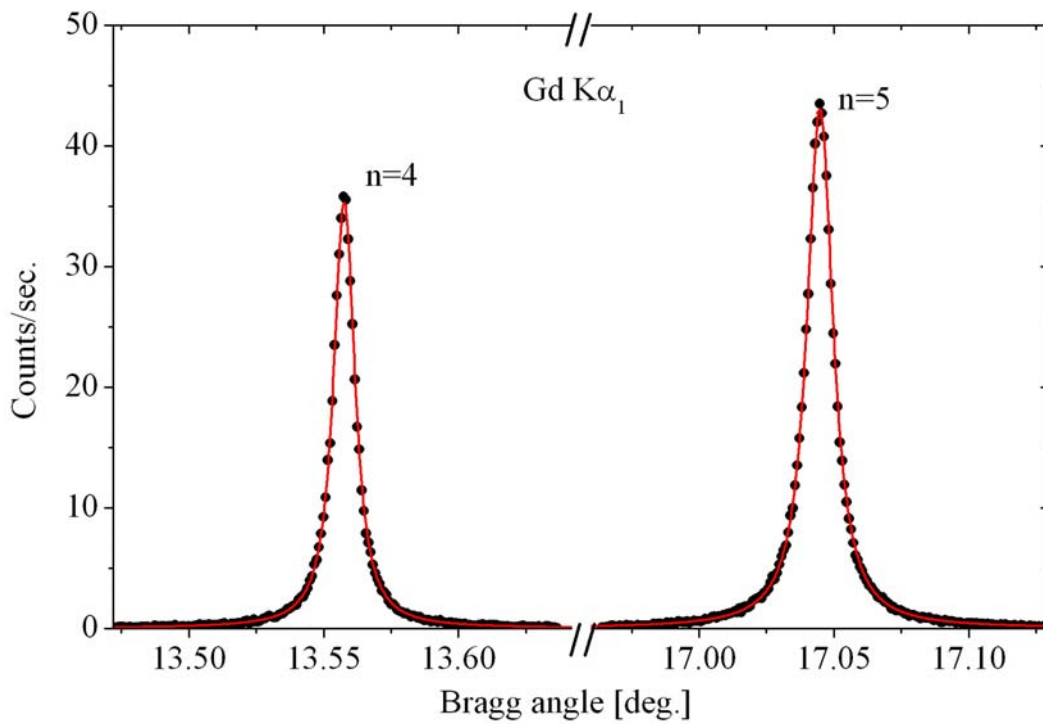
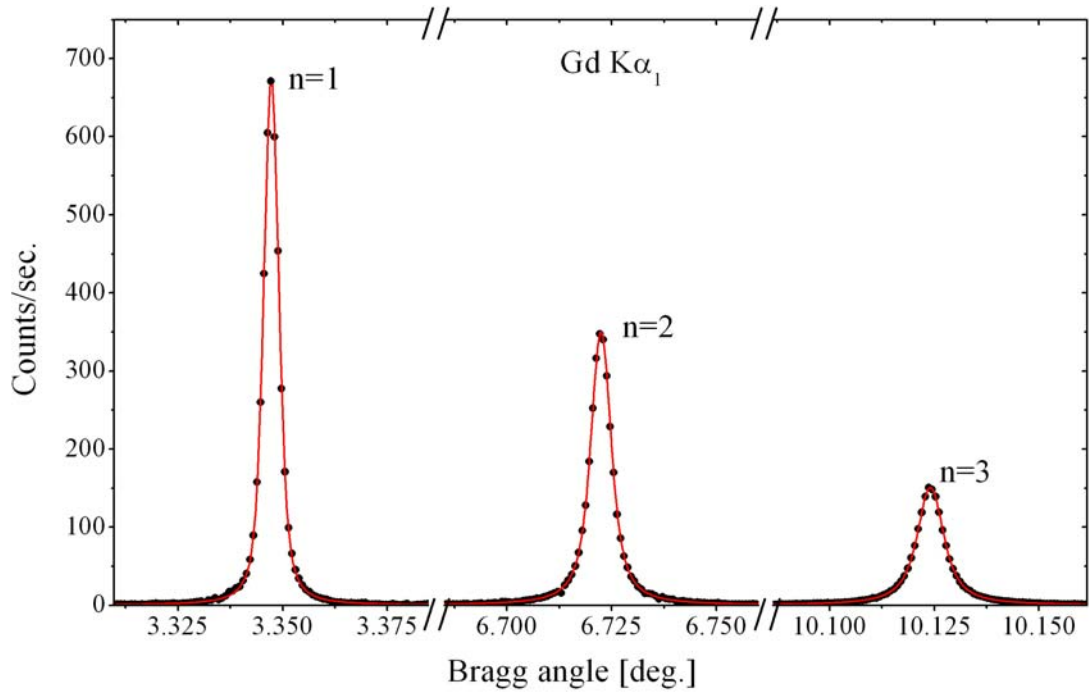


FIGURE 26: Gd  $K\alpha_1$  x-ray emission line measured at five diffraction orders. The dots represent the experimental data and the red solid line the total simultaneous fit of the data.

about the relative contribution of the Lorentz and Gauss functions to the Voigt profile is also contained in the tails of the x-ray lines. Depending on the relative widths of the two functions, the resulting Voigtian  $V(x)$  is indeed characterized by tails decaying rather like  $1/x$  in the case  $\Gamma_{nat} > \sigma$  and  $1/x^2$  in the opposite case  $\Gamma_{nat} < \sigma$ .

## 4.2 Spectrometer sensitivity

Despite its small solid angle the DuMond curved crystal spectrometer is characterized by good peak-to-background ratios and thus by a high sensitivity. This results in particular from the numerous efforts done to minimize the background. In order to illustrate the sensitivity of the instrument the extremely weak Gd  $K\alpha_3$  x-ray emission line corresponding to the dipole-forbidden  $2s_{1/2} \rightarrow 1s_{1/2}$  transition was measured. The same Gd target, x-ray tube and experimental set-up as the ones used in the instrumental resolution measurements were employed. As mentioned before, the best angular resolution is obtained when the slit-to-crystal distance is adjusted for each measured x-ray line. However, when the measured x-ray spectrum extends over a large angular range with many lines or if the spectrum, like in the present case, contains a very weak line this optimization is not so convenient. It is then more practical to measure the x-ray spectrum with an average value of the focusing distance or, in the case of a weak line, with the focusing distance corresponding to the nearest strong line. For the  $K\alpha_3$  transition, the latter solution was chosen, i.e., the measurements were performed with the focusing distance corresponding to the Gd  $K\alpha_2$  transition.

Because for measurements performed with the DuMond spectrometer the x-ray spectra are measured point by point, the time needed to measure a whole spectrum containing a weak line can be very long if the same collecting time per point is employed for all points. For this reason, the measurements were performed in two steps. First the  $K\alpha_{1,2}$  spectrum was measured on both sides of reflection in order to determine the zero Bragg angle required for the energy calibration of the spectrometer. The  $K\alpha_{1,2}$  spectrum measured on the right side of reflection was used later on to determine the  $K\alpha_1$  and  $K\alpha_2$  line shapes. A precise knowledge of these line shapes was indeed crucial for a correct determination of the position and intensity of the weak  $K\alpha_3$  line. In the second step the angular range corresponding to the energy region of the  $K\alpha_3$  transition was measured on the right side of reflection in 28 successive step by step scans. Each scan contained 200 equidistant points and the acquisition time per point was 200 sec. Furthermore, in order to control the instrumental reproducibility and the stability of the x-ray tube intensity, which was particularly important for these long time measurements, a short measurement of the

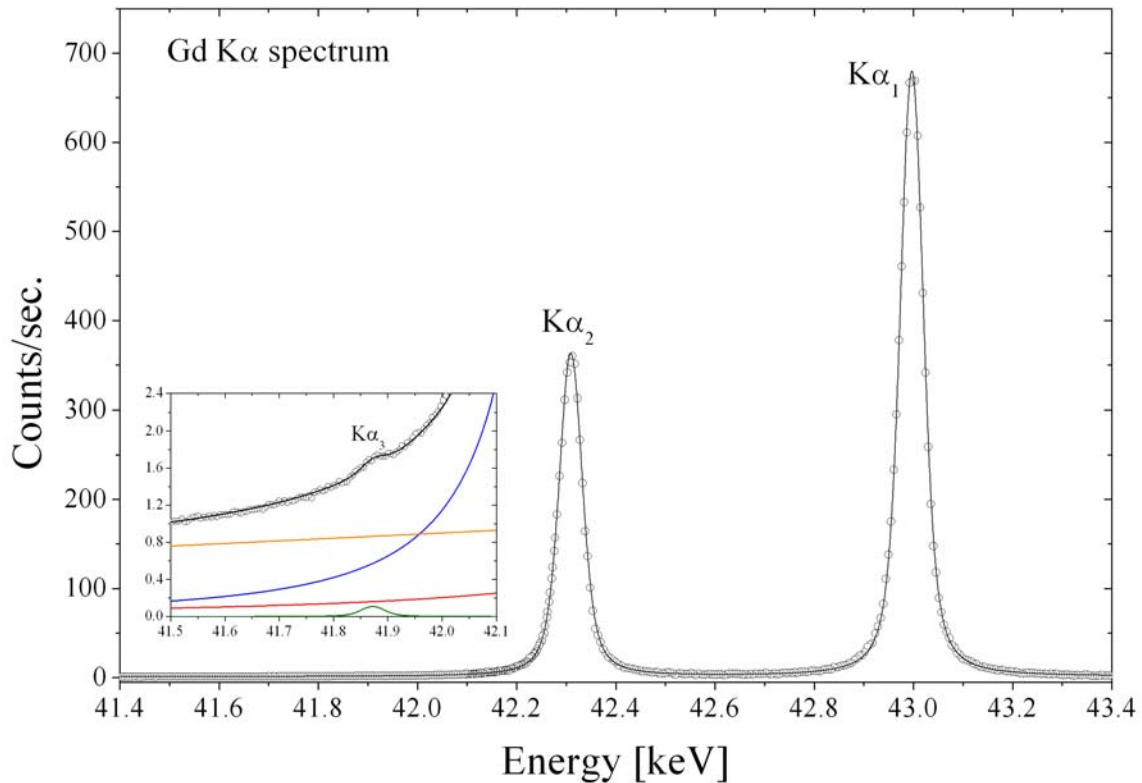


FIGURE 27: The  $K\alpha$  x-ray spectrum of Gd. The dots represent the experimental data and the black solid line the total fit. The inset shows the enlarged energy region of the  $K\alpha_3$  transition with the components used in the fit: tail of the  $K\alpha_1$  line (red curve), tail of the  $K\alpha_2$  line (blue curve), linear background (orange straight line) and  $K\alpha_3$  line (green curve).

$K\alpha_2$  x-ray line was performed between each fourth scan. The analysis showed, however, that the fluctuations of the intensity of the  $K\alpha_2$  line were smaller than 1.4% and the instabilities of the line position less than 0.8 eV. For this reason, no off-line corrections of the data were performed and the recorded twenty-eight scans were simply added together.

The measured Gd  $K\alpha$  spectrum is presented in Fig. 27. As shown, in the energy region corresponding to the  $K\alpha_3$  line, the main contribution to the measured intensity originates from the low energy tail of the  $K\alpha_2$  line and the linear background, some additional contribution is due to the low energy tail of the  $K\alpha_1$  line but only a very tiny part comes from the forbidden  $K\alpha_3$  transition. Therefore to fit properly the  $K\alpha_3$  x-ray spectrum shown in the inset, a two step procedure was employed.

In the first step, the  $K\alpha_1$  and  $K\alpha_2$  lines were fitted in order to determine the



intensity of the tails in the region corresponding to the  $K\alpha_3$  transition. In the fitting procedure the intensities, energies and Gaussian widths of the x-ray lines were let free, whereas the Lorentzian widths were kept fixed at the values quoted in the tables of Campbell and Papp [28]. Then, the fitted low energy tails of the  $K\alpha_1$  and  $K\alpha_2$  lines were subtracted from the measured total spectrum. In the second step, the residual spectrum was analyzed. The  $K\alpha_3$  line was fitted with the same method as the one used for the  $K\alpha_{1,2}$  lines. However, due to the extremely poor intensity of this transition, only the energy and the intensity were let free in the fitting procedure, the Gaussian and Lorentzian widths being kept fixed. The Gaussian width was calculated from the known angular instrumental resolution while the Lorentzian width was derived from the atomic level widths quoted in [28].

For the energy of the  $K\alpha_3$  transition, a result of  $41870 \pm 2$  eV was obtained. The latter was found to be consistent, within the experimental uncertainties, with another existing experimental value reported in Ref. [29] and with the theoretical prediction given in [26]. Concerning the relative intensity of the forbidden transition, a ratio  $I(K\alpha_3)/I(K\alpha_1)$  of  $(1.61 \pm 0.11) \times 10^{-4}$  was found. This result is in good agreement with the experimental value of  $(1.5 \pm 0.1) \times 10^{-4}$  quoted in [29] as well as with a theoretical prediction based on Scofield's calculations which gives a value of  $1.7 \times 10^{-4}$  [30].

A further example illustrating the high sensitivity of the DuMond spectrometer is given in the second part of this thesis in which measurements of the photoinduced  $K\alpha$  hypersatellite lines of molybdenum are presented and discussed. As a double ionization of the  $K$ -shell by photoionization is only possible via sequential processes, a photoelectric effect followed by a TS1 or shake process, the probability for a double  $K$ -shell photoionization is extremely weak, especially for mid- $Z$  elements such as Mo, and the hypersatellite transitions decaying the double  $1s$  vacancies are very difficult to observe.

### 4.3 Spectrometer precision

In the DuMond spectrometer the Bragg angles are measured by means of an optical laser interferometer with a precision of a few marcsec (see Fig. 10). As the lattice spacing constant  $d_{110}$  of the quartz crystal was also determined with a high accuracy (about 5 ppm), the precision on the energies measured with the spectrometer depends mainly on the errors related to the fitting procedure. If the measured transitions are intense, the errors from the fit are small and the precision is of the order of  $10^{-5}$ . However, as shown by Eq. (21), for a given uncertainty on the Bragg angle the corresponding uncertainty on the energy varies with the squared energy ( $\Delta E \propto E^2$ ). As a consequence, for the same angular precision, the same diffraction order and the same fitting error, the energy determination of a x-ray line of 80 keV will be 16 times less accurate than that of a 20 keV x-ray line.

In order to probe the precision of the energies determined with the DuMond spectrometer, the  $K\alpha_2$  (K–L<sub>2</sub> transition),  $K\beta_1$  (K–M<sub>3</sub> transition) and  $K\beta_{17}$  (L<sub>2</sub>–M<sub>3</sub> transition) x-ray lines of gold were measured. The objective of these measurements was to probe the precision of the spectrometer by means of the Ritz combination principle. According to the latter, the sum of the energies of the K–L<sub>2</sub> and L<sub>2</sub>–M<sub>3</sub> transitions should indeed be equal to the energy of the K–M<sub>3</sub> transition. A serious difficulty of these measurements was that the energy domain corresponding to the three transitions extended over about 70 keV. A further and still more challenging problem was that the energy of the L<sub>2</sub>–M<sub>3</sub> transition (10.6 keV) was far below the lowest energy that can be measured with Laue type crystal spectrometers for which the minimum energy is usually around 20 keV. Nevertheless, thanks to the wide angular range covered by the DuMond spectrometer of Fribourg and the thinness of the employed quartz crystal, the project could be carried out successfully and the Ritz principle verified within a precision of about  $10^{-5}$ .

In these measurements the x-ray tube gold anode itself served as the source of the radiation of interest. The x-ray tube was positioned so that the axis of the emitted bremsstrahlung and characteristic radiation was parallel to the target–crystal direction (a setup named direct geometry). The position of the slit was adjusted transversally so that the crystal viewed the center of the electron beam spot on the x-ray tube anode. It has to be noted that in the direct geometry setup employed for these measurements, the

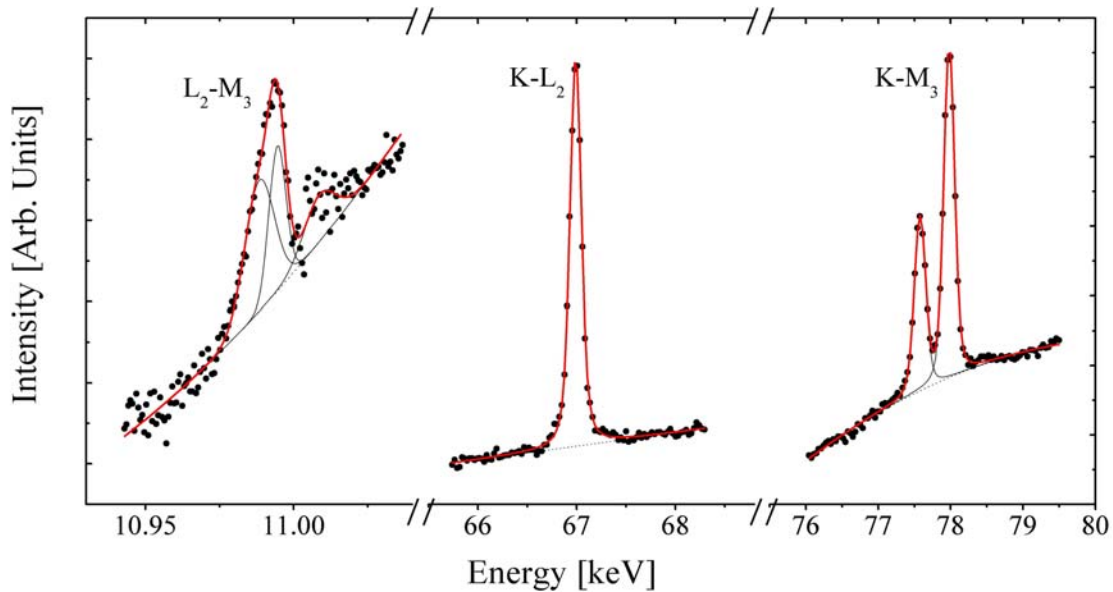


FIGURE 28: Measured  $L_2-M_3$ ,  $K-L_2$  and  $K-M_3$  transitions of gold (dots). The red solid lines show the total fits to the experimental data points. The pronounced slope observed in the  $L_2-M_3$  spectrum originates from the bremsstrahlung of the electrons.

characteristic fluorescence of Au was produced by electron impact and not by photoionization as in the other projects presented in this thesis. The tube was operated at 90 kV and 30 mA. The  $K\alpha_2$  and  $K\beta_1$  x-ray lines were observed on both sides of reflection in order to determine for each of them the spectroscopic zero position (origin of the Bragg angles scale) required for the energy calibration of the spectrometer. Later on, only the lines measured on the positive side of reflection were used for the energy determination. The measured  $K\alpha_2$  and  $K\beta_1$  spectra contained 100 and 150 equidistant points, respectively. For the strong  $K\alpha_2$  line, the acquisition time per point was 30 sec., whereas for the weaker  $K\beta_1$  line a time of 250 sec. was chosen. Because the  $L\beta_{17}$  ( $L_2-M_3$  transition) is very weak, the origin of the Bragg angles scale was determined by measuring on both sides of reflection the stronger and relatively close lying  $L\beta_1$  x-ray line ( $L_2-M_4$  transition). The angular range corresponding to the energy region of the  $L\beta_{17}$  line was then measured on the right side of reflection in several successive step by step scans. Each scan contained 140 equidistant points and the total acquisition time per point was 2300 sec. The stability of the experimental setup was checked periodically by inserting short measurements of the  $L\beta_1$  x-ray line between each scan.

TABLE IV: Energies of the  $K-L_2$ ,  $L_2-M_3$  and  $K-M_3$  transitions of Au.

	$K-L_2$ [eV]	$L_2-M_3$ [eV]	$K-M_3$ [eV]
This work	$66990.83 \pm 0.26$	$10990.21 \pm 0.29$	$77979.92 \pm 0.52$
Ref. [26]	$66990.73 \pm 0.22$	$10991.54 \pm 0.72$	$77979.80 \pm 0.38$

TABLE V: Comparison between the sum of the energies of the  $K-L_2$  and  $L_2-M_3$  cascading transitions and the energy of the crossover  $K-M_3$  transition.

	$K-L_2 + L_2-M_3$ [eV]	$K-M_3$ [eV]	$[K-M_3 - (K-L_2 + L_2-M_3)]$ [eV]
This work	$77981.04 \pm 0.39$	$77979.92 \pm 0.52$	$-1.12 \pm 0.65$
Ref. [26]	$77982.27 \pm 0.75$	$77979.80 \pm 0.38$	$-2.47 \pm 0.84$

The energy spectra were fitted with Voigt functions. In the fitting procedure the Lorentzian widths, taken from Ref. [28] and the known instrumental Gaussian width, were kept fixed, whereas the intensities and centroid energies as well as the parameters of the linear background were let free. In order to fit properly the weak  $L_2-M_3$  quadrupole transition two Voigtians had to be used so that the energy of this transition was determined from the weighted average of the energies of the two components. The fitted spectra are presented in Fig. 28 and the obtained energies in Table IV. In Table V, the sum of the energies of the two cascading transitions is compared to the energy of the crossover transition to verify the Ritz principle.

As it can be seen from Table V, a small but significant deviation from the Ritz principle is observed in our measurements. The same holds but in a more pronounced way for the energies quoted in Ref. [26]. The origin of the discrepancy is not clear but we are tempted to explain it by the energy of the  $L_2-M_3$  transition which seems to be somewhat too high even if the value deduced from our measurements is 1.3 eV lower than the one reported in [26]. Actually, the shape of the  $L_2-M_3$  transition evinces some asymmetry so that it was not possible to fit it with a single Voigtian. In our opinion, this asymmetry might indicate that the  $L_2$  or  $M_3$  atomic level is affected by some interaction (solid state or chemical effect) which slightly modifies the energy of this level and consequently the energy and the shape of the transition. Another and maybe simpler explanation could be the following: since the  $L_2$  vacancies are partly created via  $L_1L_2N$  Coster-Kronig

transitions,  $L_2^{-1}N^{-1}$  double vacancy states are created. The radiative decay of these double vacancy states gives then rise to  $N$ -satellite x-ray lines on the high-energy side of the  $L_2$ - $M_3$  transition. As the energy shift of these  $N$ -satellites is smaller than the natural line widths of the transitions, the satellites cannot be resolved from the  $L_2$ - $M_3$  diagram line so that the latter is slightly shifted to a higher energy.

## 4.4 Additional examples of applications

### 4.4.1 Measurements of the Au $L$ x-ray lines series

X-ray lines belonging to the  $L$ -series are more numerous than those corresponding to the  $K$ -series. They are also generally weaker, broader, and have more complex profiles. As it can be seen from Fig. 29, which shows the radiative  $L$  diagram transitions of Gold, the  $L$  x-ray spectrum consists of three major groups: the  $L\alpha$ ,  $L\beta$  and  $L\gamma$  lines. In the present project the energies and line widths of 13  $L$  x-ray lines among those depicted in Fig. 29 were measured and the results compared to other available experimental and theoretical data. The goal of this project was to obtain a set of modern and reliable data for the  $L$  x-rays of Au. High-resolution  $L$  x-ray data of heavy elements are indeed still scarce in the literature and existing ones are in most cases rather old. Experimental data are scarce because the energies of  $L$  x-rays of heavy elements range approximately between 10 and 20 keV, an energy domain which is hardly accessible for crystal spectrometers. Most Laue-type crystal spectrometers are indeed employed for photon energies above 20 keV, whereas Bragg-type crystal spectrometers cannot be used in general above 10 keV. In this energy region, there is thus a lack of high-resolution x-ray data. A precise knowledge of the energies and line widths of  $L$  x-ray lines is, however, very useful in many domains using x-ray photons (XRF analysis technique, plasma diagnostics, x-ray imaging, etc.). In high-resolution x-ray spectroscopy, reliable energies and line widths are also helpful because they permit to improve the data analysis by diminishing the number of free fitting parameters. Furthermore, in experiments in which weak structures have to be extracted from the tails of close lying and much more intense diagram lines, the shape and position of the latter must be known precisely to obtain reliable results.

The measurements were performed in the direct geometry setup using the gold anode of the x-ray tube as the source of the characteristic  $L$  x-ray emission. The x-ray tube was operated at 40 kV and 40 mA. For the  $L_1$ ,  $L_2$  and  $L_3$ -subshells of gold, the ionization threshold energies lie at 14.353 keV, 13.734 keV and 11.919 keV, respectively. The chosen voltage of 40 kV was thus 3 times higher or more than the threshold energies, which is sufficient for a strong characteristic  $L$  x-ray emission. At the same time, the bremsstrahlung whose intensity grows approximately with the squared value of the

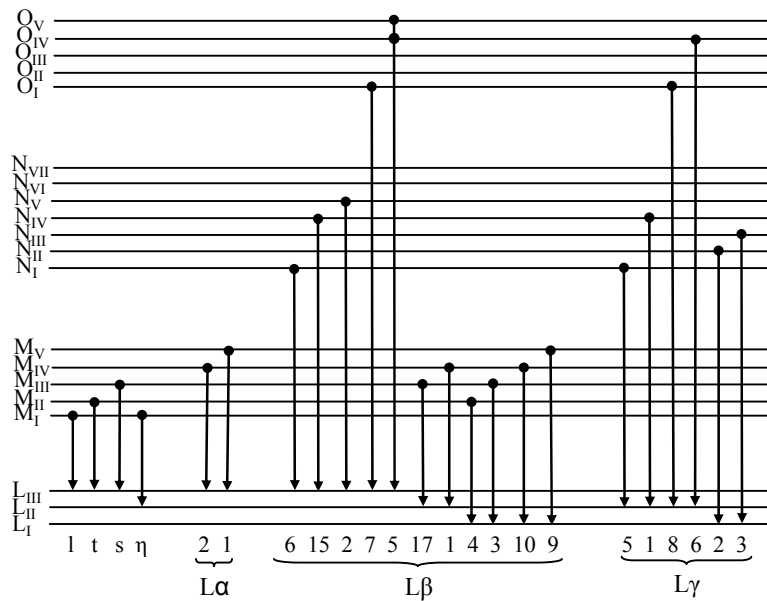


FIGURE 29: The L diagram x-ray lines of Au.

high-voltage and represents the main source of background in the direct geometry setup was kept at a reasonable value. A slit width of 0.10 mm was employed as the best compromise between a high enough spectrometer luminosity and an acceptable instrumental resolution.

The  $L$  x-ray spectrum of gold extends approximately between 8.5 keV ( $L_{\ell}$  transition) and 13.8 keV ( $L\gamma_3$  transition). Such energies are very low for a transmission-type crystal spectrometer, mainly because the absorption of the diffracted x-rays by the crystal is dramatically large. For this reason, even if the Bragg angle (17.3 deg.) corresponding to the  $L_{\ell}$  transition is included in the angular range of  $\pm 20$  deg. covered by the DuMond spectrometer of Fribourg, this line could not be measured, the absorption in the crystal being higher than 98%. The same holds for the three other transitions belonging to the same group as the  $L_{\ell}$  one (see Fig. 29). The transition with the lowest energy that could be measured was the  $L\alpha_2$  so that the energy domain of the measured  $L$  x-ray transitions extended from 9.6 keV up to 13.8 keV. The corresponding Bragg angles ranged between 15.2 and 10.6 deg. Due to the strong absorption by the crystal of such low energy x-ray photons, which results to poor intensities and

consequently to longer acquisition times, and the broad angular domain to be scanned, the measurements were performed in the following way: the energy domain corresponding to the  $L\alpha$  x-ray spectrum was first measured. This first scan contained 430 equidistant points and the acquisition time was 90 sec. per point. In the second stage of the measurements, the  $L\beta$  x-ray region was scanned. This second measurement consisted of 710 equidistant points with an acquisition time of 60 sec. per point. Finally, the  $L\gamma$  x-ray spectrum was measured using again 710 equidistant points but a shorter acquisition time of 30 sec. per point. Each group of  $L$  x-ray lines was measured with the same focusing distance. The latter was determined using the Bragg angle corresponding to the center of the energy interval covered by the given group of lines. For each group of lines observed at the same focusing distance, the spectroscopic zero position was determined by measuring the most intense line of the group at positive and negative sides of reflection. All x-ray lines were measured in the first order of diffraction.

The observed  $L$  x-ray lines were calibrated in energy and then analyzed by means of the least-squares fitting program PeakFit. The line shapes of the measured transitions were fitted with Voigt profiles. In the fitting procedure only the known Gaussian instrumental broadening was kept fixed while the intensities, energies, Lorentzian widths and the two constants of the linear background were used as free fitting parameters. The fitted high-resolution  $L\alpha$ ,  $L\beta$  and  $L\gamma$  Au x-ray spectra are presented in Figs. 30, 31, and 32, respectively.

The presence of two or more holes in atomic inner shells give rise to satellite x-ray lines that are shifted towards higher energies with respect to the parent diagram lines. In general, the energy shifts of satellites increase with the principal quantum number of the transition electron and decrease with the principal quantum number of the spectator vacancy [31]. As a result, for  $L$  x-rays  $M$  satellites can be well resolved whereas  $N$  satellites are poorly separated from the diagram lines and occur only as asymmetries on the high energy sides of the latter. In addition, as the spectator vacancies can be located in different subshells and many combinations between the two holes are possible in the initial and final state, satellite lines consist of numerous components that vary in energy and intensity. Such resolved  $M$ -satellite lines can be seen in Fig. 31. The satellite structure which is clearly separated from the parent  $L\beta_2$  diagram line was fitted with two



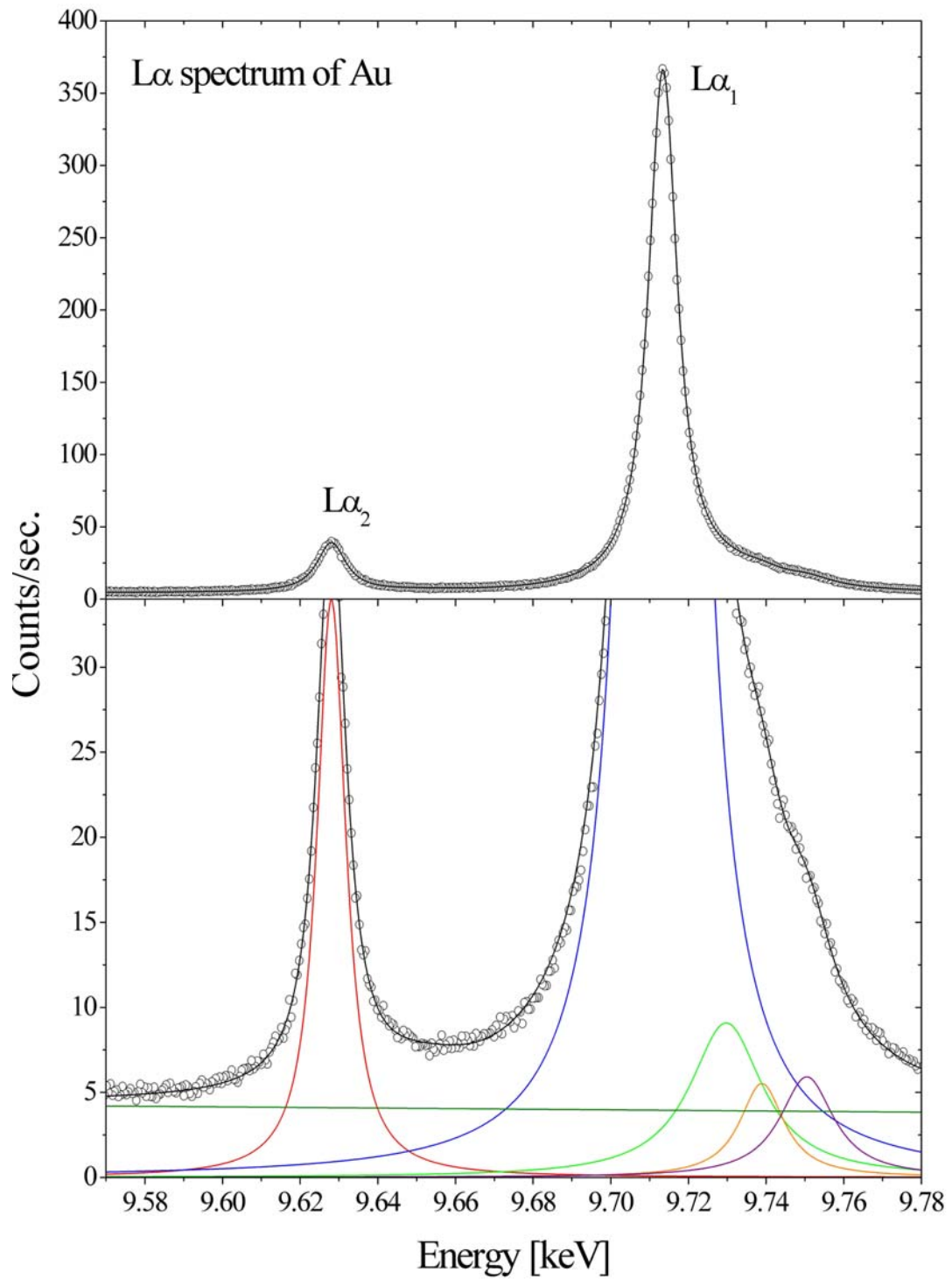


FIGURE 30: The  $La$  x-ray spectrum of  $Au$ . The top part of the figure presents the total fit of the spectrum and the bottom parts shows in more details the fitted components. The three peaks (green, orange and purple) around 9.74 keV correspond to the  $M$ -satellites of the  $L\alpha_1$  x-ray line.

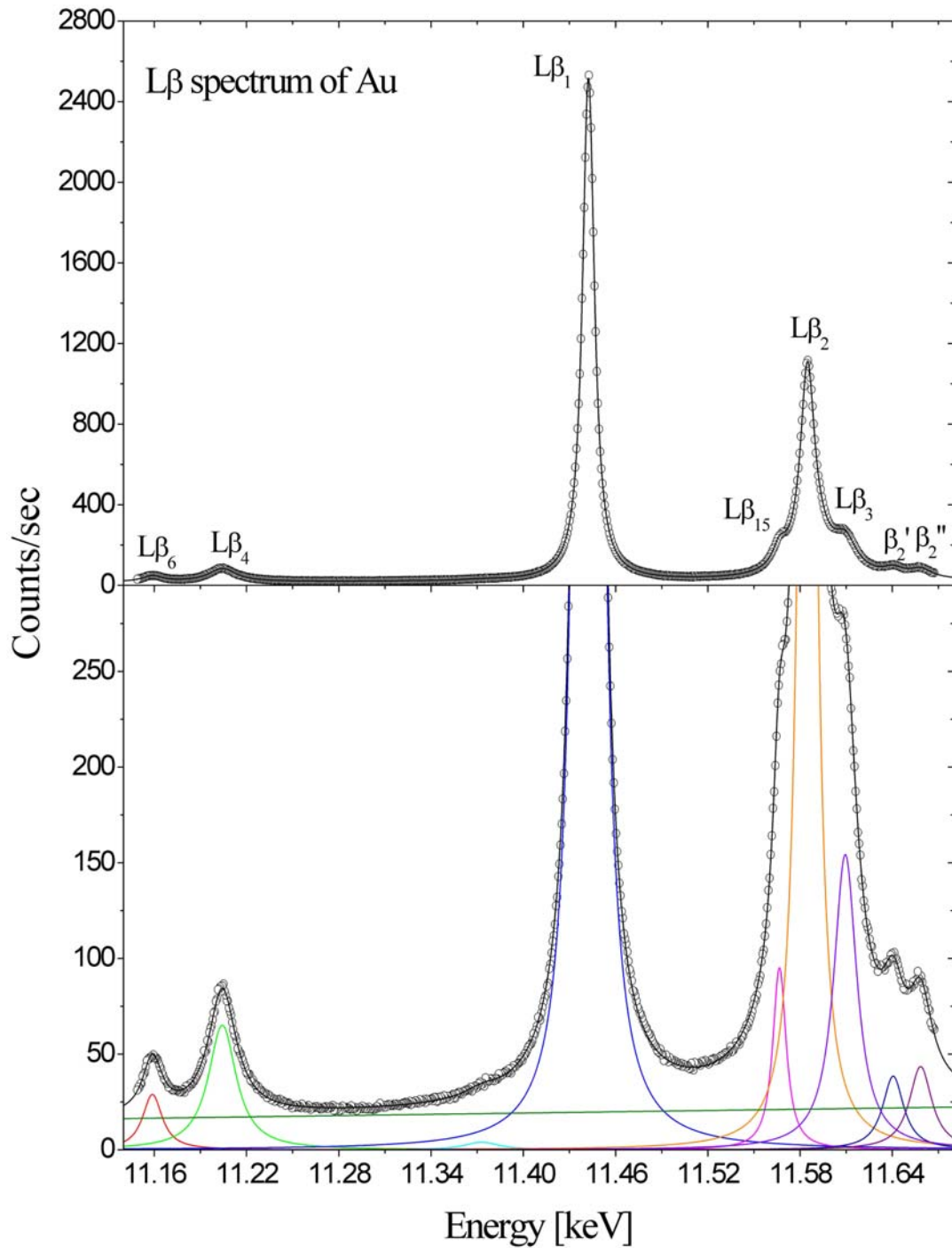


FIGURE 31: The  $L\beta$  x-ray spectrum of Au. The top part of the figure presents the total fit of the spectrum and the bottom parts shows in more details the fitted components. The two peaks (purple and royal) at about 11.64 keV correspond to the M-satellites of the  $L\beta_2$  x-ray line.

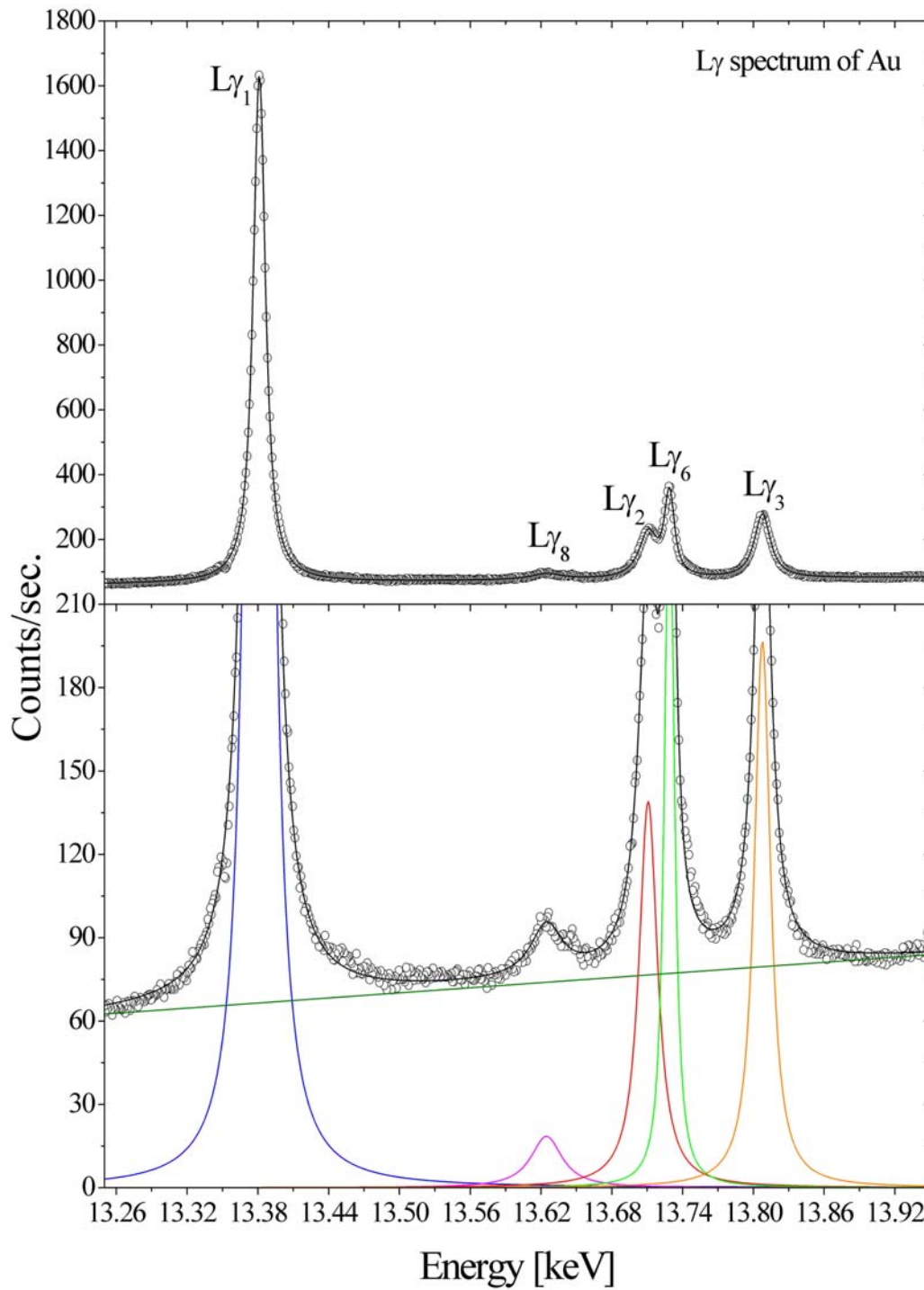


FIGURE 32: The  $L\gamma$  x-ray spectrum of Au. The top part of the figure presents the total fit of the spectrum and the bottom parts shows in more details the fitted components.

components ( $L\beta_2'$  and  $L\beta_2''$ ). The average energy shift is about 6 eV. A similar  $M$ -satellite structure which was fitted with three components (see Fig. 30) is observed for the  $L\alpha_1$  transition but in this case the shift is only about 3 eV. The difference in the shifts can be explained by the principal quantum number of the transition electron which is  $n = 4$  for the  $L\beta_2$  transition and  $n = 3$  for the  $L\alpha_1$  one. It can be noted that  $M$ -satellites were only observed for transitions to the  $L_3$  subshell. This is due to the fact that the  $L_3^{-1}M^{-1}$  double vacancy states, which are the initial states of the observed  $M$ -satellite transitions, are created through  $L_1L_3M_{4,5}$  Coster–Kronig transitions, whereas  $L_1L_2M_{4,5}$  Coster–Kronig transitions, which would lead to the emission of  $M$ -satellites for the  $L_2$  transitions, are energetically forbidden. On the other hand,  $L_{1,2}L_3N$  and  $L_1L_2N$  Coster–Kronig transitions being energetically allowed,  $N$ -satellites should accompany as well  $L_3$  transitions as  $L_2$  ones. They are, however, not observed because, according to the second rule mentioned above about the energy shifts of satellite lines, they are fully overlapping with the parent diagram lines, the energy shifts being smaller than the natural widths of the transitions. The resolved satellite structures were analyzed with several Voigt functions, whose energies, Lorentzian widths and intensities were used as free fitting parameters. The energies obtained from the fits for the  $L\beta_2'$  and  $L\beta_2''$  satellites are 11641.0(5) eV and 11657.8(5) eV, respectively. Both energies are in good agreement with the experimental values of 11658.1(1.2) eV and 11641.7(1.1) eV reported in [32].

The natural line widths of the  $L$  x-ray transitions of Au obtained in the present study are listed in Table VI where they are compared to other available experimental data. As the natural width of an x-ray transition is given by the sum of the widths of the initial and final states, our results are also compared to the values derived from the atomic level widths recommended by Campbell and Papp in Ref. [28]. The errors quoted for the widths obtained in the present work correspond to the errors given by the fitting program. In general, a good agreement is found between our values and those reported in Refs. [32] and [34], an average deviation of about 0.5 eV being observed. The biggest difference concerns the  $L_3-N_5$  transition for which our result is smaller by 1.6 eV. This might indicate that in the studies [32] and [34] the  $M$ -satellite structure of the  $L_3-N_5$  was not completely separated from the parent diagram line, leading to a broadening of the latter. The comparison of our results with the values derived from the level widths recommended

by Campbell and Papp [28] evinces an average deviation of about 1 eV. In general, the widths obtained in the present study are somewhat bigger than those reported in [28], the biggest difference (2.3 eV) being observed for the  $L_1-M_2$  transition. Finally, a satisfactory agreement is also found between our results and the values given in Ref. [33] (average deviation of 0.9 eV), except for the  $L\gamma_8$  line ( $L_2-O_1$  transition) for which a strong discrepancy is observed ( $30.68 \pm 3.2$  eV in our case, 9.5 eV in [33]). We are, however, inclined to believe that the value reported in [33] is wrong because the natural width of the  $O_1$  subshell is expected to be strongly broadened by the fast  $O_1O_{2,3}O_{4,5}$  super-Coster-Kronig transitions and its natural width should be therefore significantly bigger than the one of the  $N_4$  subshell, in contradiction with the widths of 10.8 eV and 9.5 eV reported in [33] for the  $L_2-N_4$  and  $L_2-O_1$  transitions, respectively.

The energies of the measured  $L$  x-ray transition are given in Table VII together with the experimental and theoretical values reported by Deslattes et al. in Ref. [26]. The theoretical energies listed in [26] were obtained from MBPT (Many Body Perturbation

TABLE VI: Comparison of the Au  $L$  x-ray line widths obtained in this work with other available experimental data and with values derived from the atomic level widths reported in [28].

Transition	Width [eV]				
	Present work	Ref. [32]	Ref. [33]	Ref. [34]	Ref. [28]
$L_1-M_2$	$21.6 \pm 0.9$		19.4		$19.3 \pm 2.3$
$L_1-M_3$	$17.8 \pm 0.7$	18.4	20.8		$18.3 \pm 2.1$
$L_1-N_2$	$18.0 \pm 0.4$		17.2		$16.2 \pm 1.7$
$L_1-N_3$	$15.3 \pm 0.2$		15.2		$14.9 \pm 1.6$
$L_2-M_4$	$8.6 \pm 0.1$	8.67	7.75	8.28	$7.71 \pm 0.59$
$L_2-N_4$	$11.3 \pm 0.1$		10.8	11.4	$9.63 \pm 0.75$
$L_2-O_1$	$30.7 \pm 3.2$		9.5		
$L_2-O_4$	$8.4 \pm 0.2$		8.05		
$L_3-M_4$	$8.6 \pm 0.1$	8.39	8.5		$7.72 \pm 0.60$
$L_3-M_5$	$8.5 \pm 0.1$	8.38	8.1	8.57	$7.72 \pm 0.60$
$L_3-N_1$	$15.6 \pm 1.8$		16.3		$14.0 \pm 1.0$
$L_3-N_4$	$9.9 \pm 0.7$		11		$9.64 \pm 0.75$
$L_3-N_5$	$9.8 \pm 0.3$	11.4	10.3	11.4	$9.44 \pm 0.75$

Theory) calculations. The energies of the  $L_2-O_1$  and  $L_2-O_4$  transitions being not quoted in [26], the values given in a former compilation of x-ray energies by Bearden [35] were used for the comparison of these two transitions. As for the transition widths, only the errors originating from the fitting procedure were considered in the uncertainties quoted for the present results. As shown, most present results are consistent with the experimental energies reported in [26] within the combined errors, except for three  $L_I$  transitions for which differences between 1 and 1.4 eV are observed, whereas the combined errors are smaller than 1 eV. Regarding the comparison with Bearden's values, the energies of the  $L_2-O_1$  are in agreement but not those of the  $L_2-O_4$  transition. In this case, the deviation is about two times bigger than the sum of the two individual errors. Due to the bigger uncertainties characterizing the theoretical values reported in [26], a good agreement is observed for all transitions, except for the  $L_2-N_4$  and  $L_3-N_5$  ones. It seems that the energies of these two transitions are somewhat overestimated by the MBPT calculations

TABLE VII: Comparison of the Au L x-ray line energies obtained in this work with the experimental and theoretical values reported in [26].

Transition	Energy [eV]		
	Present work	Ref. [26]	Ref. [26]
$L_1-M_2$	$11204.25 \pm 0.30$	$11204.81 \pm 0.45$	$11204.8 \pm 3.0$
$L_1-M_3$	$11609.27 \pm 0.20$	$11610.50 \pm 0.14$	$11610.5 \pm 3.2$
$L_1-N_2$	$13710.89 \pm 0.10$	$13709.70 \pm 0.67$	$13710.0 \pm 4.6$
$L_1-N_3$	$13807.68 \pm 0.07$	$13809.10 \pm 0.11$	$13805.4 \pm 2.0$
$L_2-M_4$	$11442.37 \pm 0.01$	$11442.45 \pm 0.47$	$11442.0 \pm 1.4$
$L_2-N_4$	$13381.25 \pm 0.01$	$13381.79 \pm 0.64$	$13377.9 \pm 2.6$
$L_2-O_1$	$13624.62 \pm 1.02$	$13626.0 \pm 0.75^a)$	
$L_2-O_4$	$13728.86 \pm 0.05$	$13730.4 \pm 0.46^a)$	
$L_3-M_4$	$9628.07 \pm 0.04$	$9628.05 \pm 0.33$	$9628.1 \pm 1.3$
$L_3-M_5$	$9713.37 \pm 0.01$	$9713.44 \pm 0.34$	$9713.3 \pm 1.2$
$L_3-N_1$	$11158.75 \pm 0.50$	$11160.33 \pm 0.45$	$11156.4 \pm 3.3$
$L_3-N_4$	$11566.75 \pm 0.10$	$11566.81 \pm 0.80$	$11564.0 \pm 2.5$
$L_3-N_5$	$11584.97 \pm 0.01$	$11584.75 \pm 0.48$	$11582.12 \pm 0.57$

<sup>a)</sup> These two experimental values were taken from Ref. [35].

since similar differences of approximately 2.5 eV are also found with the experimental values reported in [26].

#### *4.4.2 Determination of the mass attenuation coefficient of molybdenum around the K-absorption edge*

X-ray Absorption Spectroscopy (XAS) measurements represent a powerful tool to characterize the atomic environment (number and species of neighbor atoms) of solid, liquid and gaseous samples. Different techniques such as EXAFS (Extended X-ray Absorption Fine Structure) and XANES (X-ray Absorption Near Edge Structure) have been developed and represent now routine works at synchrotron radiation facilities [36]. In all techniques, the absorber, i.e., the sample to be analyzed, is irradiated with a monochromatic x-ray beam whose energy is changed step by step across an absorption edge. Two modes of operation are possible. In the transmission mode (thin absorbers), the intensity of the beam measured after the sample with a photodiode is compared to the intensity of the incoming beam. From the difference, the intensity that has been absorbed in the sample can be deduced. In the fluorescence mode (thick absorbers) the sample x-ray fluorescence emission is measured with a semiconductor detector. The intensity of the fluorescence signal being proportional to the absorption coefficient of the sample, results similar to those obtained in the transmission mode can be obtained.

In this project, we have probed the possibility to use the DuMond spectrometer for in-house EXAFS measurements, using the x-ray tube to produce the continuous energy x-ray beam and the crystal of the spectrometer to monochromatize the bremsstrahlung photons and tune their energy across the chosen absorption edge. For these measurements, the direct geometry setup was employed. The absorber can be positioned either between the slit and the crystal or between the crystal and the detector. In the first case the “white bremsstrahlung beam” transmitted through the sample is analyzed with respect to its energy by the crystal. In the second case, the absorption by the sample of the beam monochromatized beforehand by the crystal is measured as a function of the energy [37]. Both techniques were checked and almost identical results were found. However, as in the first geometry the absorber can be fixed directly on the slit, which permits to use absorbers with much smaller dimensions than in the second geometry, we have opted for the first

solution.

The measurements were performed with an absorber consisting of a  $\sim 20 \mu\text{m}$  thick metallic foil of molybdenum. The absorption spectrum was observed around the  $K$ -edge which lies for Mo at  $20000.5 \pm 2.1 \text{ eV}$  [26]. The bremsstrahlung intensity increasing with the squared atomic number of the anode material, an x-ray tube with a gold ( $Z = 79$ ) anode was employed. Furthermore, as the Bragg angle corresponding to 20 keV photons diffracted in first order is the same as the one corresponding to 40 keV photons diffracted in second order or 60 keV photons diffracted in third order, a high-voltage of 40 kV was chosen for the x-ray tube so that the x-ray beam diffracted by the crystal was really monochromatic without any upper harmonics. On the other hand, to get a strong enough bremsstrahlung intensity, this relatively small value of the high-voltage was compensated by using an electron current of 50 mA. Finally, high-resolution being needed to resolve the fine structures of the absorption spectrum, a slit width of 0.10 mm was chosen.

At first, the angular spectrum around the Bragg angle corresponding to the  $K$  absorption edge of Mo was scanned without absorber. Then, the same measurement was repeated, but this time with the Mo foil fixed on the slit. Both scans consisted of 250 points with acquisition times of 20 sec. per point in the first measurement and 200 sec. in the second one. The measurement with the absorber was performed on both sides of reflection for the energy calibration of the spectrometer. The measurements with and without absorber are depicted in Fig. 33.

The Mo mass attenuation coefficient  $\mu(E)$  could be derived from the intensities measured in the two scans, using the following relation:

$$\mu(E) = \frac{-\ln\left[\frac{I(E)}{I(E_0)}\right]}{h} = \frac{\ln[I_0(E)] - \ln[I(E)]}{h}, \quad (29)$$

where  $I(E)$  and  $I_0(E)$  stand for the intensities normalized to the same acquisition time and measured with and without absorber and  $h$  represents the absorber thickness. The latter was determined accurately by weighing the 1.9 cm high  $\times$  0.6 cm wide Mo foil. A weight of 21.1 mg was obtained corresponding to an effective thickness of  $18.50 \text{ mg/cm}^2$  or, using the density of Mo ( $10.22 \text{ g/cm}^3$ ), of  $18.1 \mu\text{m}$ . The intensity  $I_0(E)$  was approximated



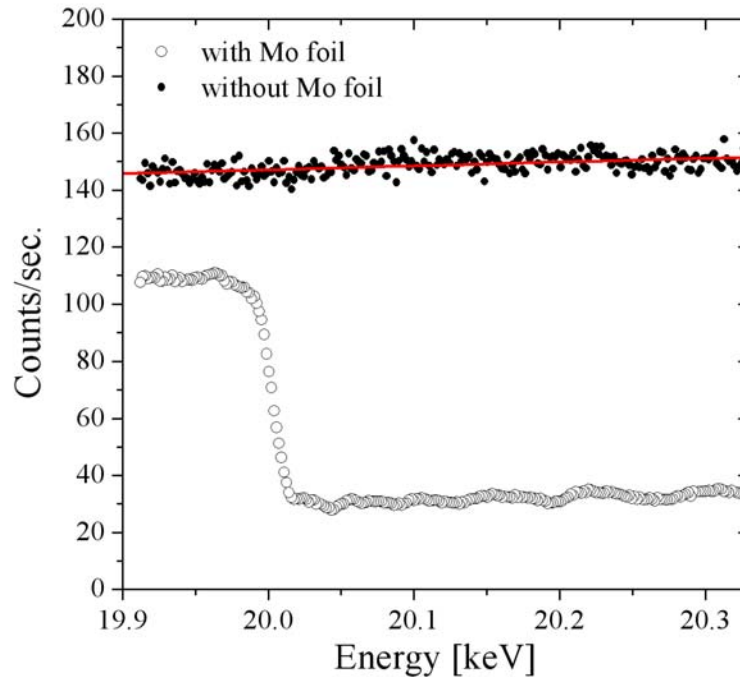


FIGURE 33: Absorption spectra of Mo around the  $K$ -edge with (data on the bottom) and without absorber (data on the top). The data were collected with the DuMond spectrometer operated in direct geometry. The red solid line represents the linear fit to the data taken without absorber. The bigger straggling of the latter are due to the shorter acquisition time.

by fitting a linear function to the experimental points (red line in Fig. 33).

The x-ray mass attenuation coefficients  $\mu(E)$  obtained in the present work are presented in Fig. 34 as a function of the photon energy. For comparison the values taken from the database XCOM [38] and those obtained by de Jonge et al. [39] in a synchrotron radiation-based experiment are also shown. In the three sets of data, a sudden increase of the absorption coefficient is observed around 20 keV. This abrupt increase, named  $K$ -edge, corresponds to the opening of the  $K$ -shell photoionization channel which is energetically forbidden for photons having a smaller energy than the binding energy of the  $K$ -shell electrons but allowed for photon energies equal or just above this threshold. The oscillations observed above the edge correspond to XANES and EXAFS structures. They are due to the scattering of the photoelectrons by neighboring atoms. The small dip observed below the edge, at about 19.96 keV, corresponds to the  $K\beta_2$  x-ray line ( $K-N_{2,3}$  transition) of Mo. This fluorescence line is produced in the absorber by the bremsstrahlung

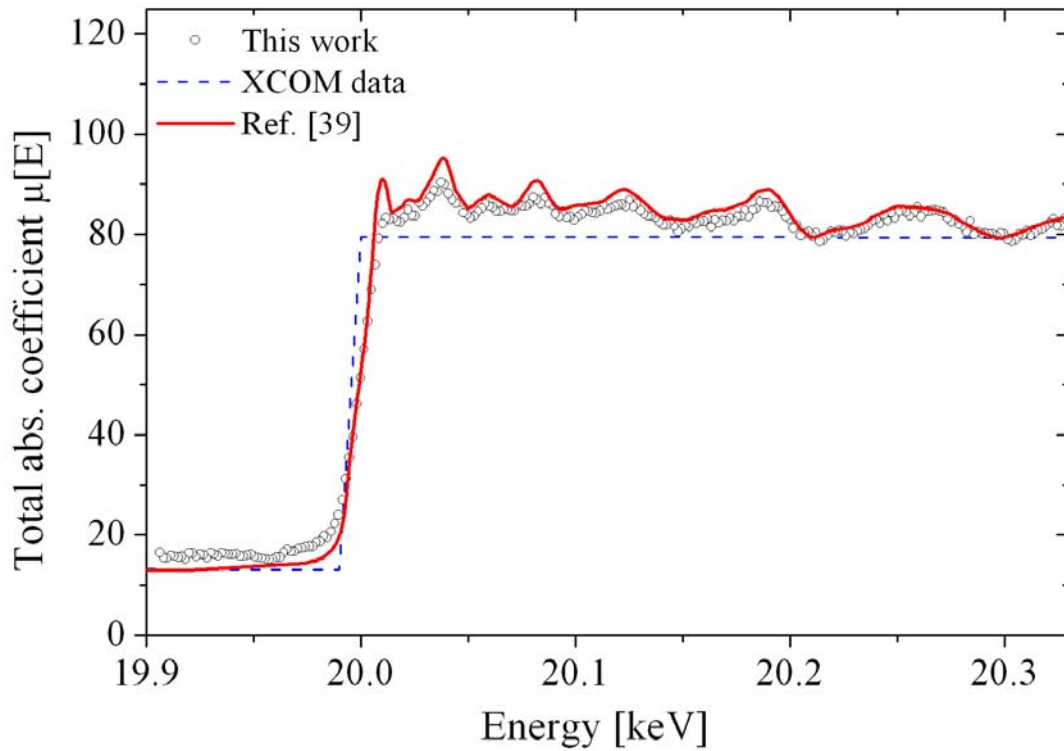


FIGURE 34: Total mass attenuation coefficient of Mo around the K-edge in  $[\text{cm}^2/\text{g}]$ . Present data are represented by open circles. For comparison the semi-experimental attenuation coefficients from the XCOM database (blue dotted line) and the ones obtained in a SR-based experiment (red solid line) are also shown.

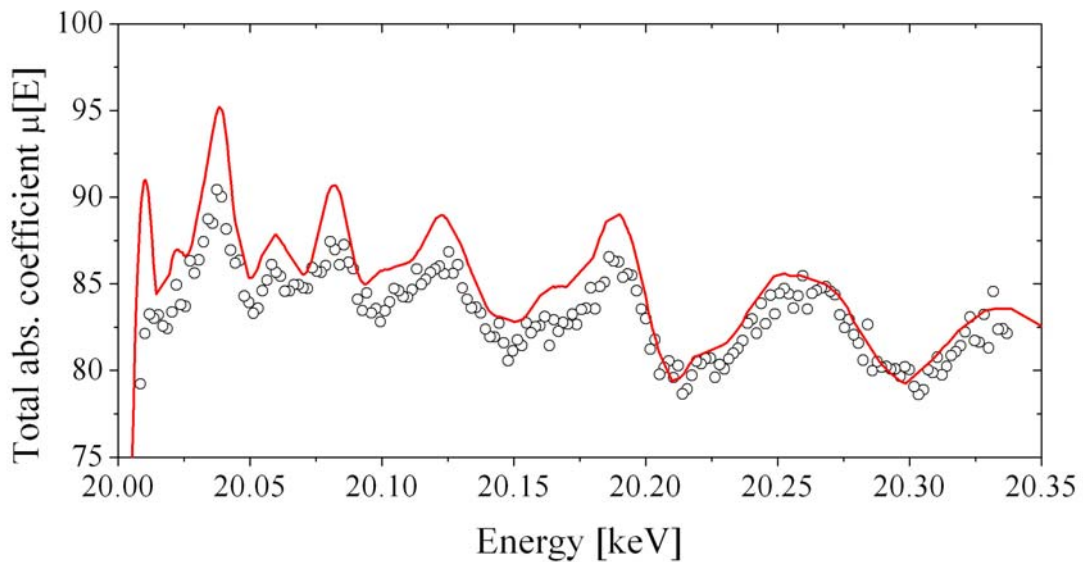


FIGURE 35: Enlarged view of the measured mass attenuation coefficients in the XANES and XAFS regions (open circles). For comparison the data from Ref [39] are also shown (red solid line).

photons which have an energy higher than 20 keV. As the width of the fluorescence source and its location are the same as the ones of the slit, the  $K\beta_2$  x-rays are diffracted by the crystal at the Bragg angle corresponding to their energy (19.96527(95) keV [26]). This increases a little bit the intensity  $I(E)$  around  $E = E(K\beta_2)$ , and this increase of the intensity  $I(E)$  is interpreted by the analysis as a tiny, artificial, diminution of the absorption coefficient  $\mu(E)$ , which explains the small dip observed in Fig. 34. Note that this dip would not be observed if the absorber were placed between the crystal and the detector as in XAS measurements performed at synchrotron radiation facilities. Actually, this explains why there is no dip in the data of Ref. [39].

In general, as shown in Fig. 34, our results for the absorption coefficient  $\mu(E)$  are in good agreement with the semi-experimental XCOM data and with the SR data from [39]. XCOM data correspond to so-called “atom-like” absorption coefficients, i.e., absorption coefficients for free and isolated atoms. It is therefore natural that they do not exhibit any XANES or XAFS structure. A more detailed comparison between the XANES/XAFS regions measured in this work and in [39] is presented in Fig. 35, where a

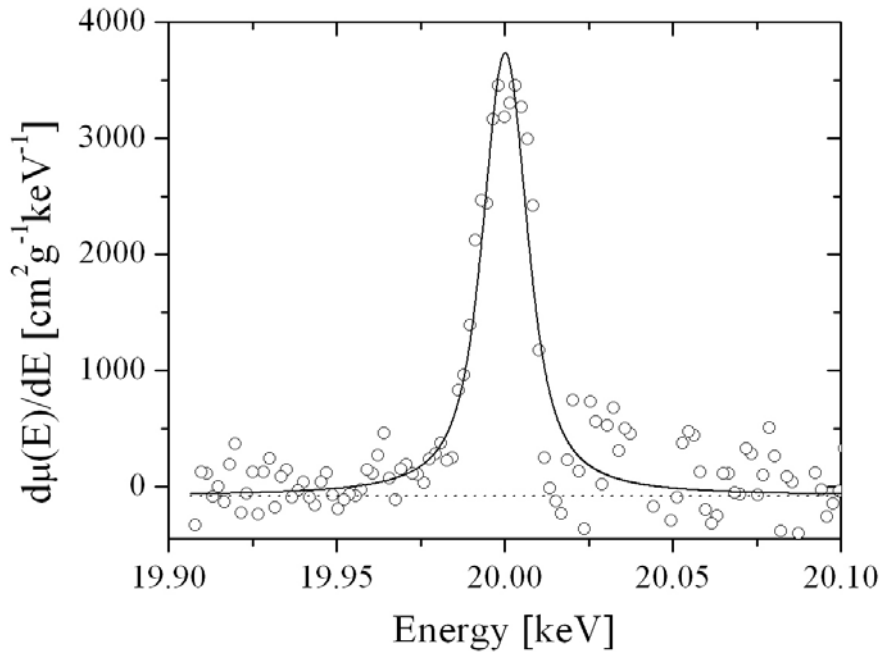


FIGURE 36: Voigt profile (black solid line) obtained from the fit of the 1<sup>st</sup> derivative of the experimental absorption function  $\mu(E)$ .

very good agreement is observed between the two data sets. The small difference in intensity can be explained by the natural oxidation of our sample and by inhomogeneities in the target thickness.

Absorption edge measurements offer the possibility to determine the binding energy of the atomic level corresponding to the measured edge. The binding energy is indeed equal to the energy associated to the first inflection point of the absorption curve. This point, located approximately in the middle of the abrupt increase of the curve, can be determined accurately by fitting the peak corresponding to the 1<sup>st</sup> derivative of the function  $\mu(E)$ . The centroid energy of the peak provided by the fit gives then the binding energy. This method was applied to our absorption measurement to determine the binding energy of the  $1s$  level of Mo. The Voigt function used to fit the points corresponding to the derivative of the absorption function  $\mu(E)$  determined in the present work is shown in Fig. 36. From the fit a result of  $20000.18 \pm 0.36$  eV was found, in very good agreement with the value of  $20000.351 \pm 0.020$  eV reported in [26].

## 5. Conclusion

In the first part of this work, the high-resolution Laue-type DuMond curved crystal spectrometer of Fribourg was presented in details. In particular, the new LabVIEW-based program developed within this thesis to control the spectrometer and acquire the data was described.

The dependence of the angular spectrometer resolution as a function of the focusing distance and slit width was investigated. The resolution was then determined by means of three different methods. Consistent results were obtained. The two last methods which are self-consistent were developed within the present work. They were found to be significantly more precise than the standard method.

The spectrometer sensitivity was demonstrated with the measurement of the very weak Gd  $K\alpha_3$  x-ray line (forbidden  $2s_{1/2} \rightarrow 1s_{1/2}$  transition). The precision of the instrument was then probed via the Ritz principle applied to the  $L_2-M_3$ ,  $K-L_2$  and  $K-M_3$  transitions of Au. A deviation of about  $2\sigma$  was found. The latter was tentatively explained by the overlap of the  $L_2-M_3$  diagram transition with its unresolved  $N$  x-ray satellites originating from  $L_1L_2N$  Coster-Kronig transitions.

Finally, two further projects were presented. In the first one, the energies and natural line widths of thirteen transitions belonging to the  $L$  x-ray lines series of Au were determined. In the second one, the mass attenuation coefficients of Mo were measured for energies around the  $K$ -absorption edge. XANES and EXAFS oscillations were observed in the absorption spectrum. The latter were found to agree well with former data taken using synchrotron radiation. In addition, from the absorption spectrum, a precise value for the binding energy of the  $1s$  level of Mo was obtained.



## 6. Bibliography

- [1] H.H. Johann,  
*Die Erzeugung lichtstarker Röntgenspektren mit Hilfe von Konkavenkristallen.*  
Z. Phys. **69** (1931) 185.
- [2] T. Johansson,  
*Über ein neuartiges genau fokussierendes Röntgenspektrometer.*  
Z. Phys. **82** (1935) 507.
- [3] L. von Hamos,  
*Röntgenspektroskopie und Abbildung mittels gekrümmter Kristallreflektoren.*  
Naturwissenschaften **20** (1932) 705.
- [4] L. von Hamos,  
*Röntgenspektroskopie und Abbildung mittels gekrümmter Kristallreflektoren I:  
Geometrisch–optische Betrachtungen.*  
Ann. Phys. **409** (1933) 716.
- [5] L. von Hamos,  
*Röntgenspektroskopie und Abbildung mittels gekrümmter Kristallreflektoren II:  
Beschreibung eines fokussierenden Spektrographen mit punktgetreuer  
Spaltabbildung.*  
Ann. Phys. **411** (1934) 252.
- [6] Jesse W.M. DuMond,  
*A high resolving power curved–crystal focusing spectrometer for short wave–length  
x–rays and gamma–rays.*  
Rev. Sci. Instr. **18** (1947) 626.

- [7] Y. Cauchois,  
*Spectrographie des rayons X par transmission d'un faisceau non-canalisé à travers un cristal courbé.*  
J. Phys. Radium **3** (1932) 320.
- [8] N. Ryde and B. Andersson,  
*A precision curved crystal gamma-ray spectrometer".*  
Proc. Phys. Soc. **B68** (1955) 1117.
- [9] O. Beckman, P. Bergvall, B. Axelsson,  
*A precision curved crystal x-ray and gamma-ray spectrometer.*  
Ark. Fysik **14** (1959) 419.
- [10] K.M. Crowe and R.E. Shafer,  
*7.7 m bent crystal spectrometer at the 184 Inch Cyclotron.*  
Rev. Sci. Instr. **38** (1967) 1.
- [11] O. Piller, W. Beer and J. Kern,  
*Das fokussierende kristallspektrometer der universität Fribourg.*  
Nucl. Instr. and Meth. **107** (1973) 61.
- [12] G.L. Borchert, W. Scheck, O.W.B. Schult,  
*Curved crystal spectrometer for precise energy measurements of gamma rays from 30 to 1500 keV.*  
Nucl. Instr. and Meth. **124** (1975) 107.
- [13] G.L. Borchert, P.G. Hansen, B. Johnson, H.L. Ravn, O.W.B. Schult and P. Tidemand-Petersson,  
*Curved crystal spectrometer for measurements of smaller K x-ray energy shifts.*  
Nucl. Instr. and Meth. **178** (1980) 209.



- [14] H.R. Koch, H.G. Börner, J.A. Pinston, W.F. Davidson, J. Faudou, R. Roussille and O. W.B. Schult,  
*The curved crystal gamma ray spectrometers "GAMS 1, GAMS 2, GAMS 3 for high resolution ( $n, \gamma$ ) measurements at the high flux reactor in Grenoble.*  
Nucl. Instr. and Meth. **175** (1980) 401.
- [15] W. Beer, K. Bos, G. De Chambrier, K.L. Giovanetti, P.F.A. Goudsmit, B.V. Grigoryev, B. Jeckelmann, L. Knecht, L.N. Kondurova, J. Langhans, H.J. Leisi, P.M. Levchenko, V.I. Marushenko, A.F. Mezentsev, H. Obermeier, A.A. Petrunin, U. Rohrer, A.G. Sergeev, S.G. Skornjakov, A.I. Smirnov, E. Steiner, G. Strassner, V.M. Suvorov and A. Vacchi,  
*Crystal spectrometer for measurements of pionic x-rays.*  
Nucl. Instr. and Meth. **238** (1985) 365.
- [16] B. Perny, J.-Cl. Dousse, M. Gasser, J. Kern, R. Lanners, Ch. Rhône and W. Schwitz,  
*DuMond curved crystal spectrometer for in-beam x-ray and gamma-ray spectroscopy.*  
Nucl. Instr. and Meth. in Physics Research Sect. A **267** (1988) 120.
- [17] L.V. Azaroff,  
*Elements of X-Ray Crystallography.*  
McGraw-Hill Book Company, New York, 1968.
- [18] M. Sanchez del Rio,  
*X-ray Oriented Programs (XOP).*  
<http://www.esrf.fr/computing/scientific/xop/>.
- [19] Hewlett-Packard, Laser Position Transducer System, Model 5526A.  
Technical specifications.

- [20] W. Schwitz,  
*Precision of curved crystal spectrometers I: Large angle laser interferometer.*  
Nucl. Instr. and Meth. **154** (1978) 95.
- [21] Moore Rotary Table, type 7046, Moore special tool Co., Inc. Bridgeport, Connecticut, USA.
- [22] Detector data sheet, Bicron Corp., Ohio, U.S.A.
- [23] Technical specifications of the PCI-6040 E series Multifunctional I/O card, National Instruments, Austin, USA.
- [24] National Instruments, LabVIEW Help, August 2005, 371361A-01.
- [25] R. Bitter, T. Mohiuddin, M. Nawrocki,  
*LabVIEW Advanced Programming Techniques*, Second edition.
- [26] R.D. Deslattes, E.G. Kessler, Jr, P. Indelicato, L. de Billy, E. Lindroth and J. Anton,  
*X-ray transition energies: new approach to a comprehensive evaluation.*  
Rev. Mod. Phys. **75** (2003) 35.
- [27] PeakFit software, User Manual.
- [28] J.L. Campbell and T. Papp,  
*Widths of the atomic K-N<sub>7</sub> levels.*  
At. Data Nucl. Data Tables **77** (2001) 1.
- [29] B. Galley and J.-Cl. Dousse,  
*Forbidden 2s<sub>1/2</sub>-1s<sub>1/2</sub> radiative atomic transitions.*  
Phys. Rev. A **50** (1994) 3058.

- [30] J.H. Scofield,  
*Relativistic Hartree–Slater values for K and L x–ray emission rates.*  
At. Data Nucl. Data Tables **14** (1974) 121.
- [31] J.–Cl. Dousse and J. Hozowska,  
*L– and M–shell–electron shake processes following 1s photoionization in argon and krypton.*  
Phys. Rev. A **56** (1997) 4517.
- [32] H. Oohashi, T. Tochio and Y. Ito,  
*Origin of Au  $L\beta_2$  visible satellites.*  
Phys. Rev. A **68** (2003) 032506.
- [33] F.K. Richtmyer, S.W. Barnes and E. Ramberg,  
*The widths of the L–series and the energy levels of Au (79).*  
Phys. Rev. **46** (1934) 843.
- [34] J.H. Williams,  
*The natural widths of the L –series lines in the x–ray spectra of elements 74 to 83.*  
Phys. Rev. **45** (1934) 71.
- [35] J.A. Bearden,  
X–Ray Wavelengths.  
Rev. Mod. Phys. **39** (1967) 78.
- [36] D. Norman,  
*X–ray absorption spectroscopy (EXAFS and XANES) at surfaces.*  
J. Phys. C **19** (1986) 3273.

- [37] T. Ludziejewski, P. Rymuza, Z. Sujkowski, B. Boschung, J.-Cl. Dousse, B. Galley Z. Halabuka, Ch. Herren, J. Hoszowska, J. Kern, Ch. Rhême and M. Polasik, *High-resolution study of the  $K\beta_2$  x-ray spectra induced by proton and photon impact on Zr, Mo, and Pd targets.*  
Phys. Rev. **52** (1995) 2791.
- [38] <http://physics.nist.gov/PhysRefData/Xcom/Text/XCOM.html>.
- [39] M.D. de Jonge, Ch.Q. Tran, Ch.T. Chantler, Z. Barnea, B.B. Dhal, D.J. Cookson, W.-K. Lee and A. Mashayekhi, *Measurement of the x-ray mass attenuation coefficient and determination of the imaginary component of the atomic form factor of molybdenum over the 13.5–41.5 keV energy range.*  
Phys. Rev. A **71** (2005) 032702.

Part II:

Photoinduced  $K\alpha$   
hypersatellite x-ray lines of  
molybdenum



# 1. Introduction

X-ray hypersatellites are x-ray lines that are emitted by atoms with two vacancies in the same shell in the initial state.  $K\alpha$  x-ray hypersatellite lines, noted  $K\alpha^h$  in the literature, correspond therefore to the radiative decay of atoms with an empty  $K$ -shell in the initial state and one vacancy in the  $K$ -shell plus one in the  $L_3$  or  $L_2$ -subshell in the final state, i.e.,

$$K\alpha_1^h : K^{-2} \rightarrow K^{-1}L_3^{-1}, \quad (30a)$$

$$K\alpha_2^h : K^{-2} \rightarrow K^{-1}L_2^{-1}, \quad (30b)$$

Due to the presence of an additional vacancy, named spectator vacancy, in the initial and final states and the resulting change of the electron screening, satellite x-ray lines are shifted to higher energies with respect to their parent diagram lines. As mentioned before, the energy shift decreases with the principal quantum number of the spectator vacancy. For instance, for atoms with  $Z \sim 50$ , the energy shifts of  $K\alpha$  x-rays are  $\sim 500$  eV,  $\sim 50$  eV and  $\sim 5$  eV when the spectator vacancy is located in the  $K$ ,  $L$  and  $M$ -shell, respectively. Thus, for  $K\alpha$  x-rays the shift is clearly the highest when the spectator vacancy is located in the  $K$ -shell. For this reason, these “super” satellite lines have been called hypersatellites.

$K\alpha^h$  and to a smaller extent  $K\beta^h$  ( $K^{-2} \rightarrow K^{-1}M_{2,3}^{-1}$  transition) hypersatellites have been studied experimentally for a variety of elements ranging from neon ( $Z = 10$ ) to thallium ( $Z = 81$ ) [1–11]. Most hypersatellite measurements were performed by means of high-resolution x-ray spectroscopy, using crystal spectrometers. In principle, for mid- $Z$  elements, the energy shifts of the hypersatellites are sufficiently large to resolve them from their parent diagram lines with a good Si(Li) detector. However, due to the Lorentzian shapes of the transitions which enhance the tails of the detector response and the poor intensity of the hypersatellite lines, accurate and reliable information about the yields and energies of hypersatellites is difficult to extract from low-resolution measurements. An alternative to the high-resolution spectroscopy method is offered by the so-called satellite-hypersatellite coincidence technique [12]. In this technique, the two photons emitted as a result of the hypersatellite-satellite cascade  $K^{-2} \rightarrow K^{-1}L^{-1} \rightarrow L^{-2}$  are measured

in coincidence by two Si(Li) detectors placed close to the target.

Hypersatellites are interesting in many aspects for studying atomic systems. At first they permit to probe in a detailed way the goodness of theoretical calculations concerning the atomic structure. In particular, they are more sensitive than the diagram lines to relativistic and QED effects such as the transverse Breit interaction [13]. Precise measurements of their energies provide thus stringent tests of MCDF (Multi-configuration Dirac-Fock) and MBPT (Many Body Perturbation Theory) calculations concerning the energies of the atomic levels in multiply ionized atoms. The natural line widths of hypersatellite lines, which are expected to be larger than those of the corresponding diagram lines, permit to determine the widths of double  $K$ -hole excited states [14]. In the LS coupling scheme which prevails for light elements, the  $K\alpha_1^h$  hypersatellite is strictly forbidden by the electric-dipole selection rules. In the  $j$ - $j$  coupling, which applies to heavy elements, this transition is, however, allowed. Between these two extreme cases, i.e., for mid-heavy elements for which the relevant coupling is the intermediate one, the  $K\alpha_1^h$  hypersatellite is not forbidden but only hindered by the selection rules. For these reasons, the  $K\alpha_1^h / K\alpha_2^h$  intensity ratio varies smoothly as a function of the atomic number  $Z$  from zero for light elements to two for heavy elements. Thus, measurements of this ratio for mid-heavy elements provide useful information about the coupling scheme of the latter. Furthermore, as the two vacancies in the initial state belong to the same shell, hypersatellites provide important information about electron correlations in atoms [15]. Last but not least, from the  $K\alpha^h/K\alpha$  hypersatellite-to-diagram line yield ratios, the double  $K$ -shell ionization cross sections  $\sigma_{KK}$  can be determined.

$K$  hypersatellite x-rays can be produced by impact with heavy and light ions, electrons and photons. All these particles can produce double  $1s$  vacancy states in the target atoms but the double ionization cross sections vary by several orders of magnitude. They are large for heavy ions and very small for photons. For charged particle impact, the double ionization probability is proportional to the squared single ionization probability. As a result, in collisions involving heavy ions, the single ionization probability is so high that the probability for a double ionization is still quite large. Unfortunately, the probability for a simultaneous multiple ionization in the outer shells is also high. This



leads to very complex x-ray spectra containing numerous overlapping satellite lines, from which it is then difficult to extract the x-ray hypersatellites. For electrons, one faces the opposite situation. The probability for a single ionization is quite low so that the probability for a double ionization is very small but, in counterpart, the probability for a simultaneous ionization of outer-shell electrons is negligibly small.

For photons, the single ionization probability is comparable to the one of electrons but the double ionization probability is no longer proportional to the squared single probability. In photoionization, the dominant process is indeed the photo-effect in which a single photon interacts with a single electron. A direct double ionization through a single photo-effect is therefore excluded and the removal of the two  $1s$  electrons is only possible via a sequential two-step mechanism, namely a photo-effect followed by a shake or knock-out process. In the shake process [16], the  $K$  photoelectron is ejected rapidly and due to the sudden change of the central potential a subsequent excitation of a second electron to an unfilled bound state or to the continuum takes place. In the knock-out process, the outgoing photoelectron knocks out the second  $1s$  electron in an  $(e, 2e)$ -like electron collision. For mid-heavy elements, the  $K$ -shell shake and knock-out probabilities are small so that the relative intensities of photoinduced hypersatellites with respect to their parent diagram lines are only of the order of  $10^{-4}$ – $10^{-5}$ . As a consequence, by now high-resolution measurements of  $K$  hypersatellites of mid-heavy elements are extremely scarce and existing data have been only obtained using intense synchrotron radiation beams for the production of the target fluorescence.

In the present work, we have probed the possibility to measure  $K\alpha$  hypersatellites of mid- $Z$  elements using the bremsstrahlung of an x-ray tube to make the samples fluorescing. This project represented a very challenging experimental task because the bremsstrahlung intensity of an x-ray tube is lower to a large extent than that of synchrotron radiation and because the background is increased by a factor of 2–3 by the elastic scattering in the target of the bremsstrahlung from the x-ray tube. In addition, at synchrotron radiation facilities, monochromatic and energy tunable beams are available. The energy tunability permits to adjust the beam energy to the value corresponding to the maximum double photoionization cross section, whereas the monochromatic character of the photons employed to produce the hypersatellites simplifies grandly the interpretation

of the results. On the other hand, experiments carried out at SR facilities are limited in time (typically one week), which is not the case in in-house experiments performed with x-ray tubes. The main reason, however, for performing this hypersatellite project with an x-ray tube resided in the fact that hypersatellites of mid-heavy elements can only be measured with Laue-type crystal spectrometers, the energy of the transitions of interest being too high for Bragg-type spectrometers. Unfortunately, the larger sizes of Laue-type crystal spectrometers do not permit their installation at SR beam-lines, at least for instruments using crystals with radius of curvature of several meters like the DuMond spectrometer of Fribourg.

Despite the above-mentioned difficulties, the project could be finally realized successfully with a molybdenum sample ( $Z = 42$ ) and a gold anode x-ray tube. Thanks to an optimization of the experimental set-up and a very long data acquisition, the extremely weak  $K\alpha_{1,2}^h$  hypersatellite x-ray lines of Mo could be extracted from the background fluctuations and their energy, natural line width and relative intensity determined.

## 2. Experimental method and measurements

As the high-resolution DuMond curved crystal spectrometer has been described in details in the first part of the present thesis work, only the features specific to the experimental setup employed for the measurements of the Mo  $K\alpha^h$  x-ray hypersatellites will be presented below.

The spectrometer was operated in the slit geometry. A slit width of 0.10 mm was chosen leading in 1<sup>st</sup> diffraction order to a FWHM energy resolution of the spectrometer of 6.45 eV for the  $K\alpha_{1,2}$  diagram lines and of 6.81 eV for the  $K\alpha_{1,2}^h$  hypersatellites. The target consisted of a 54 mg/cm<sup>2</sup> thick metallic foil of Mo placed 27.5 mm behind the slit and tilted by 11.25 deg. with respect to the target-crystal direction. For this angle, the maximum  $K\alpha$  fluorescence intensity was indeed observed. The measurements were performed in first order of diffraction corresponding to Bragg angles of 8.3 and 8.1 deg. for the diagram and hypersatellite lines, respectively. The Mo foil was irradiated with the bremsstrahlung produced by a water cooled Coolidge-type Au anode x-ray tube whose x-ray exit window consisted of a 1 mm thick beryllium foil. The tube was operated at 90 kV and 30 mA and oriented so that the axis of the conical x-ray beam was perpendicular to the target-crystal direction. The distance between the x-ray tube and the target was 45 mm. The target chamber was pumped down to about 1 mbar. For the diffraction of the x-rays the (110) planes of a 10 cm high  $\times$  10 cm wide  $\times$  0.5 mm thick quartz crystal plate were used. The quartz lamina was bent cylindrically to a radius of 315 cm. The effective reflecting area of the crystal was 12 cm<sup>2</sup>. For the detections of the x-ray the Phoswich scintillator detector was employed.

The measurements were performed in two steps. In the first step the region of the  $K\alpha_1$  and  $K\alpha_2$  diagram lines was measured with a focusing distance equal to the average focusing distance of the two lines. The spectrum was observed on both sides of reflection in order to determine the zero Bragg angle required for the energy calibration of the spectrometer. The spectrum measured on the right side was used later on to determine the  $K\alpha_1$  and  $K\alpha_2$  line shapes whose precise knowledge was crucial for a correct analysis of the weak hypersatellites. In the second step, the angular range corresponding to the region of the  $K\alpha_{1,2}^h$  hypersatellites was measured on the right side of reflection in 87 successive

step by step scans. The same focusing distance as the one used for the diagram line was employed. For the hypersatellite measurements the crystal was thus defocused by about 1.7 mm. This small defocusing value, however, did not affect the precision of the measurements, the corresponding loss of resolution being negligibly small (see Fig. 23). Each scan contained 200 equidistant points and the acquisition time per point was 200 sec. In order to control the instrumental reproducibility and the stability of the x-ray tube intensity, a short measurement (30 sec. per point) of the  $K\alpha_{1,2}$  x-ray lines was performed between each fourth scan. However, as shown later on by the data analysis, the relative intensity fluctuations of the  $K\alpha_1$  and  $K\alpha_2$  lines were found to be smaller than 0.2% and the straggling of the centroid positions smaller than 0.2 eV for the  $K\alpha_1$  line and smaller than 0.5 eV for the  $K\alpha_2$  one. For this reason, the  $K\alpha^h$  hypersatellite scans were simply added together without any further corrections.

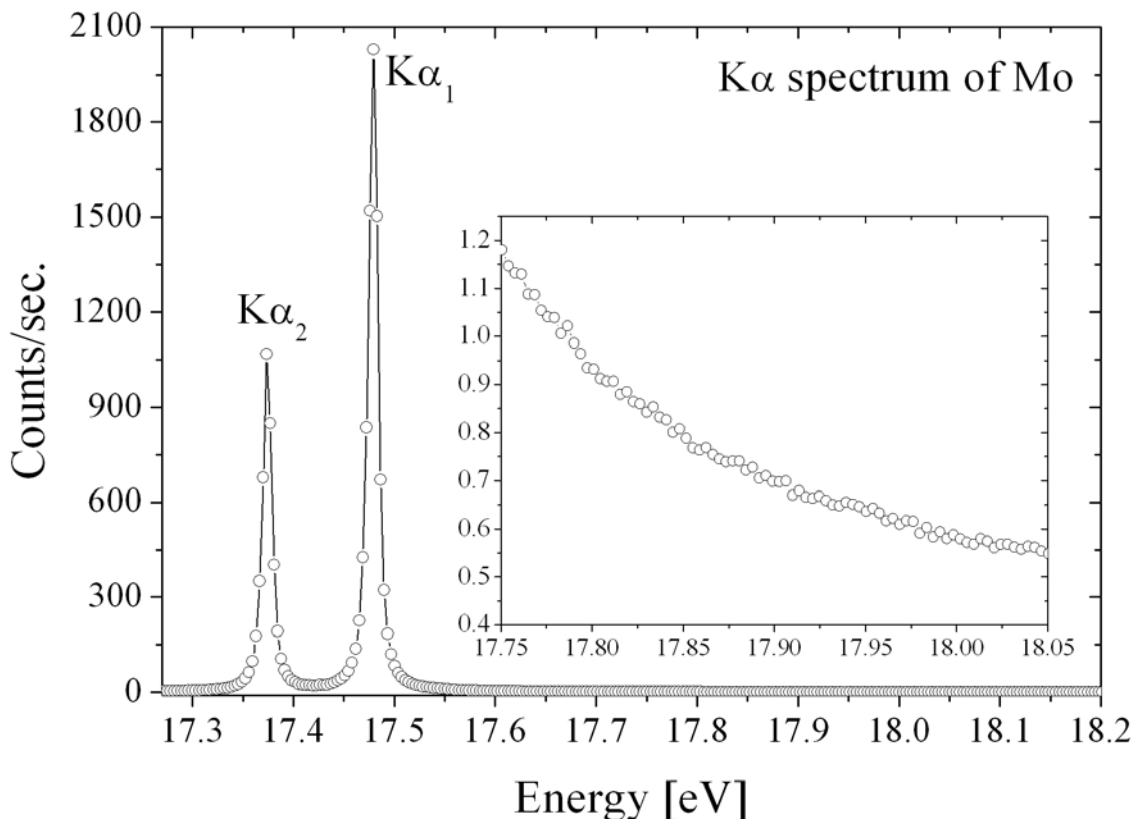


FIGURE 37:  $K\alpha$  x-ray spectrum of molybdenum induced by photoionization using the Au x-ray tube. The inset shows the hypersatellite energy region (enlarged scale).

For illustration, the  $K\alpha_{1,2} + K\alpha_{1,2}^h$  x-ray spectrum is represented in Fig. 37. The energy region corresponding to the  $K\alpha^h$  hypersatellites is shown enlarged in the inset. As it can be seen, the results of this first attempt are rather disappointing since no hypersatellite can be distinguished, although the data were collected during about 5 h per point. Actually, simulations performed afterwards have shown that the measured spectrum is correct and that the expected hypersatellite intensities are indeed smaller than the background fluctuations. It was concluded that additional efforts had to be done to lower the background. In the hypersatellite region, the background is due to the elastic scattering by the target of the x-ray tube bremsstrahlung, the Lorentzian tail of the  $K\alpha_1$  line and, to a smaller extent, the tail of the  $K\alpha_2$  line. The bremsstrahlung-induced background component consists of photons that have the same energy as the one corresponding to the hypersatellite x-rays, the same geometrical origin, the target, and both react similarly to the high-voltage and current of the x-ray tube. However, as bremsstrahlung photons contributing to the production of the hypersatellites should have an energy higher than the threshold energy for a double ionization of Mo, i.e. about 40.6 keV, by inserting an appropriate absorber between the x-ray tube and the target one can diminish the intensity of the bremsstrahlung photons contributing to the background in the hypersatellite region and only moderately the intensity of the bremsstrahlung photons that contribute to the production of the hypersatellites. The absorber which satisfies the best these conditions corresponds to an element whose  $K$ -edge lies just below the hypersatellite energies. As the Mo hypersatellite energies are about 17.8 keV for the  $K\alpha_2^h$  and 17.9 keV for the  $K\alpha_1^h$ , the most appropriate absorber is yttrium ( $Z = 39$ ) whose  $K$ -edge lies at 17.038 keV. The same idea can be used to reduce the background originating from the tails of the  $K\alpha_1$  and  $K\alpha_2$  lines. In this case, the hypersatellite-to-diagram line intensity ratio should be increased by using an absorber which diminishes markedly the intensities of the diagram lines and significantly less those of the hypersatellites. As the single ionization cross section is the highest just above the  $K$ -edge which is equal to 20.0 keV for molybdenum, an absorber with the  $K$ -edge below this energy but as close as possible to it should be chosen. In this case, the best absorber is niobium ( $Z = 41$ ) whose edge lies at 18.986 keV. Note that, as above the  $K$ -edge the absorption decreases with the energy, the bremsstrahlung photons

contributing to the production of the hypersatellites are less absorbed, as desired. Finally, an absorber consisting of a 50  $\mu\text{m}$  thick Nb foil followed by a 25  $\mu\text{m}$  thick Y foil was chosen and fixed on the nose of the x-ray tube, in front of the Be window.

The efficiency of a Coolidge x-ray tube is given approximately by the following empirical formula [17]:

$$\eta[\%] = \frac{P_{x\text{-ray}}}{P_{el}} = 1.4 \cdot 10^{-6} \cdot Z \cdot HV[kV], \quad (31)$$

where  $P_{x\text{-ray}}$  represents the power of the emitted x-rays and  $P_{el}$  the electron energy absorbed in the anode,  $HV$  represents the high-voltage of the x-ray tube and  $Z$  stands for the atomic number of the anode material. In our case  $Z = 79$  and  $HV = 90$  kV so that the efficiency was about 1%. From Eq. (31) one can obtain the power of the emitted x-rays:

$$P_{x\text{-ray}}[W] = 1.4 \cdot 10^{-6} \cdot Z \cdot HV^2[kV] \cdot I[mA], \quad (32)$$

where  $I$  is the electron current in the x-ray tube. One sees that the x-ray power varies linearly with the electron current and quadratically with the high-voltage. For a given tube power, a larger x-ray power can thus be obtained by using a higher voltage and a smaller current. This is one of the reasons for which a high-voltage of 90 kV and a current of 30 mA were chosen for this project. The radiation emitted by the x-ray tube consists of the bremsstrahlung, whose spectrum is continuous, and of discrete characteristic x-ray lines. However, the intensity of the characteristic emission was found to represent less than 1% of the total x-ray intensity and was therefore neglected in the calculations presented below.

The bremsstrahlung intensity  $i$  can be calculated as a function of the photon wavelength  $\lambda$ , using the following semi-empirical formula [17]:

$$i(\lambda) = C \cdot Z \cdot \frac{I}{\lambda^2} \left( \frac{I}{\lambda_{swl}} - \frac{I}{\lambda} \right) \cdot Z + B \cdot Z^2 \cdot \frac{I}{\lambda^2}, \quad (33)$$

where  $C$  and  $B$  are constants with  $C \gg B$  and  $\lambda_{swl}$  stands for the shortest possible wavelength of the emitted x-rays. Using the relation  $\lambda = hc/E = 12.398[\text{\AA} \cdot \text{keV}]/E[\text{keV}]$  and the condition  $I(E) \cdot dE = i(\lambda) \cdot d\lambda$  the following expression is obtained for the

intensity  $I(E)$  of the x-ray tube as a function of the photon energy:

$$I(E) = i \left( \frac{12.398 [\text{\AA} \cdot \text{keV}]}{E [\text{keV}]} \right) \cdot \frac{12.398 [\text{\AA} \cdot \text{keV}]}{(E [\text{keV}])^2}. \quad (34)$$

To take into account the absorption of the x-rays in the Be exit window of the x-ray tube, the relation (34) should be modified as follows:

$$I(E) \rightarrow I_1(E) = I(E) \cdot \exp[-\mu_{Be}(E) \cdot h_{Be}] \quad (35)$$

where  $\mu_{Be}(E)$  stands for the mass attenuation function of Be obtained by fitting the values tabulated in the XCOM database [18] and  $h_{Be}$  the thickness of the Be window in  $\text{g}/\text{cm}^2$ . The intensity of the bremsstrahlung impinging on the Mo target when the Nb and Y absorbers are inserted in front of the Be window can be calculated in a similar way, leading to:

$$I_2(E) = I(E) \cdot \exp[-\mu_{Be}(E) \cdot h_{Be} - \mu_{Nb}(E) \cdot h_{Nb} - \mu_Y(E) \cdot h_Y] \quad (36)$$

where  $\mu_{Nb}(E)$  and  $\mu_Y(E)$  represent the linear attenuation functions deduced from [18] for Nb and Y, respectively, and  $h_{Nb}$  and  $h_Y$  stand for the thicknesses in  $\text{g}/\text{cm}^2$  of the two foils. The bremsstrahlung intensities  $I_1(E)$  and  $I_2(E)$  received by the Mo target in the measurements performed with and without absorbers is depicted in Fig. 38. As shown, the number of the bremsstrahlung photons with  $20 \text{ keV} \leq E \leq 30 \text{ keV}$  (i.e., those for which the single ionization cross section  $\sigma_K$  is the highest) is strongly diminished by the two absorbers, whereas the number of photons with  $E \geq \sim 40 \text{ keV}$  (i.e., those contributing to the production of the hypersatellites) is only diminished by about 30%.

In view of the disappointing results obtained for the  $K\alpha^h$  hypersatellites in the first series of measurements, the latter were repeated, using, however, the Nb and Y absorbers to improve the peak-to-background conditions. In addition a small collimator was installed between the x-ray tube and the sample in order to diminish the residual background arising from the elastic and inelastic scattering of the bremsstrahlung by the walls of the target chamber. Apart this small but important changes, the setup was the same as the one employed in the first measurements. The same holds for the experimental procedure except that a longer step length was employed for the hypersatellite region so

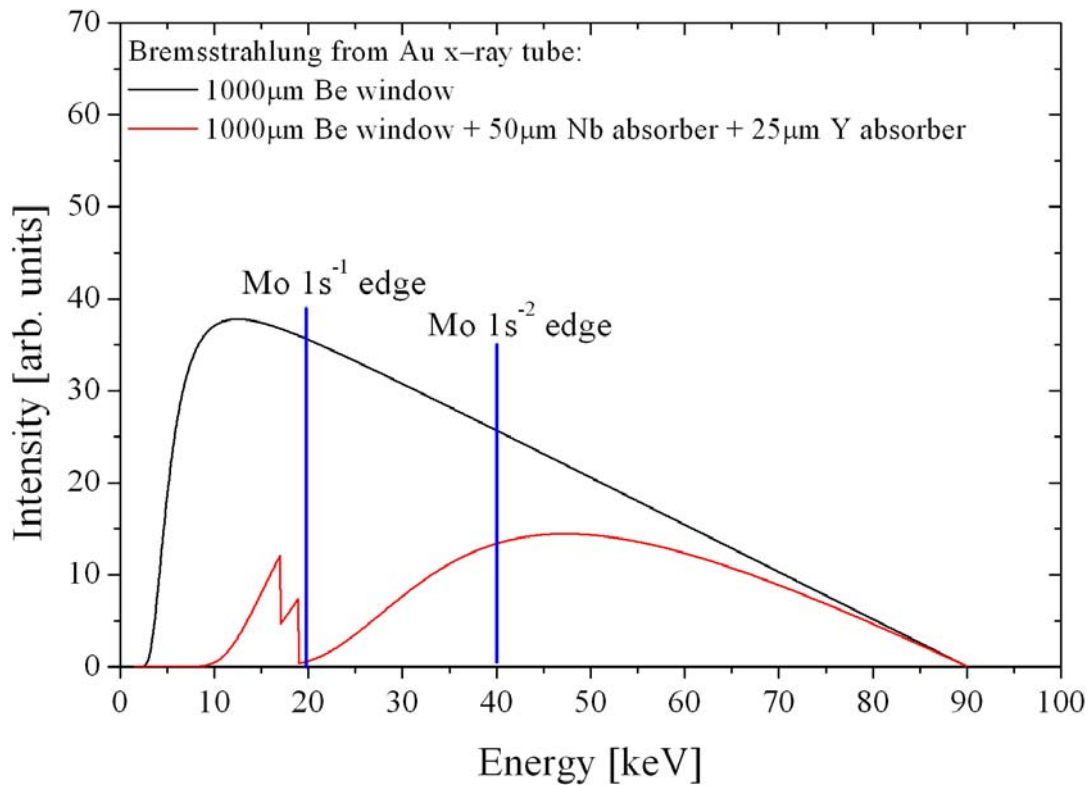


FIGURE 38: Calculated bremsstrahlung x-ray spectrum emitted by the Au x-ray tube without absorber (black solid line) and with the niobium + yttrium absorbers (red solid line). The positions of the threshold energies for a single, respectively double, K-shell ionization of Mo are indicated by the vertical blue lines.

that the number of points could be diminished from 200 to 110. In counterpart, the acquisition time per point was increased from 200 sec. to 750 sec. Furthermore, the number of scans was also increased (to 104) so that the total acquisition time per point was 78'000 sec. ( $\sim 21.7$  h) and the total duration of the new hypersatellite measurements about 100 days. Due to this very long duration of the experiment, control measurements of the  $K\alpha_{1,2}$  diagram lines were performed periodically. However, as in the first series of measurements, no significant fluctuations were observed in the intensities of the two lines, neither in their positions, so that no off-line corrections were needed and the 104 hypersatellite scans were simply added together. The  $K\alpha + K\alpha^h$  x-ray spectrum of Mo obtained in the second series of measurements is presented in Fig. 39. As it can be seen, in this case the hypersatellite lines emerge more clearly from the background fluctuations and, thanks to the absorbers, the sum of the three background components in the



hypersatellite region could be diminished by a factor of about 4.

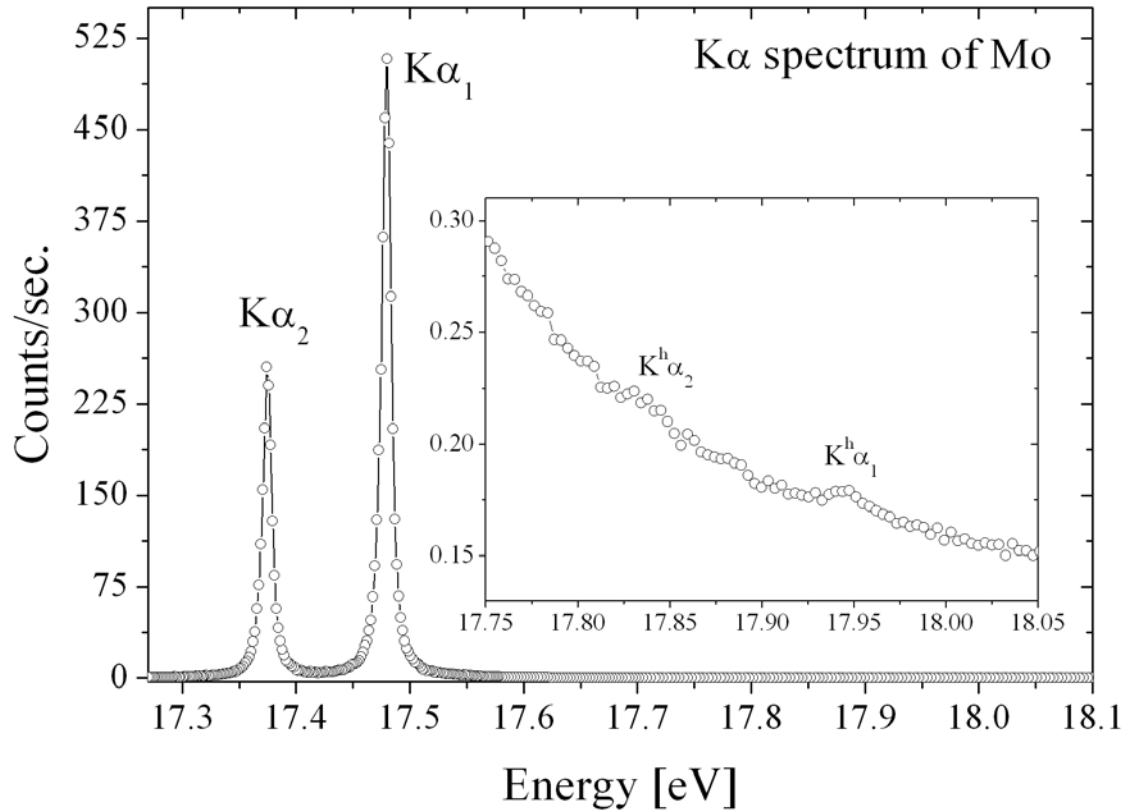


FIGURE 39: K $\alpha$  x-ray spectrum of molybdenum induced by photoionization using the Au x-ray tube and the Nb + Y absorbers. In the enlarged energy region shown in the inset, the two hypersatellites are still very weak but visible thanks to the diminution of the background obtained with the two absorbers.

### 3. Data analysis

The observed diagram and hypersatellite lines of molybdenum were analyzed by means of the least square fitting program PeakFit, employing Voigt functions to reproduce the line shapes of the four transitions. The same method of analysis was used for the two series of measurements, i.e., the measurements performed without and with the absorbers.

At first, the x-ray spectrum spanning the whole  $K\alpha_{1,2} + K\alpha_{1,2}^h$  region and calibrated beforehand in energy was fitted. The diagram lines were fitted using one Voigt function per transition, whereas the hypersatellite lines were not considered in this first stage of the analysis. In the fitting procedure, the intensities, energies and Gaussian widths of the two diagram lines as well as the two parameters of the linear background were let free while the Lorentzian widths were kept fixed at the values deduced from the tables of Campbell and Papp [19]. Although the Gaussian widths could have been calculated from the known angular resolution of the spectrometer, they were let free in the fit in order to better reproduce the tails of the two transitions in the region of the hypersatellites. However, the fit was done with the constraint that the two diagram lines should have the same Gaussian width, using the option offered by the PeakFit program to share a free fitting parameter between several lines. Actually, the value provided by the fit for the shared Gaussian width was found to be slightly different but consistent within the fit error with the calculated one. The hypersatellite region fitted with this method is shown in Fig. 40 for the measurements performed without and with absorbers.

In the second stage of the analysis, the fitted high-energy tails of the  $K\alpha_1$  and  $K\alpha_2$  diagram lines and linear background were subtracted from the experimental data points and the residuals were analyzed. The  $K\alpha^h$  x-ray hypersatellite lines were fitted with the same method as the one used for the  $K\alpha$  x-ray spectrum. However, in this case the energies, intensities and the Lorentzian widths of the hypersatellite lines were let free while the Gaussian widths was kept fixed at the values computed from the known angular instrumental resolution. A constant background was also used as free fitting parameter but the latter was found to be consistent with zero within the fit error. The fits of the residual spectra are shown in more details in Fig. 41 for both series of measurements.

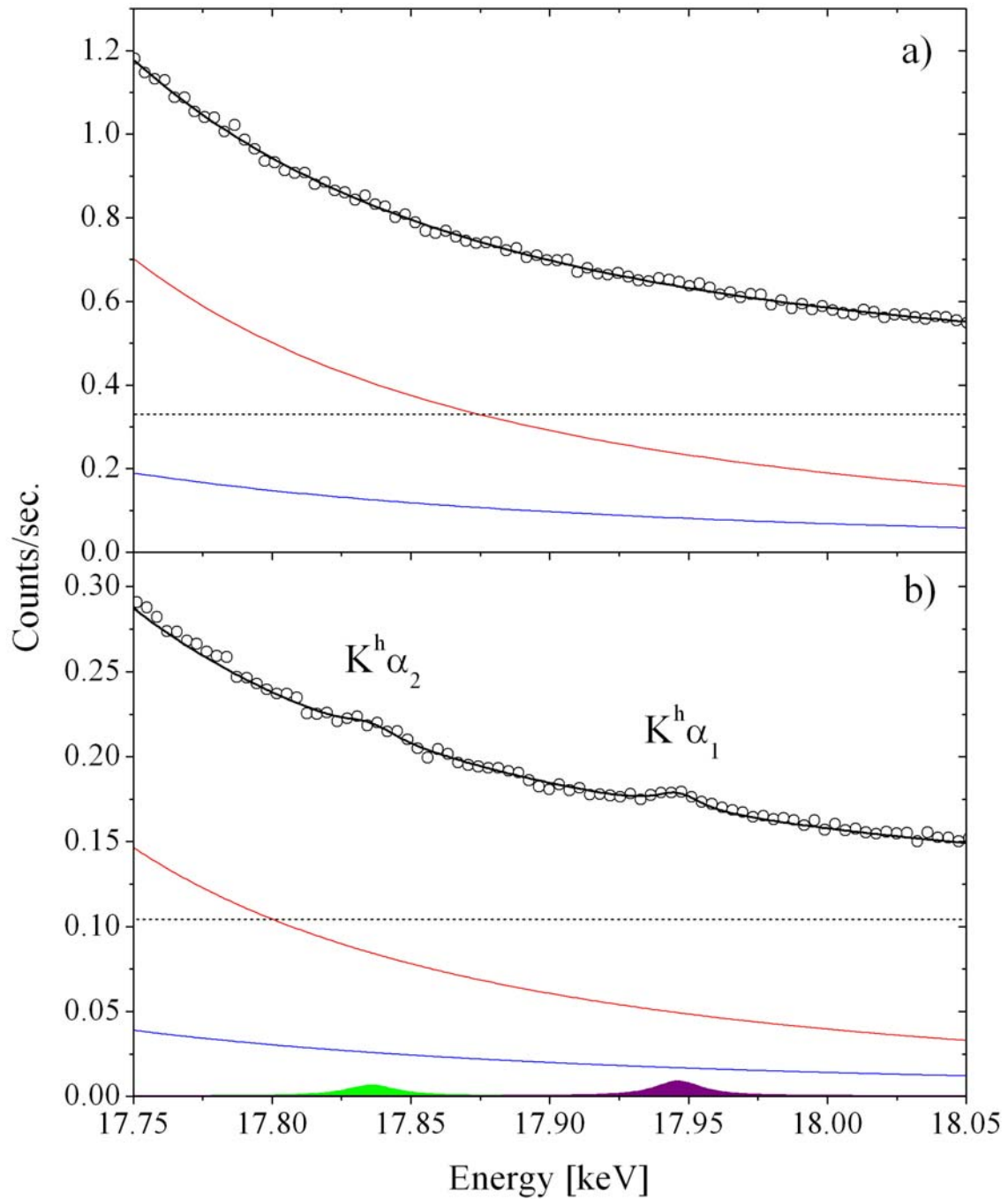


FIGURE 40: Fitted  $K\alpha$  x-ray spectrum of molybdenum in the region of the hypersatellite lines for the measurements performed (a) without absorbers and (b) with the  $50\ \mu\text{m}$  thick niobium plus  $25\ \mu\text{m}$  thick yttrium absorbers. The red and blue solid lines correspond to the high-energy tails of the  $K\alpha_1$  and  $K\alpha_2$  diagram lines, respectively, and the dotted line to the linear background originating from the elastic scattering in the target of the x-ray tube bremsstrahlung. For the measurements with absorbers, the fitted hypersatellite lines are also represented (green and purple curves). The total fits to the experimental data are shown by black solid lines.

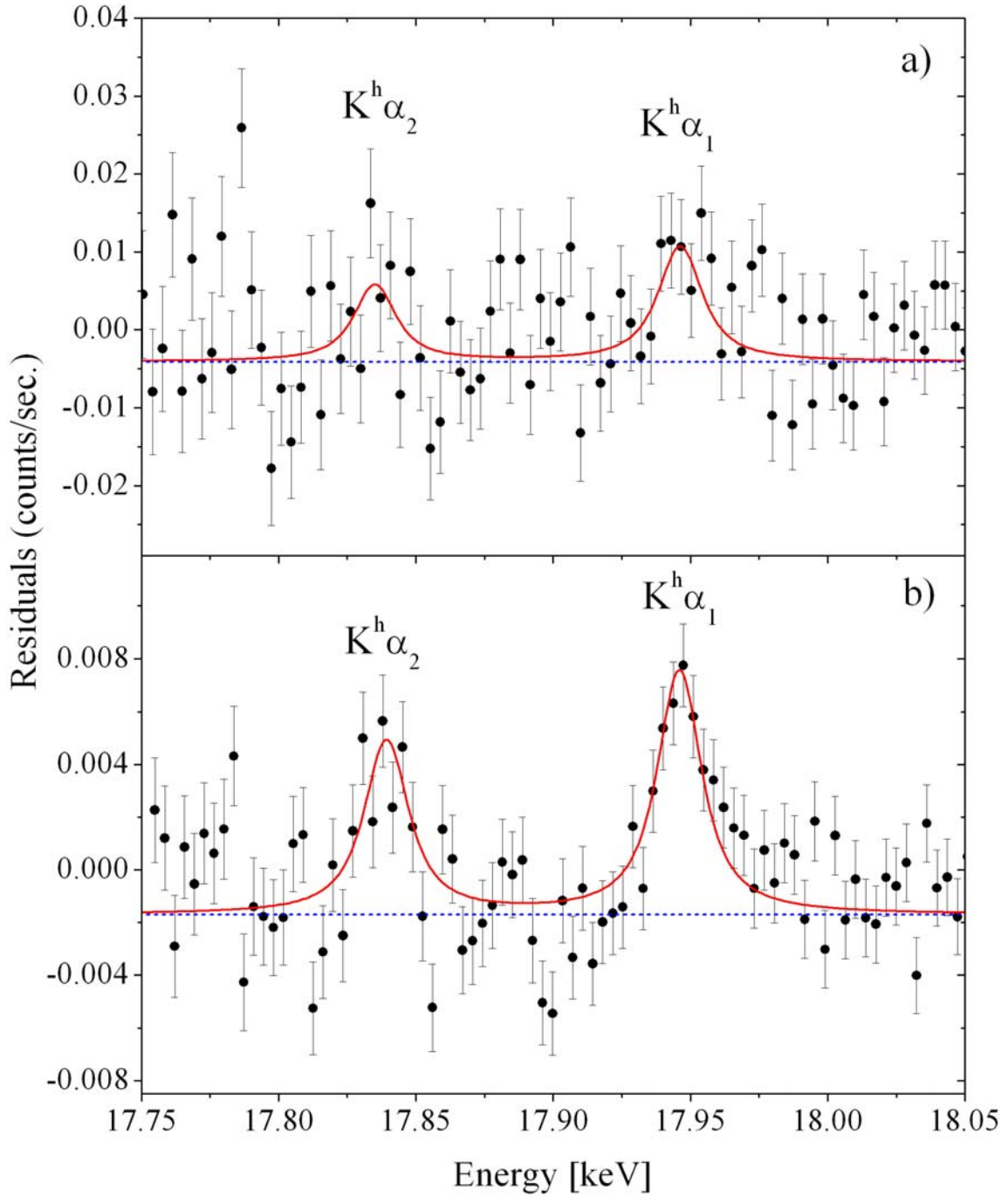


FIGURE 41: Fits of the residual spectra for (a) the measurements performed without absorber and (b) with the Nb + Y absorbers. The residual spectra were obtained by subtracting from the experimental data points the  $K\alpha_1$  and  $K\alpha_2$  tails and the linear background. The red solid lines correspond to the total fits and the dotted blue lines to the constant backgrounds used in these fits.

## 4. Results and discussion

### 4.1 Energies

The values obtained from the fits for the energies of the  $K\alpha$  diagram and  $K\alpha^h$  hypersatellite x-ray lines of molybdenum are listed in Table VIII where they are compared to results of MCDF calculations performed with the GRASP code [20]. The errors reported in Table VIII arise from the statistical errors given by the fits. The MCDF values obtained for the diagram and hypersatellite transitions are also presented graphically in the form of stick spectra in Fig. 42 and Fig. 43, respectively.

As it can be seen from Table VIII, the hypersatellite energies obtained from the measurements performed with and without absorbers are consistent within the fitting errors but the latter are rather large, especially for the measurements without absorbers, due to the poor statistics of the residual spectra. Furthermore, the values provided by the GRASP calculations are found to be systematically higher by about 2 eV. This systematic deviation arises probably from an offset energy in the theoretical energy scale.

The energy shifts of the hypersatellites with respect to their parent diagram lines obtained in the present study are presented in Table IX together with the experimental values obtained by Boschung *et al.* [14] and the theoretical predictions from the GRASP code and from other MCDF calculations performed by Chen *et al.* [21]. As shown, present results are in good agreement with the single other available experimental values as well as with both theoretical predictions. The biggest difference is observed for the  $K\alpha_2^h$

TABLE VIII: Experimental energies obtained from the fits for the diagram and hypersatellite lines of molybdenum. Present results are compared to the theoretical predictions provided by the GRASP code [20]. Quoted uncertainties correspond to the statistical errors from the fits.

	This work		GRASP calculations
	no absorber	with absorber	
$E(K\alpha_2)$ [eV]	$17374.24 \pm 0.04$	$17374.34 \pm 0.04$	17376.42
$E(K\alpha_1)$ [eV]	$17479.24 \pm 0.02$	$17479.41 \pm 0.02$	17481.13
$E(K\alpha_2^h)$ [eV]	$17835.05 \pm 5.39$	$17839.27 \pm 2.15$	17843.49
$E(K\alpha_1^h)$ [eV]	$17946.25 \pm 3.70$	$17945.98 \pm 1.54$	17948.49

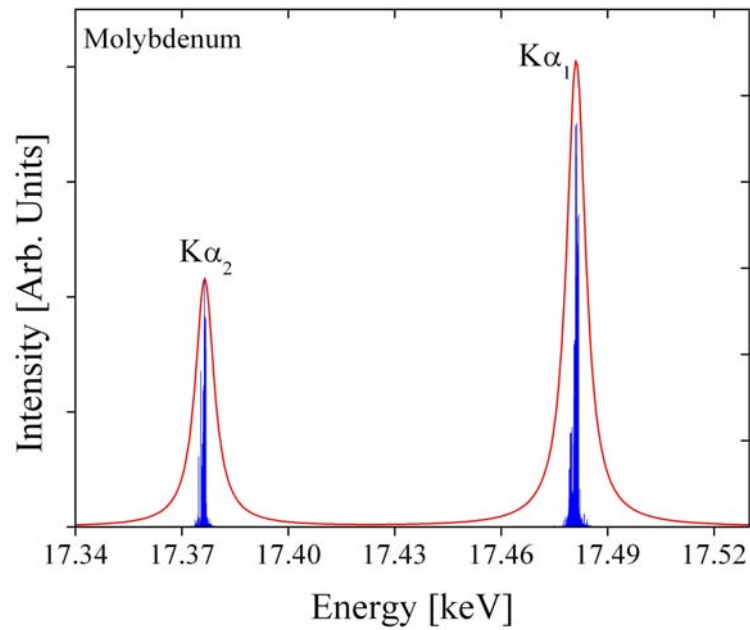


FIGURE 42: The  $K\alpha_{1,2}$  x-ray transitions of Mo calculated by means of the GRASP code (blue bars). The spectral line shape (red solid line) was calculated by attaching to each MCDF component a Lorentzian function whose width ( $\Gamma_K + \Gamma_L$ ) was derived from the atomic level widths listed in [19] and by calculating then the sum of all Lorentzians.

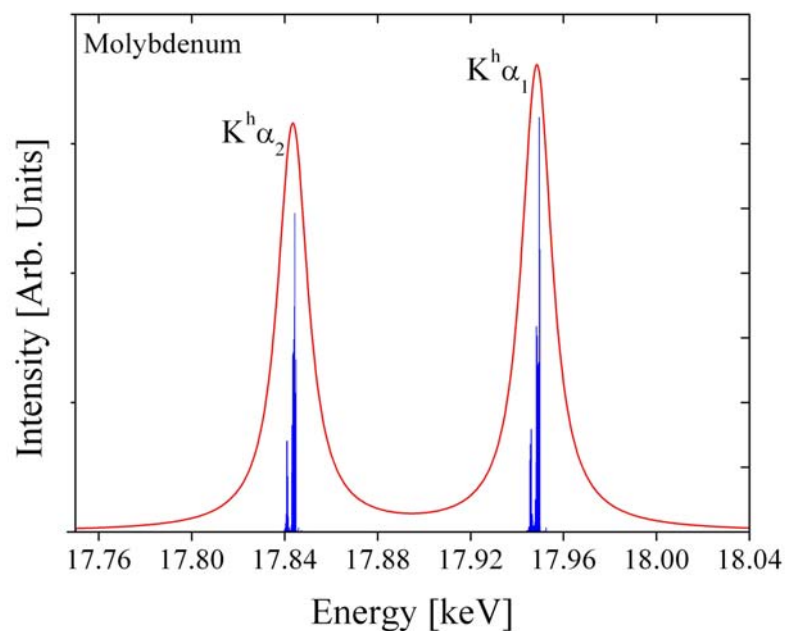


FIGURE 43: Same as Fig. 42, except that the Lorentzian width attached to each MCDF component was calculated with the approximation of Mossé ( $3\Gamma_K + \Gamma_L$ ) [22].

TABLE IX: Present experimental energy shifts of the  $K\alpha_{1,2}$  hypersatellite lines with respect to the parent diagram lines. For comparison, theoretical values obtained from the GRASP code [20] and from calculations by Chen *et al.* [21] as well as the experimental value of Boschung *et al.* [14] are also quoted.

Energy shifts [eV]	This work		GRASP	Chen <i>et al.</i>	Boschung <i>et al.</i>
	no absorber	with absorber			
$E(K\alpha_2^h) - E(K\alpha_2)$	$460.8 \pm 5.4$	$465.0 \pm 2.1$	467.1	466	$465.4 \pm 1.0$
$E(K\alpha_1^h) - E(K\alpha_1)$	$467.0 \pm 3.7$	$466.6 \pm 1.5$	467.4	466	$465.2 \pm 1.0$

hypersatellite line measured without absorbers due to the poor statistics of this line but even in this case our value is consistent with the other quoted experimental and theoretical values.

## 4.2 Natural line widths

Due to the double vacancy state in the  $K$  shell, the natural linewidths of the  $K\alpha_1^h$  and  $K\alpha_2^h$  hypersatellite x-ray lines are expected to be significantly larger than the ones of the parent  $K\alpha_1$  and  $K\alpha_2$  diagram lines. The natural linewidth of an x-ray transition is indeed equal to the sum of the widths of the initial and final atomic states. As a consequence, the widths of the diagram transitions  $K\alpha_{1,2}$  are equal to  $\Gamma_K + \Gamma_{L3,L2}$ , whereas the ones of the hypersatellites  $K\alpha_{1,2}^h$  are given by  $2\Gamma_K + (\Gamma_K + \Gamma_{L3,L2}) = 3\Gamma_K + \Gamma_{L3,L2}$  if one assumes that the width of the doubly ionized initial state  $K^{-2}$  can be approximated by  $\Gamma_{KK} \cong 2\Gamma_K$  (Mossé's approximation [22]).

On the other hand, using the multiconfiguration Dirac-Fock (MCDF) calculations, Chen [23] has shown that the widths  $\Gamma_{KK}$  of double  $K$ -shell holes are bigger than those of single  $K$ -shell hole ( $\Gamma_K$ ) multiplied by two and that the difference between  $\Gamma_{KK}$  and  $2\Gamma_K$  decreases with the atomic number  $Z$ . For Ne ( $Z = 10$ ), the ratio  $\Gamma_{KK} : 2\Gamma_K$  is about 1.89. Therefore, Diamant *et al.* [24] have pointed out that the width of the hypersatellite line should be given by  $\Gamma_{KK} + \Gamma_K + \Gamma_L$ , rather than by  $3\Gamma_K + \Gamma_L$ . For Kr ( $Z = 36$ ), the ratio is 1.14. As Kr is the heaviest element tabulated in [23], the width  $\Gamma_{KK}$  for Mo ( $Z = 42$ ) was determined by extrapolation. A value  $\Gamma_{KK} = 9.96$  eV was found. Using in addition the atomic level widths  $\Gamma_K$  and  $\Gamma_{L2,3}$  reported by Campbell and Papp [17] for singly ionized atoms, values of 16.2 eV and 16.3 eV were obtained for the natural widths of the  $K\alpha_1^h$  and  $K\alpha_2^h$  hypersatellite, respectively.

The natural line widths of the  $K\alpha_1^h$  and  $K\alpha_2^h$  hypersatellite lines obtained from the fits of our data are presented in Table X where they are compared to the values calculated

TABLE X: Natural line widths of the  $K\alpha$  x-ray hypersatellite lines. For comparison, the experimental value reported in [14] and the values calculated with the two approximations described in the text are also presented.

	This work	$3\Gamma_K + \Gamma_L$	$\Gamma_{KK} + \Gamma_K + \Gamma_L$	Ref. [14]
$\Gamma(K\alpha_1^h)[\text{eV}]$	$17.2 \pm 5.0$	15.3	16.2	$19.5 \pm 2.1$
$\Gamma(K\alpha_2^h)[\text{eV}]$	$17.3 \pm 7.0$	15.4	16.3	$16.6 \pm 2.4$



with the two approximations and with the experimental values reported by Boschung *et al.* [14]. As shown, present values are in agreement with the results obtained in [14] with 100 MeV alpha particles. The same holds for the comparison with the values derived by means of the two approximations. As expected, the second approximation provides values which are closer to the experimental data but both approximations seem to somewhat underestimate the measured values. Actually, similar observations were done for lighter elements (Mg, Al and Si) [25, 26]. However, in view of the large uncertainties characterizing present results, no definitive conclusion can be drawn.

### 4.3 $K\alpha_1^h$ to $K\alpha_2^h$ intensity ratio

The intensity ratios of the  $K\alpha_1$  to  $K\alpha_2$  diagram lines have been investigated in a detailed way over a wide range of atomic numbers across the periodic table. The ratios were found to be nearly constant around 2. The situation is very different for the hypersatellite lines. For light elements for which the  $LS$  coupling scheme prevails, the  $K\alpha_1^h$  hypersatellite transition is strictly forbidden by the  $E1$  selection rules because it corresponds to a spin-flip transition. In the  $j-j$  coupling, however, which applies to heavy elements, the  $K\alpha_1^h$  is allowed. For mid-heavy elements such as Mo, for which the relevant coupling is the intermediate one, the  $K\alpha_1^h$  hypersatellite is not forbidden, neither allowed, but hindered by the selection rules. For these reasons, the  $K\alpha_1^h / K\alpha_2^h$  intensity ratio increases continuously with  $Z$ , varying from a value close to zero for light elements to a value approaching two for heavy elements. The variation of the ratio  $I(K\alpha_1^h)/I(K\alpha_2^h)$  as a function of the atomic number  $Z$  was calculated by Chen *et al.* [21] and the results of this study are shown in Fig. 44. From the latter one can see that the ratio increases rapidly between  $Z = 20$  and  $Z = 56$ . As Mo, the element investigated in the present work, lies in the  $Z$ -region where the ratio is expected to increase fast, it can be considered as a good candidate to probe the goodness of Chen's calculations.

The  $K\alpha_1^h$  to  $K\alpha_2^h$  intensity ratios extracted from our measurements performed with and without absorbers are given in Table XI where they are compared to other available experimental values. As expected, the result obtained from the measurements performed with the absorbers is closer to the two other experimental data quoted in [14] and [27] and consistent with them but the relative uncertainty of the present result is quite large (more

TABLE XI: Measured intensity ratio of  $K\alpha_1^h$  to  $K\alpha_2^h$  hypersatellite lines compared to the other existing results.

	This work		Ref. [14]	Ref. [27]
	no absorber	with absorber		
$I(K\alpha_1^h)/I(K\alpha_2^h)$	$1.6 \pm 1.3$	$1.4 \pm 0.5$	1.34 (19)	$1.1 \pm 0.2$

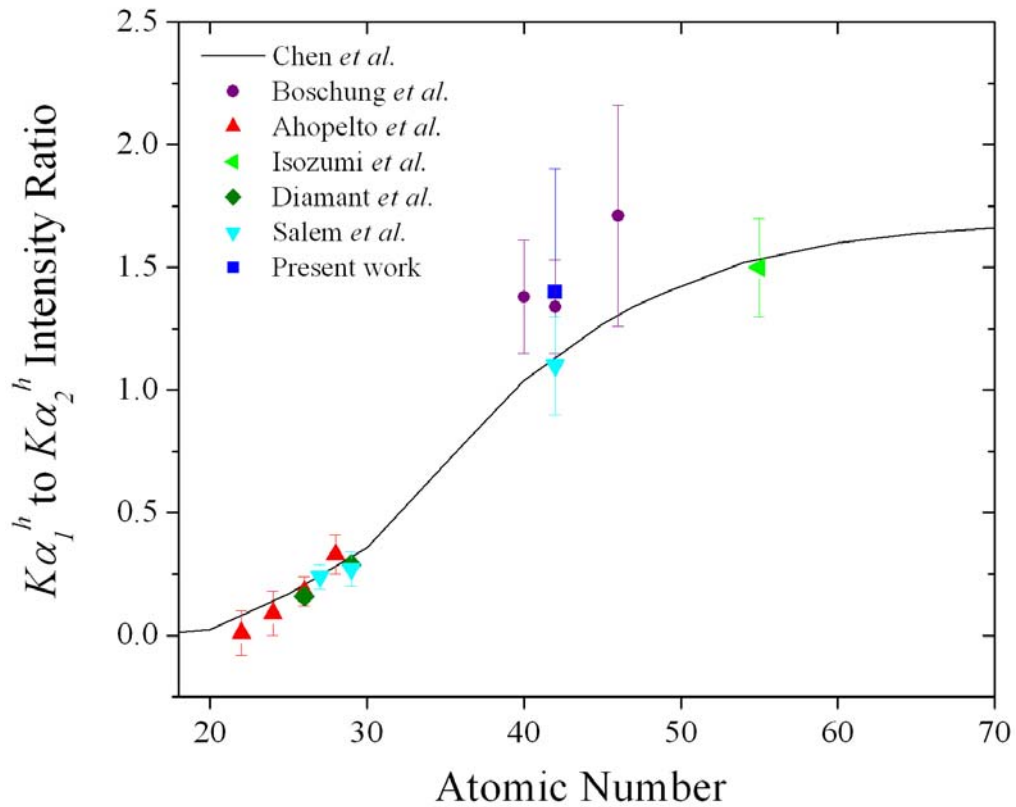


FIGURE 44: The  $K\alpha_1^h$  to  $K\alpha_2^h$  intensity ratio as a function of the atomic number  $Z$ . The black solid line stands for the results of DHS calculations by Chen et al. [21] and the symbols correspond to experimental values from: ● Ref.[14], ▼ Ref.[27,28], ◀ Ref.[29], ◆ Ref.[24,30], ▲ Ref.[31], ■ present work.

than 30%). In the case of the measurements performed without absorber, our ratio is bigger than the two other available experimental values, but still in agreement with them due to its very large relative uncertainty (80%). As shown in Fig. 44, the value predicted for Mo by Chen's calculations is about 1.1

#### 4.4 Hypersatellite-to-diagram line intensity ratio $I(K\alpha^h)/I(K\alpha)$

As the fitted intensities of the  $K\alpha_1^h$  and  $K\alpha_2^h$  hypersatellites measured without absorber are characterized by very large uncertainties, only the hypersatellites measured with the Nb and Y absorbers will be considered in this Section. The intensities of the hypersatellite and parent diagram lines provided by the fits were normalized to correspond to the same acquisition time per point and corrected to account for the self absorption in the target of the incoming photons and the  $K\alpha$  or  $K\alpha^h$  photons. From the obtained intensity ratio  $I(K\alpha^h)_{cor}/I(K\alpha)_{cor}$ , the double  $1s$  photoionization cross section  $\sigma_{KK}^{photo}$  could be derived, using the following relation:

$$\sigma_{KK}^{photo}(E) = \frac{I(K\alpha^h)_{cor}}{I(K\alpha)_{cor}} \cdot \frac{\omega_K}{\omega_{KK}} \cdot \sigma_K^{photo}(E), \quad (37)$$

where  $E$  stands for the energy of the incoming photon beam,  $\omega_K$  and  $\omega_{KK}$  are the fluorescence yields of the  $1s^{-1}$  singly ionized and  $1s^{-2}$  doubly ionized atoms and  $\sigma_K^{photo}$  is the single  $1s$  photoionization cross section. According to Chen [23], for light atoms the fluorescence yields corresponding to double  $K$ -hole states are increased by about 30% with respect to those of single  $K$ -hole states but for elements with  $Z \geq 25$  they are almost identical. Thus, for Mo one can assume that  $\omega_K \cong \omega_{KK}$ .

In our case, however, Eq. (35) cannot be applied in a straightforward way because the incoming photons have a continuous energy distribution. The difficulty can be circumvented by using the following approximation:

$$\sigma_{KK}^{photo}(\bar{E}_{KK}) = \frac{I(K\alpha^h)_{cor}}{I(K\alpha)_{cor}} \cdot \frac{\omega_K}{\omega_{KK}} \cdot \sigma_K^{photo}(\bar{E}_K) = \frac{I(K\alpha^h)_{cor}}{I(K\alpha)_{cor}} \cdot \frac{\omega_K}{\omega_{KK}} \cdot \sigma_K^{photo}(\bar{E}_{KK}) \cdot \frac{\sigma_K^{photo}(\bar{E}_K)}{\sigma_K^{photo}(\bar{E}_{KK})}, \quad (38)$$

where  $\bar{E}_K$  and  $\bar{E}_{KK}$  are the average energies of the bremsstrahlung photons contributing to the production of the  $1s^{-1}$  single vacancy states and  $1s^{-2}$  double vacancy states, respectively. These average energies can be calculated with the formula:

$$\bar{E}_{K, KK} = \frac{\int_{E_{thrK, KK}}^{HV} \int_0^h E \cdot I_{K, KK}(E, x) \cdot \sigma_{K, KK}^{photo}(E) \cdot dx \cdot dE}{\int_{E_{thrK, KK}}^{HV} \int_0^h I_{K, KK}(E, x) \cdot \sigma_{K, KK}^{photo}(E) \cdot dx \cdot dE}, \quad (39)$$

where  $E_{thrK, KK}$  stands for the threshold energy for a single, respectively double,  $K$ -shell ionization,  $h$  represents the thickness of the sample and  $I_{K, KK}(E, x)$  are intensities that are proportional to the bremsstrahlung intensity corrected for the self-absorption in the target of the incoming and fluorescence radiation. These intensities can be written as follows:

$$I_{K, KK}(E, x) = I_2(E) \cdot \int_0^h e^{-\mu_{K, KK}(E) \cdot x} dx = I_2(E) \cdot \frac{1 - e^{-\mu_{K, KK}(E) \cdot h}}{\mu_{K, KK}(E)}, \quad (40)$$

where  $I_2(E)$  stands for the bremsstrahlung intensity delivered by the x-ray tube with the Nb and Y absorbers [see Eq. (36)], and  $\mu_{K, KK}(E)$  is a function defined by:

$$\mu_{K, KK}(E) = \frac{\mu_{Mo}(E)}{\sin \alpha} + \frac{\mu_{Mo}(E_{K\alpha, K\alpha^h})}{\cos \alpha}. \quad (41)$$

In the above relation,  $\mu_{Mo}(E_i)$  represents the total absorption coefficient of Mo for the photon energy  $E_i$  and  $\alpha$  is the angle between the incoming photon beam and the target surface.

The functions  $\mu_{Mo}(E)$  and  $\sigma_K^{photo}(E)$  were determined by fitting a polynomial to the data tabulated in the XCOM database [18], while the double  $K$ -shell photoionization cross section function  $\sigma_{KK}^{photo}(E)$  was derived from the data reported in Refs. [33,34]. Using furthermore the values of 20.000 keV and 40.654 keV obtained from the GRASP code [20] for the threshold energies  $E_{thrK}$  and  $E_{thrKK}$  occurring in Eq. (39), average energies  $\bar{E}_K = 46.2$  keV and  $\bar{E}_{KK} = 57.6$  keV were finally obtained.

As  $E_{thrKK} > E_{thrK}$ , the number of bremsstrahlung photons contributing to the double  $K$ -shell photoionization is smaller than the number of photons producing a single  $K$ -shell photoionization. For this reason, the experimental hypersatellite-to-diagram yield ratio  $I(K\alpha^h)_{cor}/I(K\alpha)_{cor}$  should be further corrected by the following multiplicative factor:

$$F_N = \frac{\int_{E_{thrK}}^{HV} \int_0^h I_K(E, x) \cdot dx \cdot dE}{\int_{E_{thrKK}}^{HV} \int_0^h I_{KK}(E, x) \cdot dx \cdot dE}. \quad (42)$$

The double-to-single  $K$ -shell photoionization cross section ratio referred as  $P_{KK}$  in the literature can be deduced from Eq. (38):

$$P_{KK} = \frac{\sigma_{KK}^{photo}(\bar{E}_{KK})}{\sigma_K^{photo}(\bar{E}_{KK})} = \frac{I(K\alpha^h)_{cor}}{I(K\alpha)_{cor}} \cdot \frac{\sigma_K^{photo}(\bar{E}_K)}{\sigma_K^{photo}(\bar{E}_{KK})} \cdot F_N. \quad (43)$$

From (43), a value  $P_{KK} = 1.72 \times 10^{-4}$  was obtained with a relative uncertainty of about 30%. This rather large uncertainty originates mainly from the errors on the fitted  $K\alpha_1^h$  and  $K\alpha_2^h$  intensities. The present  $P_{KK}$  value is shown in Fig. 45 along with results for other elements obtained by different authors. The solid curve through the experimental data points corresponds to the power law fit  $P_{KK} \propto Z^{-1.61}$  proposed by Kanter *et al.* [32]. For comparison, the calculated asymptotic  $Z$ -scaling law of Forrey *et al.* [35] is also shown.

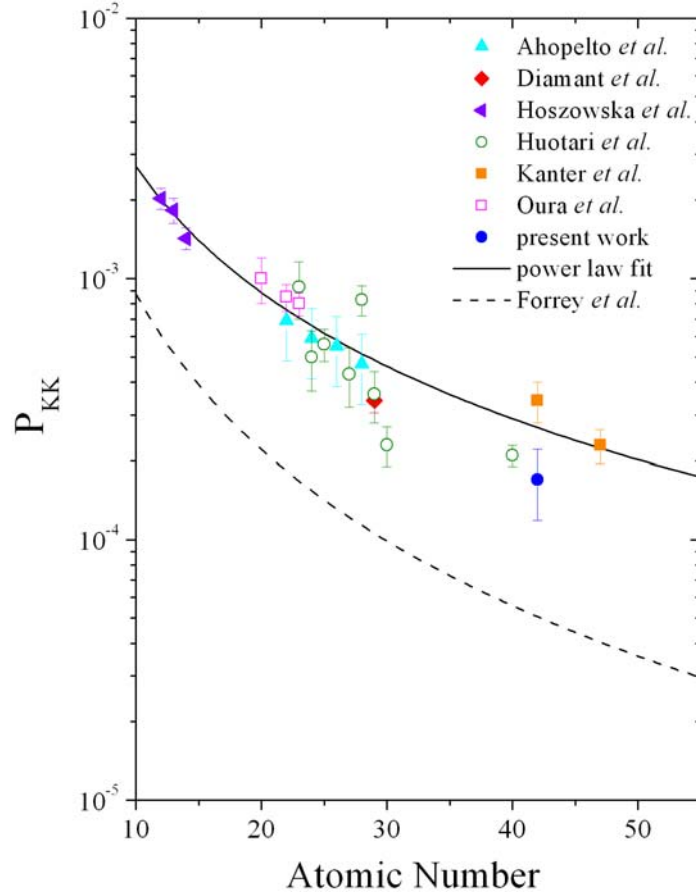


FIGURE 45: Double-to-single K-shell photoionization ratio as a function of the atomic number. The symbols correspond to experimental values: ● this work, ▲ Ref.[31], ◆ Ref.[24], ◀ Ref.[33], ○ Ref. [11], ■ Ref.12,32], □ Ref.[7]. The solid curve represents the power law fit of Kanter *et al.* [32] and the dashed line stands for the theoretical predictions of Forrey *et al.* [35].

As it can be seen from Fig. 45, our result is smaller by about 50% than the value expected from the  $Z^{1.61}$  power law proposed in [32] and not consistent with it. This is, however, not really surprising, because the errors on the correction factors employed in our method to determine  $P_{KK}$  were not considered. We have also compared our result with the one obtained by Kanter *et al.* [12] with synchrotron radiation and the satellite–hypersatellite coincidence technique. In this work, a value of  $3.4(6) \times 10^{-4}$  was found for an incident photon energy of 50 keV. This value is two times higher than ours and the discrepancy cannot be explained by the sole difference between the incoming photon beam energies (57.6 keV in the present work and 50 keV in Kanter’s experiment). Our result is thus probably too low but the one of Kanter might be also somewhat too high since it is neither consistent with the empirical curve corresponding to the power law fit.

## 5. Conclusion

High-resolution measurements of the  $K\alpha^h$  x-ray hypersatellite transitions of molybdenum were performed, using the Laue-type DuMond curved crystal spectrometer and a gold anode x-ray tube for the production of the target fluorescence. After a first attempt which was not really successful due to the very weak intensity of the hypersatellite lines and poor peak-to-background conditions, a second series of measurements was undertaken in which the background could be diminished significantly thanks to the use of dedicated absorbers placed between the x-ray tube and the sample.

From the analysis of the measured x-ray spectra, the energies and line widths of the two hypersatellite transitions could be determined as well as the  $K\alpha_1^h$  to  $K\alpha_2^h$  and  $K\alpha^h$  to  $K\alpha$  intensity ratios. A satisfactory agreement was found with available experimental values and theoretical predictions for the energies and natural line widths of the hypersatellites. For the  $K\alpha_1^h$  to  $K\alpha_2^h$  intensity ratio, the obtained value is somewhat higher than other experimental and theoretical data but consistent with them. In contrast to that, the double-to-single photoionization cross section ratio  $P_{KK}$  deduced from our measurements seems to be too small and is in slight disagreement with an empirical curve obtained by a power law fit to existing experimental data. A stronger discrepancy by a factor of about two was further found when comparing our  $P_{KK}$  value to the one obtained with synchrotron radiation by Kanter *et al.* No precise explanation was found for the deviation except that the uncertainty on our result, although already rather large, is underestimated, only the fitting errors having been considered. It is also possible, however, that the experimental result of Kanter is somewhat overestimated.



## 6. Bibliography

- [1] T.A. Carlson,  
*Double electron ejection resulting from photo-ionization in the outermost shell of He, Ne, and Ar, and its relationship to electron correlation.*  
Phys. Rev. **156** (1967) 142.
- [2] J.P. Briand, P. Chevallier, M. Tavernier and J.P. Rozet,  
*Observation of K hypersatellites and KL satellites in the x-ray spectrum of doubly K-ionized Gallium.*  
Phys. Rev. Lett. **27** (1971) 777.
- [3] O. Keski-Rahkonen, J. Saijonmaa, M. Suvanén and A. Servomaa,  
 *$K\alpha^h$  hypersatellite spectra and K shell double photoionization cross section of elemental Mg, V, Cr, Mn, and Fe.*  
Phys. Scripta **16** (1977) 105.
- [4] J.P. Briand, P. Chevallier, A. Chetoui, J.P. Rozet, M. Tavernier and A. Touati,  
*Correlation effects in double-K-vacancy production.*  
Phys. Rev. A **23** (1980) 39.
- [5] S.L. Carter and H.P. Kelly,  
*Double photoionization of helium.*  
Phys. Rev. A **24** (1981) 170.
- [6] C. Dal Cappello, R. El Mkhater, and P.A. Hervieux,  
*Mechanisms of double ionization of atoms by electron impact.*  
Phys. Rev. A **57** (1998) R693.

- [7] M. Oura, H. Yamaoka, K. Kawatsura, K. Takahiro, N. Takeshima, Y. Zou, R. Hutton, S. Ito, Y. Awaya, M. Terasawa, T. Sekioka and T. Mukoyama, *Correlative multielectron processes in K-shell photoionization of Ca, Ti and V in the energy range of 8–35 keV*.  
J. Phys. B: At. Mol. Opt. Phys. **35** (2002) 3847.
- [8] S.H. Southworth, E.P. Kanter, B. Krässig, L. Young, G.B. Armen, J.C. Levin, D.L. Ederer and M.H. Chen, *Double K-shell photoionization of neon*.  
Phys. Rev. A **67** (2003) 062712.
- [9] M. Kobal, M. Kavčič, M. Budnar, J.-Cl. Dousse, Y.-P. Maillard, O. Mauron, P.-A. Raboud and K. Tökési, *Double K-shell ionization of Mg and Si induced in collisions with C and Ne ions*.  
Phys. Rev. A **70** (2004) 062720.
- [10] R. Diamant, S. Huotari, K. Hämäläinen, C.C. Kao, and M. Deutsch, *The evaluation of inner-shell multielectronic x-rays spectra from threshold to saturation for low- to high- Z atoms*.  
Rad. Phys. Chem. **75** (2006) 143.
- [11] S. Huotari, K. Hämäläinen, R. Diamant, R. Sharon, C.C. Kao, and M. Deutsch, *Intrashell electron-interaction-mediated photoformation of hollow atoms near threshold*.  
Phys. Rev. Lett. **101** (2008) 043001.
- [12] E.P. Kanter, R.W. Dunford, B. Krässig and S.H. Southworth, *Double K-vacancy production in molybdenum by x-ray photoionization*.  
Phys. Rev. Lett. **83** (1999) 508.

- [13] Joseph B. Mann and Walter R. Johnson,  
*Breit interaction in multielectron atoms.*  
Phys. Rev. A **4** (1971) 41.
- [14] B. Boschung, J.-Cl. Dousse, B. Galley, Ch. Herren, J. Hoszowska, J. Kern,  
Ch. Rhême, Z. Halabuka, T. Ludziejewski, P. Rymuza, Z. Sujkowski, and  
M. Polasik,  
*K $\alpha$  hypersatellite lines of medium-mass atoms induced by 100-MeV  $4\text{He}^{2+}$  ions.*  
Phys. Rev. A **51** (1995) 3650.
- [15] S. Huotari, K. Hämäläinen, R. Diamant, R. Sharon, C.C. Kao, M. Deutsch,  
*X-ray hypersatellites spectra of hollow atoms.*  
J. Electron Spectrosc. Relat. Phenom. **137** (2004) 293.
- [16] T. Åberg,  
*Theory of x-ray satellites.*  
Phys. Rev. **156** (1967) 35.
- [17] L.V. Azaroff,  
*Elements of X-Ray Crystallography.*  
McGraw-Hill Book Company, New York, 1968.
- [18] <http://physics.nist.gov/PhysRefData/Xcom/Text/XCOM.html>.
- [19] J.L. Campbell and T. Papp,  
*Widths of the atomic K-N7 levels.*  
At. Data Nucl. Data Tables **77** (2001) 1.

- [20] A. Bar-Shalom, K.G. Dyall, I.P. Grant, C.T. Johnson, M. Klapisch, D.F. Mayers, B.J. McKenzie, P.H. Norrington, F. Parpia, E.P. Plummer and N.C. Pyper, *GRASP a general – purpose relativistic atomic structure program*. Version 1.0 (March 1988).
- [21] M.H. Chen, B. Crasemann and H. Mark, *Effect of the Breit interaction on K x – ray hypersatellite spectra*. Phys. Rev. A **25** (1982) 391.
- [22] J.P. Mossé, P. Chevallier and J.P. Briand, *On the natural width of the Hypersatellite lines*. Z. Phys. A – Atoms and Nuclei **322** (1985) 207.
- [23] M.H. Chen, *Auger transition rates and fluorescence yields for the double-K-hole state*. Phys. Rev. A **44** (1991) 239.
- [24] R. Diamant, S. Huotari, K. Hämäläinen, C.C. Kao, and M. Deutsch, *Cu  $K^h\alpha_{1,2}$  hypersatellites: Suprathreshold evolution of a hollow-atom x-ray spectrum*. Phys. Rev. A **62** (2000) 052519.
- [25] J. Hozowska, A.S. Kheifets, M. Berset, I. Bray, W. Cao, J.-Cl. Dousse, K. Fennane, M. Kavčič, Y. Kayser, J. Szlachetko and M. Szlachetko, *Double K-shell photoionization of low-Z atoms and He-like ions*. Eur. J. Phys. Special Topics **169** (2009) 23.
- [26] K. Fennane, J.-Cl. Dousse, J. Hozowska, M. Berset, W. Cao, Y.-P. Maillard, J. Szlachetko, M. Szlachetko, and M. Kavčič, *Double K-shell ionization of Al induced by photon and electron impact*. Phys. Rev. A **79** (2009) 032708.

- [27] S.I. Salem,  
*K $\alpha$  hypersatellites of Mo.*  
Phys. Rev. A **21** (1980) 858.
- [28] S.I. Salem, A. Kumar and B.L Scott,  
*Two-electron, one-photon transition in Cr, Fe, Co, and Cu.*  
Phys. Rev. A **29** (1984) 2634.
- [29] Y. Isozumi, Ch. Briannon and R.J. Walen,  
*Double K-hole creation accompanying K-electron capture decay of  $^{131}\text{Cs}$ .*  
Phys. Rev. C **25**, 3078 (1982).
- [30] R. Diamant, S. Huotari, K. Hämäläinen, R. Sharon, C.C. Kao, and M. Deutsch,  
*Diagram x-ray emission spectra of a hollow atom: The  $K^h\alpha_{1,2}$  and  $K^h\beta_{1,3}$  hypersatellites of Fe.*  
Phys. Rev. Lett. **91** (2003) 193001.
- [31] J. Ahopelto, E. Rantavuori and O. Keski-Rahkonen,  
*K $\alpha$  hypersatellite spectra in photon excitation and K shell double photoionization cross section for transition metals Ti, Cr, Fe, Ni.*  
Phys. Scr. **20** (1979) 71.
- [32] E.P. Kanter, I. Ahmad, R.W. Dunford, D.S. Gemmel, B. Krässig, S.H. Southworth, and L. Young,  
*Double K-shell photoionization of silver.*  
Phys. Rev. A **73** (2006) 022708.
- [33] J. Hozowska, A. K. Kheifets, J.-Cl. Dousse, M. Berset, I. Bray, W. Cao, K. Fennane, Y. Kayser, M. Kavčič, J. Szlachetko, and M. Szlachetko,  
*Physical Mechanisms and Scaling Laws of K-Shell Double Photoionization.*  
Phys. Rev. Lett. **102** (2009) 073006.

- [34] A. K. Kheifets, I. Bray and J. Hozowska,  
*K-shell double photoionization of Be, Mg and Ca.*  
Phys. Rev. A **79** (2009) 042504.
- [35] R.C. Forrey, H.R. Sadeghpour, J.D. Baker, J.D.Morgan, and A. Dalgarno,  
*Double photoionization of excited 1S and 3S states of the helium isoelectronic sequence.*  
Phys. Rev. A **51** (1995) 2112.

## Acknowledgments

*This Ph.D thesis was carried out at the University of Fribourg, Department of Physics in Switzerland. During this time, many people have given me their support and guidance. It is a pleasure to have the opportunity to express my gratitude to all of them.*

*My very special thanks I would like to express to my supervisor Prof. Jean-Claude Dousse who introduced me into the field of experimental atomic physics and guided my work during my Ph.D. years. His very broad experience, suggestions and overall help were highly important for me and absolutely crucial in carrying out this work.*

*I would like to deeply thank Dr. Joanna Hoszowska for all her help. I am very grateful for her useful comments and suggestions, helpful advice and interest in my work.*

*My gratitude goes also to Prof. Marek Pajek, Physics Institute, Jan Kochanowski University, for having accepted to review my Ph.D. thesis.*

*I direct my special thanks to Michel Berset. All his suggestions, comments and remarks as well as his technical assistance have helped me in achieving successful results in the project. I owe him a lot.*

*Many thanks to all colleagues and friends who have worked with me during my study, especially Karima Fennane, Yves-Patrick Maillard, Jean-Luc Schenker, Yves Kayser, Wei Cao and Matjaz Kavcic for the pleasant atmosphere and truly happy time spent together during these years.*

*I am also grateful to the administrative and workshop staff for their kindness and help.*

*Finally, my most sincere gratitude goes to my family for their every day support during these years. I wish to thank my husband Jakub for being incredibly understanding, supportive, and most of all, patient. Thank you for believing in me. My deepest thanks go to my son Dominik who made me laugh more than any one I know during this time. I am so grateful for your presence in my life. DZIEKUJE.*





# Curriculum vitae

## Personal information

First name: Monika Weronika  
Last name: Szlachetko  
Date and place of Birth: 25 September 1979, Kielce, Poland  
Nationality: Polish  
Marital status: married  
Child: Dominik, born on Jan. 13<sup>th</sup>, 2008

## Education

**2004–2008:** Ph.D. student and assistant in the Atomic Physics Group of the Physics Department, University of Fribourg, Switzerland.

**1998–2003:** Master in physics  
Institute of Physics, Holy Cross Academy, Kielce, Poland.

**1994–1998:**  
Secondary school, Staszów, Poland

**1986–1994:**  
Primary school, Niziny, Poland.

## Diplomas

- Master of Physics (Holy Cross Academy, Kielce, Poland)
- Secondary School Certificate.



# List of publications

## Refereed articles

***„Resonant x-ray Raman scattering for Al, Si and their oxides”.***

J. Szlachetko, R. Barrett, M. Berset, J.-Cl. Dousse, K. Fennane, J. Hoszowska, A. Kubala-Kukuś, M. Pajek, M. Szlachetko,  
Nuclear Instruments and Methods in Physics Research B 238, 353 (2005).

***„High-resolution study of x-ray resonant Raman scattering at the K-edge of silicon”.***

J. Szlachetko, J.-Cl. Dousse, J. Hoszowska, M. Pajek, R. Barrett, M. Berset, K. Fennane, A. Kubala-Kukuś, M. Szlachetko,  
Physical Review Letters 97, 073001 (2006).

***„High-resolution study of x-ray resonant Raman scattering process around 1s absorption edge for aluminium, silicon, and their oxides”.***

J. Szlachetko, J.-Cl. Dousse, J. Hoszowska, M. Pajek, R. Barrett, M. Berset, K. Fennane, A. Kubala-Kukuś, and M. Szlachetko,  
Physical Review A 75, 022512 (2007).

***„Relative detection efficiency of back- and front-illuminated charge-coupled device cameras for x-ray between 1 keV and 18 keV”.***

J. Szlachetko, J.-Cl. Dousse, J. Hoszowska, M. Berset, W. Cao, M. Kavčič and M. Szlachetko,  
Review of Scientific Instruments 78, 9 (2007).

***„Physical mechanisms and scaling laws of K-shell double photoionization”.***

J. Hoszowska, A.S. Kheifets, J.-Cl. Dousse, M. Berset, I. Bray, W. Cao, K. Fennane, Y. Kayser, M. Kavčič, J. Szlachetko, and M. Szlachetko,  
Physical Review Letters 102, 073006 (2009).

***„Double K-shell photoionization of low-Z atoms and He-like ions”***

J. Hoszowska, A.S. Kheifets, M. Berset, I. Bray, W. Cao, J.-Cl. Dousse, K. Fennane, M. Kavčič, Y. Kayser, J. Szlachetko and M. Szlachetko, European. Physical Journal: Special Topics 169, 23 (2009).

***„Double K-shell ionization of Al induced by photon and electron impact”***

K. Fennane, J.-Cl. Dousse, J. Hoszowska, M. Berset, W. Cao, Y.-P. Maillard, J. Szlachetko, M. Szlachetko, and M. Kavčič, Physical Review A 79, 032708 (2009).

***„Application of the high-resolution grazing-emission x-ray fluorescence method for impurities control in semiconductor technology”***

J. Szlachetko, D. Banaś, A. Kubala-Kukuś, M. Pajek, W. Cao, J.-Cl. Dousse, J. Hoszowska, Y. Kayser, M. Szlachetko, M. Kavčič, M. Salomé, J. Susini, Journal of Applied Physics 105, 086101 (2009).

## Conference abstracts

***„Resonant Raman scattering for Al, Si and their oxides”.***

J. Szlachetko, R. Barrett, M. Berset, J.-Cl. Dousse, K. Fennane, J. Hoszowska, A. Kubala-Kukuś, M. Pajek, M. Szlachetko,  
4th Conference on Synchrotron Radiation in Materials Science, Grenoble 2004, France.

***„X-ray resonant Raman scattering in Si at 1s absorption edge”.***

J. Szlachetko, R. Barrett, M. Berset, J.-Cl. Dousse, K. Fennane, J. Hoszowska, A. Kubala-Kukuś, M. Pajek, M. Szlachetko,  
ESRF Users Meeting, Grenoble 2005, France.

***„Size-dependent K $\beta$  resonant X-ray emission spectra of MnO<sub>2</sub> nanopowder”.***

J. Hoszowska, M. Berset, J.-Cl. Dousse, K. Fennane, J. Szlachetko, M. Szlachetko,  
ESRF Users Meeting, Grenoble 2005, France.

***„First high-resolution study of the double 1s photoionization of Mg”.***

J.-Cl. Dousse, J. Hoszowska, M. Berset, K. Fennane, J. Szlachetko, M. Szlachetko,  
20th International Conference on X-ray and Inner-Shell Processes, Melbourne 2005, Australia.

***„Size-dependent resonant K x-ray emission spectra of Mn and Fe oxide nanopowders”.***

J. Hoszowska, M. Berset, J.-Cl. Dousse, K. Fennane, J. Szlachetko, M. Szlachetko,  
20th International Conference on X-ray and Inner-Shell Processes, Melbourne 2005, Australia.

***„X-ray resonant Raman scattering in Si and SiO<sub>2</sub> at Si-K absorption edge”.***

J. Szlachetko, R. Barrett, M. Berset, J.-Cl. Dousse, K. Fennane, J. Hoszowska, A. Kubala-Kukuś, M. Pajek, M. Szlachetko,  
XXIV International Conference on Photonic, Electronic and Atomic Collisions, Rosario 2005, Argentina.

***„First high-resolution observation of X-ray resonant Raman scattering in Si at 1s absorption edge”.***

J. Szlachetko, R. Barrett, M. Berset, J.-Cl. Dousse, K. Fennane, J. Hoszowska, A. Kubala-Kukuś, M. Pajek, M. Szlachetko,  
International Workshop on Photoionization, Campinas 2005, Brazil.

***„High-resolution study of the x-ray resonant Raman scattering for Al, Si, Al<sub>2</sub>O<sub>3</sub> and SiO<sub>2</sub> in the region of the K-absorption edge”.***

M. Szlachetko, R. Barrett, M. Berset, J.-Cl. Dousse, K. Fennane, J. Hoszowska, A. Kubala-Kukuś, M. Pajek, J. Szlachetko,  
International Workshop on Photoionization, Campinas 2005, Brazil.

***„X-ray resonant Raman scattering in Si and SiO<sub>2</sub> at Si K-absorption edge”.***

A. Kubala-Kukuś, J. Szlachetko, R. Barrett, M. Berset, J.-Cl. Dousse, K. Fennane, J. Hoszowska, M. Pajek, M. Szlachetko,  
8th International School and Symposium on Synchrotron Radiation in Natural Sciences, Zakopane 2006, Poland.

***„X-ray resonant Raman scattering below the Si-K absorption edge”.***

M. Pajek, J. Szlachetko, A. Kubala-Kukuś, R. Barrett, M. Berset, J.-Cl. Dousse, K. Fennane, J. Hoszowska, M. Pajek, M. Szlachetko,  
European Conference on X-Ray Spectrometry, Paris 2006, France.

***„Double 1s photoionization of Ca and V beyond maximum”.***

J. Hoszowska, J.-Cl. Dousse, K. Fennane, W. Cao, M. Kavčič, J. Szlachetko, M. Szlachetko,  
European Conference on X-Ray Spectrometry, Paris 2006, France.

**„Double K-shell ionization of magnesium and aluminium”.**

J.-Cl. Dousse, J. Hoszowska, K. Fennane, W. Cao, M. Kavčič, J. Szlachetko, M. Szlachetko,

European Conference on X-Ray Spectrometry, Paris 2006, France.

**„Relative detection efficiency of back- and front-illuminated CCD cameras for x-rays between 1keV and 18 keV”.**

J. Szlachetko, J.-Cl. Dousse, J. Hoszowska, M. Kavčič, W. Cao, M. Szlachetko,

ESRF Users Meeting, Grenoble 2007, France.

**„X-ray resonant Raman scattering in Si and SiO<sub>2</sub> below K-shell absorption edge”.**

M. Pajek, A. Kubala-Kukuś, J. Szlachetko, M. Berset, J.-Cl. Dousse, K. Fennane, M. Szlachetko, R. Barrett, J. Hoszowska,

12<sup>th</sup> Conference on total Reflection X-ray Fluorescence Analysis and Related Methods TXRF 2007, Trento 2007, Italy.

**„Application of grazing emission x-ray fluorescence for high-resolution detection of impurities in silicon”.**

M. Pajek, A. Kubala-Kukuś, D. Banaś, J.-Cl. Dousse, J. Hoszowska, J. Szlachetko, M. Szlachetko, W. Cao,

12<sup>th</sup> Conference on Total Reflection X-Ray Fluorescence Analysis and Related Methods TXRF 2007, Trento 2007, Italy.

**„High-resolution grazing emission x-ray fluorescence studies of impurities in silicon”.**

A. Kubala-Kukuś, M. Pajek, D. Banaś, J.-Cl. Dousse, J. Hoszowska, , J. Szlachetko, M. Szlachetko, W. Cao,

XXV International Conference on Photonic, Electronic and Atomic Collisions (ICPEAC), Freiburg 2007, Germany.

**„Photon energy dependence of the ratio of double to single K-shell ionization of magnesium, aluminium and silicon”.**

J. Hoszowska, J.-Cl. Dousse, M. Berset, W. Cao, K. Fennane, J. Szlachetko, and M. Szlachetko,

XXV International Conference on Photonic, Electronic and Atomic Collisions, Freiburg 2007, Germany.

**„High-resolution study of the x-ray resonant Raman scattering process around the K-absorption edge for Al, Al<sub>2</sub>O<sub>3</sub>, Si and SiO<sub>2</sub>”.**

J. Szlachetko, R. Barrett, M. Berset, J.-Cl. Dousse, K. Fennane, J. Hoszowska, A. Kubala-Kukuś, M. Pajek, and M. Szlachetko,

XXV International Conference on Photonic, Electronic and Atomic Collisions, Freiburg 2007, Germany.

**„Double 1s ionization of Al and Si by photon and electron impact”.**

J. Hoszowska, M. Berset, W. Cao, J.-Cl. Dousse, K. Fennane, Y. Kayser, J.-L. Schenker, J. Szlachetko, M. Szlachetko and M. Kavčič,

European Conference on X – ray Spectrometry, Dubrovnik 2008, Croatia.

**„Double K-shell photoionization of low-Z atoms and He-like ions”.**

J. Hoszowska, A.S. Kheifets, M. Berset, W. Cao, J.-Cl. Dousse, K. Fennane, M. Kavčič, Y. Kayser, J. Szlachetko, and M. Szlachetko,

21<sup>st</sup> International Conference on X-ray and Inner-Shell Processes, Paris 2008, France.

**„Investigation of the x-ray resonant Raman scattering process around the 1s absorption edge for Si, SiO<sub>2</sub>, Al and Al<sub>2</sub>O<sub>3</sub>”.**

J.-Cl. Dousse, J. Szlachetko, R. Barrett, M. Berset, K. Fennane, J. Hoszowska, A. Kubala-Kukuś, M. Pajek, and M. Szlachetko,

21<sup>st</sup> International Conference on X-ray and Inner-Shell Processes, Paris 2008, France.



***„Application of high-resolution grazing emission x-ray fluorescence for material sciences”.***

J. Szlachetko, M. Pajek, A. Kubala-Kukuś, D. Banaś, J.-Cl. Dousse, J. Hoszowska, M. Szlachetko, Y. Kayser, W. Cao, M. Kavcic, M. Salomé, J. Susini,  
18<sup>th</sup> ESRF Users’ Meeting, Grenoble 2008, France.

***„Hollow magnesium, aluminium and silicon: photon energy dependence of double 1s ionization”.***

J. Hoszowska, J.-Cl. Dousse, M. Berset, W. Cao, K. Fennane, Y. Kayser, M. Kavčič, A. S. Kheifets, Y-P. Maillard, J. Szlachetko, and M. Szlachetko,  
Annual Meeting of the Swiss Physical Society, University of Geneva 2008.

***„Synchrotron radiation based high-resolution grazing emission x-ray fluorescence detection of Al-impurities on Si wafers”.***

Y. Kayser, D. Banaś, W. Cao, J.-Cl. Dousse, J. Hoszowska, A. Kubala-Kukuś, M. Pajek, M. Salomé, J. Susini, J. Szlachetko, M. Szlachetko,  
Annual Meeting of the Swiss Physical Society, University of Geneva 2008.

***„Application of high-resolution grazing emission x-ray fluorescence in material sciences”.***

A. Kubala-Kukuś, D. Banaś, W. Cao, J.-Cl. Dousse, J. Hoszowska, Y. Kayser, M. Pajek, J. Szlachetko, M. Szlachetko, M. Salomé, and J. Susini,  
9th International School and Symposium on Synchrotron Radiation in Natural Science (ISSRNS), Kielce 2008, Poland.

***„Resonant Raman scattering in synchrotron radiation based x-ray fluorescence analysis”.***

M. Pajek, D. Banaś, A. Kubala-Kukuś, J. Szlachetko, M. Berset, J.-Cl. Dousse, J. Hoszowska, K. Fennane, M. Szlachetko, R. Barrett,  
II National Conference: Polish Synchrotron – Beamlines (NCPSB), Kielce 2008, Poland.